IMAGING WITH AMBIENT SEISMIC NOISE: BEYOND SURFACE-WAVE MICROSEISMS

A DISSERTATION
SUBMITTED TO THE DEPARTMENT OF GEOPHYSICS
AND THE COMMITTEE ON GRADUATE STUDIES
OF STANFORD UNIVERSITY
IN PARTIAL FULFILLMENT OF THE REQUIREMENTS
FOR THE DEGREE OF
DOCTOR OF PHILOSOPHY

Jason P. Chang
August 2018

Abstract

Whether due to naturally occurring or human-generated vibrations, the ground is never truly at rest. Though individual recordings of these vibrations appear to be noisy, there are actually spatially coherent seismic signals hidden in them. By having two receivers record this ambient seismic noise continuously and simultaneously, it is possible to extract these hidden signals with a method called passive seismic interferometry, which effectively transforms one of the receivers into a seismic source. Thus, when performed on an array of receivers, passive seismic interferometry can produce an entire virtual seismic survey at a fraction of the cost of a traditional seismic survey with active sources. These virtual responses between receivers can then be used to image the subsurface.

A number of studies have successfully implemented passive seismic interferometry. However, the vast majority of them focus on extracting low-frequency microseism surface waves, which are generated by the interaction of ocean waves and the subsequent pressure variations along the sea-bottom. Though the resulting high-resolution subsurface velocity maps from these studies are impressive, they do not demonstrate the full potential of passive seismic interferometry. Hence, the goal of this thesis is to demonstrate the ability of passive seismic interferometry to extract more than just microseism surface waves. To do so, I apply the technique to three industry-scale seismic arrays located in three different environments.

I first focus on urban ambient seismic noise recorded by a dense seismic array in Long Beach, California. In this environment, passive seismic interferometry using continuous recordings between $3 - 4$ Hz extracts Rayleigh waves originating from these local roads. After tailoring my Rayleigh-wave traveltime selection criteria to account for the presence of noise sources within the array, I invert the traveltimes to produce near-surface group velocity maps that reveal structures that coincide well

with those in geologic maps, including the Newport-Inglewood fault.

I then switch to a shallow-water ocean-bottom node array in the North Sea to show that passive seismic interferometry can extract P-waves propagating through the water column in the ambient seismic noise field between $40-200$ Hz. Examination of the virtual responses between receivers over time reveals that the major sources of seismic energy at these high frequencies are distant shipping noise and the operating platform in the center of the array. Based on the successful extraction of P-waves, I aim to extract 1D reflection profiles from the continuous data by effectively performing seismic interferometry using ambient seismic noise after up- and down-going wavefield separation.

Finally, I work with ambient seismic noise recorded by a deep-water, long-offset ocean-bottom node array offshore Norway. Because of the length of the array, I focus on continuous recordings below 2 Hz, which is the microseism band. Though passive seismic interferometry in this environment extracts the commonly observed Scholte waves, it also extracts two other wave modes that have rarely been observed in ambient seismic noise. One is acoustic guided waves, which can be used to produce 1D P-wave velocity profiles. The other is critical refractions, which have never been observed in ambient seismic noise before and can potentially be used for tomography. Because of the novelty of this observation, I model one hypothesis for the natural generation of critical refractions.

Preface

The electronic version of this report[1] makes the included programs and applications available to the reader. The markings **ER**, **CR**, and **NR** are promises by the author about the reproducibility of each figure result. Reproducibility is a way of organizing computational research that allows both the author and the reader of a publication to verify the reported results. Reproducibility facilitates the transfer of knowledge within SEP and between SEP and its sponsors.

ER denotes Easily Reproducible and are the results of processing described in the paper. The author claims that you can reproduce such a figure from the programs, parameters, and makefiles included in the electronic document. The data must either be included in the electronic distribution, be easily available to all researchers (e.g., SEG-EAGE data sets), or be available in the SEP data library[2]. We assume you have a UNIX workstation with Fortran, Fortran90, C, X-Windows system and the software downloadable from our website (SEP makerules, SEPScons, SEPlib, and the SEP latex package), or other free software such as SU. Before the publication of the electronic document, someone other than the author tests the author's claim by destroying and rebuilding all ER figures. Some ER figures may not be reproducible by outsiders because they depend on data sets that are too large to distribute, or data that we do not have permission to redistribute but are in the SEP data library, or that the rules depend on commercial packages such as Matlab or Mathematica.

CR denotes Conditional Reproducibility. The author certifies that the commands are in place to reproduce the figure if certain resources are available. The primary reasons for the CR designation is that the processing requires 20 minutes

[1] http://sepwww.stanford.edu/public/docs/sep171
[2] http://sepwww.stanford.edu/public/docs/sepdatalib/toc_html/

or more.

NR denotes Non-Reproducible figures. SEP discourages authors from flagging their figures as NR except for figures that are used solely for motivation, comparison, or illustration of the theory, such as: artist drawings, scannings, or figures taken from SEP reports not by the authors or from non-SEP publications.

Our testing is currently limited to LINUX 2.6 (using the Intel Fortran90 compiler) and the SEPlib-6.4.6 distribution, but the code should be portable to other architectures. Reader's suggestions are welcome. For more information on reproducing SEP's electronic documents, please visit *http://sepwww.stanford.edu/research/redoc/*.

Acknowledgments

First, I would like to thank my academic advisor, Biondo Biondi, for allowing me to be a part of the Stanford Exploration Project. He took a chance on an undergraduate student who not only had very little coding experience, but who also graduated from UC Berkeley (of all places). His unwavering belief in my abilities and my work consistently gave me the confidence to push through any perceived setbacks, and his valuable insight and suggestions showed me how to become a better researcher. Second, I thank Bob Clapp for the countless hours he spent helping me become a competent programmer, for the guidance and insights he provided throughout my research beyond the computational aspects, and for his valuable career and life advice. I would also like to thank the founder of SEP, Jon Claerbout, for his endless enthusiasm for field data, his ideas, and his pool parties. Next, I'd like to thank my thesis committee member, Greg Beroza, for various helpful suggestions and allowing me to join his ambient-field seismology seminars over the summer. I thank Rosemary Knight for being my second-project advisor. I thank Jack Baker for chairing my defense.

I also thank senior members of SEP, Stewart Levin and Shuki Ronen, for their help converting between data formats and for sharing their expertise working with field data. Thanks also to SEP administrators – Diane Lau, Claudia Baroni, and Liliane Pereira – for handling all travel reimbursements and organizing our SEP and SEG meetings.

I would like to thank the sponsors of SEP for providing financial support for our research group. In particular, I would like to thank Dan Hollis of Nodal Seismic, Chris Walker of Seabed Geosolutions, and David Monk of the Apache Corporation for providing field datasets for my research and helpful comments on conference abstracts.

To my colleagues at SEP, I thank you all for the various suggestions, insights,

and laughs you shared with me. From the senior students – Gboyega Ayeni, Sjoerd de Ridder, Adam Halpert, Elita Li, Mandy Wong, Xukai Shen, Yang Zhang, Chris Leader, Ali Almomin, Musa Maharramov, Yi Shen, Qiang Fu, and Ohad Barak – to the junior students – Taylor Dahlke, Huy Le, Eileen Martin, Guillaume Barnier, Gustavo Alves, Daniel Blatter, Ettore Biondi, Kaixi Ruan, Alejandro Cabrales, Yinbin Ma, Joseph Jennings, Fantine Huot, Rahul Sarkar, Stuart Farris, Siyuan Yuan, Rustam Akhmadiev, and Miguel Ferrer – thank you all for making everyday in SEP so enjoyable.

I am also grateful to my first-year attic peers – Gader Alalli, Andreas Mavrommatis, Sam Bydlon, Emily Fay, Rall Walsh, Cyndi Kelly, Marina Kim, Brad Lipovsky, Ossian O'Reilly and Shaoyu Lu – and other department friends – Kevin Seats, Dario Grana, Nick Odlum, and Denys Grombacher – for all the fun times in and around Stanford. In particular, I thank Emily, Taylor, Shaoyu, and Rahul for being great officemates the past years, and Chris, Kevin, Andreas, and Dario for impromptu Sporcle sessions.

Having grown up in the Bay Area, I have been fortunate to have a strong group of friends in the region prior to coming to Stanford. I thank them all – particularly Noah Paul-Gin and Kent Tonozuka – for dragging me out of my Stanford bubble to go crabbing, play video games, eat free sushi, and try new activities. I also would like to thank my girlfriend, Helen Feng, for her love and support. Your constant optimism and encouragement helped me push through these final years of my PhD.

Finally, I would like to thank my family. To my parents, Wesley and Davian, thank you for supporting me throughout my life and for always being there for me. To my sister, Alison, thank you for inspiring me to be the best person I can be everyday. I am who I am today because of all of you, and I love you all.

Contents

List of Tables

List of Figures

Chapter 1

Introduction

The ground is never truly at rest. Whether human-generated like traffic noise and industrial work, or naturally occurring like earthquakes and ocean waves, vibrations from passive seismic sources are always propagating under our feet regardless of whether we can sense them or not. While these background vibrations appear to be incoherent noise when recorded by a single receiver, there is actually spatial coherent seismic signal hidden in the recording. By employing multiple receivers to simultaneously record these background vibrations, it is possible to extract these hidden coherent seismic signals through a method called seismic interferometry. For two receivers, the process effectively returns an estimate of the Green's function recorded by one receiver had the other receiver been an impulsive source.

The concept of using seismic interferometry with these background vibrations, or ambient seismic noise, is not new. Since the turn of the century, a number of studies have estimated the impulse response between receivers with great success across a range of spatial scales, from the continental scale with USArray to the local scale with industry-owned seismic networks. The majority of those studies extracted the surface-wave portion of the estimated Green's function at very low frequencies (below 2 Hz). The resulting surface-wave traveltimes between multiple receiver paths within an array are often used to perform surface-wave tomography, which produces high-resolution velocity models of the subsurface.

While seismic interferometry with ambient seismic noise has performed well at recovering low-frequency surface waves, there have been far fewer successes when

focusing on higher-frequency noise or non-surface waves. The reasons for the relative lack of success are numerous, including the characteristic of noise sources at higher frequencies, the relative strength of surface waves compared to body waves, and the lack of large, dense seismic arrays that continuously record seismic data. This thesis addresses these issues and aims to extract these less-common wave modes from the ambient seismic noise field at the exploration scale.

BENEFITS OF PASSIVE SEISMIC SURVEYS

A passive seismic survey refers to an array of receivers that continuously records the ambient seismic noise field. Though these surveys do not record the same high-resolution seismic data as traditional seismic surveys with active seismic sources (e.g., marine air guns, vibroseis trucks, explosives), they can sometimes provide a more practical option for subsurface imaging when combined with seismic interferometry.

First, seismic surveys with active seismic sources are expensive to operate, from the amount of man-power required to execute these surveys to the financial cost of the acquisition equipment. The cost of these surveys increases when interested in time-lapse studies, where multiple surveys over time are required. With a passive seismic survey, expensive active seismic sources are no longer required. Instead, the signal is ambient seismic noise, which is continuously generated everywhere at no cost. Because ambient seismic noise is always being generated, it is also naturally suited for low-cost subsurface monitoring.

Second, active seismic sources, particularly those used for hydrocarbon exploration, are often unrealistic or highly inconvenient in certain environments. For instance, using vibroseis trucks to perform seismic surveys in urban environments, though doable, presents multiple logistical challenges such as acquiring city permits and educating the community about the nature of active seismic surveys. Alternatively, ambient seismic noise occurs without any disruption to the surrounding environment. The requirement of only an array of continuously recording receivers allows new locations, such as urban settings and environmentally protected areas, to be seismically imaged in a non-intrusive manner. The ability to seismically characterize the subsurface in these areas can have significant benefits, particularly for earthquake hazard analysis in densely populated regions.

Third, active seismic sources often have difficulty creating low-frequency (below 10 Hz) energy. Though technology is developing to address this frequency gap (e.g., Dellinger et al., 2016), they are not yet commonly employed. These low frequencies can be useful for building starting velocity models for full-waveform inversion. Conveniently, ambient seismic noise is commonly strong at low frequencies and has the potential to fill in parts of this frequency gap. Furthermore, because the ambient seismic noise field is composed of primarily surface waves, it is well suited to characterize near-surface seismic velocities. This knowledge can be useful for improving the results of traditional seismic imaging algorithms. Though challenging to extract, low-frequency body waves in the ambient seismic noise field can also help generate useful starting models for imaging algorithms.

AMBIENT SEISMIC NOISE

In this thesis, ambient seismic noise refers to any seismic vibration not due to an active seismic source such as a vibroseis truck or a marine air gun. As a result, the ambient seismic noise field is my signal and any energy from traditional active-source seismic surveys is my noise. This is the opposite distinction from traditional seismic surveys. Sources of these background vibrations can be either natural or human-induced.

At low frequencies (below 2 Hz), the ambient seismic noise field is dominated by microseism energy, which is generated when ocean waves interact with each other to produce pressure variations at the sea bottom (Longuet-Higgins, 1950) or when ocean waves interact with the shoreline (Hasselmann, 1963). Though they are generated continuously, microseisms are strongest during stormy weather conditions because the strength of microseism energy is tied to the size of the ocean waves. Microseisms propagate primarily as surface waves (e.g., Blaik and Donn, 1953; Friedrich et al., 1998; Ekström, 2001), though they can also propagate as body waves (e.g., Toksöz and Lacoss, 1968; Landès et al., 2010). Importantly, these microseisms can be recorded everywhere (both on land and at sea) regardless of distance from the ocean, and often propagate along all azimuths. Because of the pervasiveness and strength of surface waves in the low-frequency microseism band, they are the most commonly used wave modes in ambient seismic noise studies. This thesis explores the ambient seismic noise field beyond these microseism surface waves. In Chapter 5, I focus on body waves in the microseism band.

At frequencies above 2 Hz, the sources of seismic noise shift from primarily natural sources (like ocean waves) to primarily anthropogenic sources. On land, road traffic dominates the ambient seismic noise field, particularly in urban environments (Chapter 2). Industrial noise can also greatly influence the background noise field, though it is less common than road traffic in many locations. Like microseisms, these anthropogenic sources on land primarily generate surface waves, though they can also produce body waves (Nakata et al., 2011). In Chapter 3, I work with the ambient seismic noise field between $3 - 4$ Hz in an urban environment.

In marine environments, the sources of high-frequency (above 2 Hz) seismic energy are different than on land. From approximately $10 - 500$ Hz, the ambient seismic noise field is dominated by primarily distant shipping noise (Wenz, 1972) propagating mostly horizontally through the water layer. Because the sea bottom and sea surface act as a waveguide for P-waves, shipping noise originating great distances from a receiver can be recorded. In the presence of drilling platforms, industrial noise can also be prevalent at these frequencies. From approximately 500 Hz$-$25 kHz, the ambient seismic noise field is dominated by breaking waves at the sea surface (Hildebrand, 2009), which propagates mostly vertically rather than horizontally. During periods of stormy weather, this breaking-wave energy can be detected at frequencies below 100 Hz (Brooks and Gerstoft, 2009). Since attenuation becomes more significant as frequency increases, breaking-wave energy is constrained to mostly shallow waters (100s m). In Chapter 4, I work with the ambient seismic noise field between $40 - 200$ Hz in a marine environment.

PASSIVE SEISMIC INTERFEROMETRY

The primary tool for extracting spatially coherent signal from the ambient seismic noise field is passive seismic interferometry. By cross-correlating simultaneous and continuous recordings of ambient seismic noise from two receivers, it is possible to extract the estimated Green's function (EGF) between those two receivers. The process effectively converts one of the receivers into a virtual seismic source. By repeating this procedure for all combinations of receivers in an array, an entire seismic survey can be simulated without involving a single active seismic source. Therefore, passive seismic interferometry is a data-processing method that creates a virtual seismic survey at a fraction of the cost of a traditional active-source seismic survey.

The concept of using seismic interferometry to extract spatially coherent seismic signal from the ambient seismic noise field has been proposed and used in practice for half a century. Claerbout (1968) first showed that the reflection response of a 1D medium could be retrieved from the auto-correlation of the transmission response, and Rickett and Claerbout (1999) proposed that cross-correlating noise traces recorded at two receivers would produce the wavefield that would be recorded between the two receivers. Since the beginning of this century, significant progress has been made in the applications of passive seismic interferometry. Campillo and Paul (2003) demonstrated that the EGF between two seismic stations could be retrieved by cross-correlating seismic coda waves. In 2005, the EGFs from ambient seismic noise were used for surface wave tomography. The relative density and the number of stations within the array allowed the estimation of high-resolution velocity models at the regional scale that had previously been unobtainable with limited earthquake sources (Shapiro et al., 2005; Sabra et al., 2005a).

Since then, numerous studies regarding passive seismic interferometry have been performed across multiple spatial scales with great success. The vast majority of these studies have focused on extracting the microseism surface-wave component of the EGF, with the resulting traveltimes of the surface waves used for high-resolution tomography at the continental (e.g., Lin et al., 2008; Yang et al., 2008; Bensen et al., 2008) and exploration scales (e.g., de Ridder and Dellinger, 2011; de Ridder et al., 2014; Mordret et al., 2014). In some cases, microseism diving waves (Roux et al., 2005) and reflections (Zhan et al., 2010; Ruigrok et al., 2011; Poli et al., 2012) have been successfully retrieved at the continental scale. However, there is no documented successful extraction of critical refractions from microseisms prior to Chapter 5 in this thesis.

The success of ambient noise studies at these scales has increased interest in applying this methodology to higher frequencies (greater than 2 Hz). There are a number of reasons to try to extract higher-frequency EGFs. For surface waves, they can provide velocity information about the near-surface (e.g., top 30 m), which is vital in earthquake hazard analysis. Higher frequencies of the ambient seismic noise field also have the potential to contain body waves, which would allow for high-resolution seismic imaging at the exploration scale.

For the most part, studies working with these frequencies have been restricted

to small-scale feasibility tests, as there are few large, dense array networks available for these types of studies. With small-scale arrays on land, it has been shown that high-frequency surface waves originating from anthropogenic sources can be extracted from the ambient seismic noise field (Halliday et al., 2008) and used to determine near-surface shear velocities (Picozzi et al., 2009; Pilz et al., 2012). Additionally, high-frequency body-wave reflections at the exploration scale can be extracted under highly ideal conditions where there is a single dominant noise source (e.g., road traffic) in an otherwise remote area (Draganov et al., 2007, 2013; Nakata et al., 2011). These reflections were then used to produce a migrated image of the subsurface. In Chapter 3, I extract Rayleigh waves between $3-4$ Hz generated by road traffic in an urban environment using passive seismic interferometry.

In marine environments, the dominant sources of seismic energy above 40 Hz are shipping noise, industrial noise, distant active seismic sources, and breaking waves at the sea surface. While these sources of energy rarely generate surface waves, they do produce P-waves. Using a small L-shaped (vertical and horizontal) array in offshore New Jersey, Brooks and Gerstoft (2009), extracted direct, sea-surface reflected, and sea-bottom reflected events in the water column generated by shipping and breaking-wave noise using seismic interferometry on ambient seismic noise between $20-100$ Hz. Mordret et al. (2013) extracted an apparent acoustic wave originating from an operating platform. Using an approach called passive fathometry, Gerstoft et al. (2008a) and Siderius et al. (2010) correlated up- and down-going energy from breaking waves at the sea surface to produce a shallow reflection image of the subsurface. In Chapter 4, I extract high-frequency ($40-200$ Hz) P-waves from the ambient seismic noise field in a shallow marine environment using seismic interferometry and a modified passive fathometry approach.

Theory

Seismic interferometry states that cross-correlating simultaneous and continuous recordings of ambient seismic noise from two receivers yields an estimate of the Green's function and its time-reversed version between the two receivers. In equation form,

this process can be expressed as (Wapenaar et al., 2010):

$$\langle u(x_B,t) * u(x_A,-t)\rangle \approx S(t) * \oint_{\partial V} G(x_B,x_s,t) * G(x_A,x_s,-t)\,\mathrm{d}x_s \tag{1.1}$$

$$\approx S(t) * \left[G(x_B,x_A,t) + G(x_B,x_A,-t)\right], \tag{1.2}$$

where x_A and x_B are the two receiver locations and x_s are noise source locations surrounding the receivers. $u(x_B,t)$ and $u(x_A,-t)$ are the noise recording at receiver B and the time-reversed noise recording at receiver A, respectively. The Green's functions are expressed as $G(x_A,x_s,t)$, where the first argument is the receiver location, the second argument is the impulsive source location, and the third argument is direction of time (reversed or not). ∂V is a closed boundary surrounding the two receivers that contains the sources x_s. $S(t)$ represents the auto-correlation of the source function. Convolution is expressed as $*$, with cross-correlation being defined as the convolution of one recording with the time-reversed version of another recording. $\langle\cdot\rangle$ represents ensemble averaging over all surrounding impulsive sources x_s. In words, the cross-correlation of seismic recordings at two receivers effectively evaluates the sum of cross-correlations of recordings of individual sources surrounding the receivers (Equation 1.1). This procedure yields an estimate of the Green's function and its time-reversed version had receiver A been a virtual source (Equation 1.2).

Passive seismic interferometry theory requires certain conditions to be met in order for an accurate, time-symmetric EGF to be extracted between two receivers. The first requirement is that noise sources must illuminate the two receivers equally from all directions (Lobkis and Weaver, 2001). For surface waves, noise sources at the surface surrounding the receivers is required. For body waves, noise sources not only at the surface but also in the subsurface is required. The second requirement is that noise sources are uncorrelated in time, which allows the ensemble averaging of cross-correlations of recordings of individual noise sources to be replaced by a single cross-correlation over a long period of time during which there are sources being excited in all directions (Wapenaar and Fokkema, 2006). This requirement is important in practice because separate responses to each individual noise source are no longer necessary. We can now use long recordings of continuously and simultaneously acting noise sources. While the second requirement is often met in practice, the first requirement is not. However, it is still possible to obtain reliable EGFs from the ambient seismic noise field in practice as long as strong noise sources are located in

certain positions around the receivers. This point is best explained with 2D synthetic examples.

Synthetic examples

To demonstrate the results of passive seismic interferometry, I provide 2D synthetic examples with different source distributions. The synthetic examples are set up with two receivers spaced 400 m apart in a lossless medium with a propagation velocity of 500 m/s. Point sources emitting Ricker wavelets with a central frequency of 30 Hz surround the two receivers at 0.25° intervals, with their distances from the midpoint of the two receivers randomly chosen from a uniform distribution between $1000-2000$ m. Note that these sources could also be temporally uncorrelated noise, in which case the EGFs would be convolved with the auto-correlation of the noise rather than the auto-correlation of the Ricker wavelet. In each example, I change the amplitudes of the sources based on azimuth to simulate uneven source distributions around the receivers that are often encountered in practice.

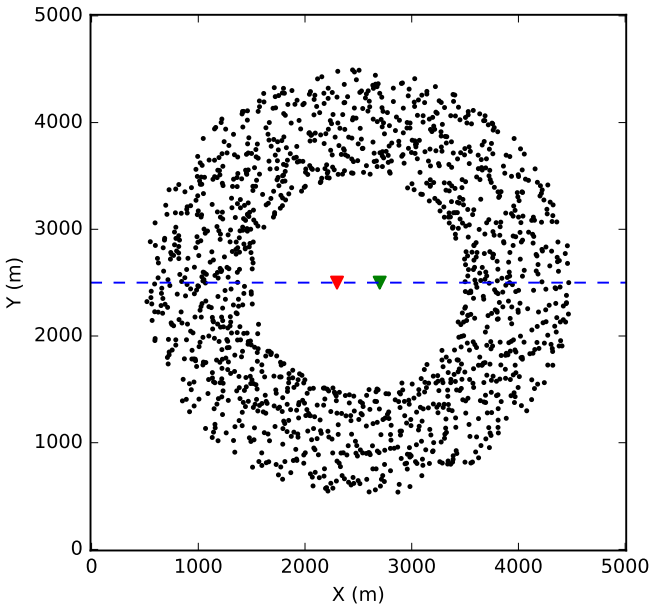

Figure 1.1: Set up for synthetic 2D example. Inverted triangles represent receivers, with red corresponding to receiver A and green corresponding to receiver B. Black points surrounding receivers are random point source locations. 0° corresponds to direction pointing right along the blue dotted line connecting receivers. [**ER**] chap1/. syn-mod

The first example is the ideal situation where there are sources evenly illuminating the receivers from all directions (Figure 1.1). Receiver B is the virtual source location (green) and receiver A is the receiver location (red). First, I model the responses at

both receivers as a function of source azimuth (Figures 1.2a-b). Note that the arrival times of the individual sources are random. Next, I cross-correlate the responses from each source separately and plot the results by source azimuth (Figure 1.2c). This gather is referred to as a correlation gather, and the associated traveltimes now vary smoothly over source azimuth (unlike in the previous receiver gathers). Next, I average traces across all source azimuths in the correlation gather (Figure 1.2d), which results in peaks at -0.8 and -0.8 s. Given the model parameters, this is the expected response (and its time-reversed version) had there been a source at receiver B recorded by receiver A (Equations 1.1 and 1.2).

From the correlation gather and the resulting average, it is clear that the primary contribution to the final EGF between the receivers comes from sources near 0° and 180°. These are the sources that are approximately in-line with the orientation of the receiver pairs. Contributions of the events near these angles constructively interfere, while contributions of events outside of these angles destructively interfere. These regions in-line with the receivers are referred to as stationary phase regions, or Fresnel zones. Sources in these regions emit energy that pass through one receiver before continuing on to the other receiver.

Oftentimes in practice, noise sources are not evenly distributed around receivers. For instance, the ambient seismic noise field can be dominated by ocean waves interacting with the coastline in certain locations, in which case the stronger noise sources are located in a limited range of azimuths relative to the receiver pair. I will take a look at the two extreme cases where strong sources are located in-line with the receivers and where they are perpendicular to the orientation of the receivers.

When strong noise sources are located in one of the stationary phase regions (left of receivers in Figure 1.3a), the correlation gather (Figure 1.3b) is dominated by the sources at those azimuths. The resulting average of the correlation gather (Figure 1.3c) reveals a single dominant arrival at -0.8 s, which is the expected response for the time-reversed Green's function if receiver B was the virtual source and receiver A was the receiver. Thus, when energy propagates through the receiver location before reaching the virtual source location, the resulting EGF contains a peak at negative time lags. Similarly, when energy propagates through the virtual source location before reaching the receiver location, the resulting EGF contains a peak at positive time lags. Though the EGF here is not symmetric over time lag (as theory suggests),

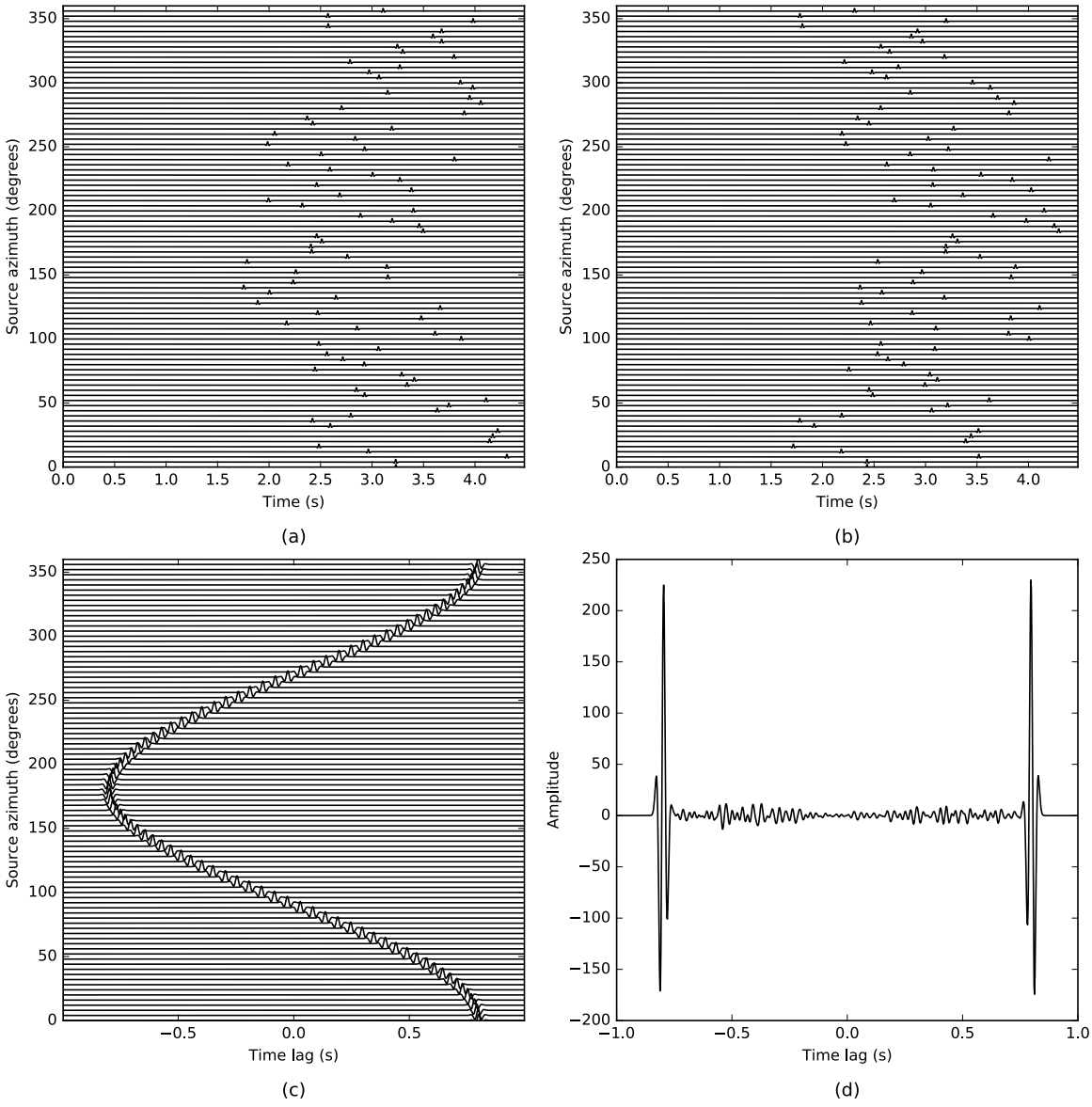

Figure 1.2: Interferometry with even illumination from sources surrounding the two receivers (see Figure 1.1). (a) Responses at receiver A as a function of source azimuth. (b) Responses at receiver B as a function of source azimuth. (c) Cross-correlation of responses at receivers A and B as a function of source azimuth. (d) Average of correlation responses. [**ER**] chap1/. even

the arrival time at negative time lags is still reliable because one of the stationary phase regions is strongly illuminated by noise sources. This example shows that while theory requires sources surrounding the receivers, the primary contributions to the EGF are from stationary phase regions.

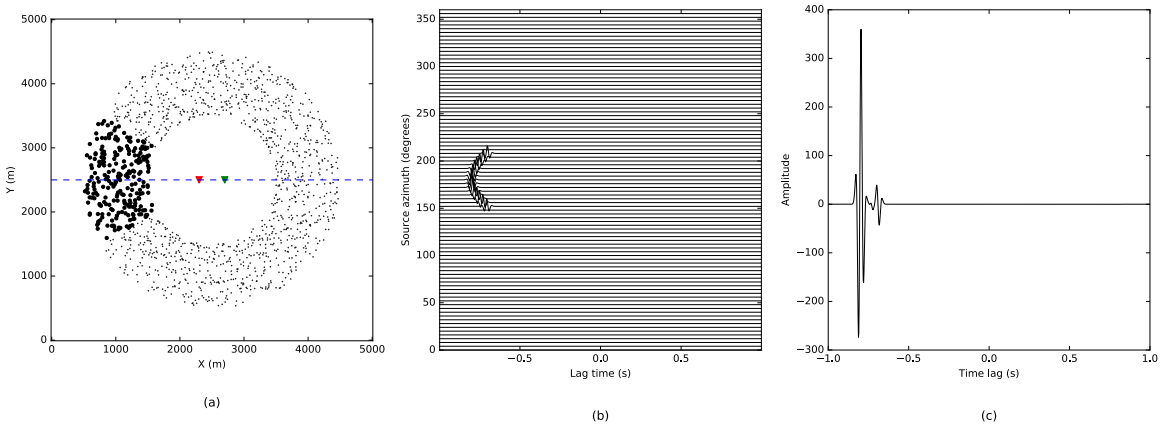

Figure 1.3: Interferometry with strong illumination from sources in-line with and to the left of the receivers. (a) Model geometry, with strong noise sources depicted by larger points. (b) Cross-correlation of responses at receivers A and B as a function of source azimuth. (c) Average of correlation responses. [**ER**] chap1/. inline

When strong noise sources are located perpendicular to the orientation of receivers (Figure 1.4a), the correlation gather (Figure 1.4b) is dominated by sources at those azimuths. Unlike in the previous example, the resulting average of the correlation gather (Figure 1.4c) shows no strong peaks at the expected arrival times (-0.8 and 0.8 s). Instead, the EGF contains energy at earlier arrival times than expected. These events are artifacts of having strong sources outside of the stationary phase locations and are not representative of the true Green's function between the two receivers. Signals from sources outside the stationary phase locations do not first propagate to one receiver then continue to the other, but rather reach both receivers at similar times. These two examples indicate the importance of understanding the noise source locations relative to receiver orientations prior to interpreting the EGFs. If passive seismic interferometry is blindly applied, the accepted traveltime measurements in the EGFs could be artificially early. Chapter 2 takes multiple approaches to characterize the ambient seismic noise field in a complex urban environment prior to applying passive seismic interferometry.

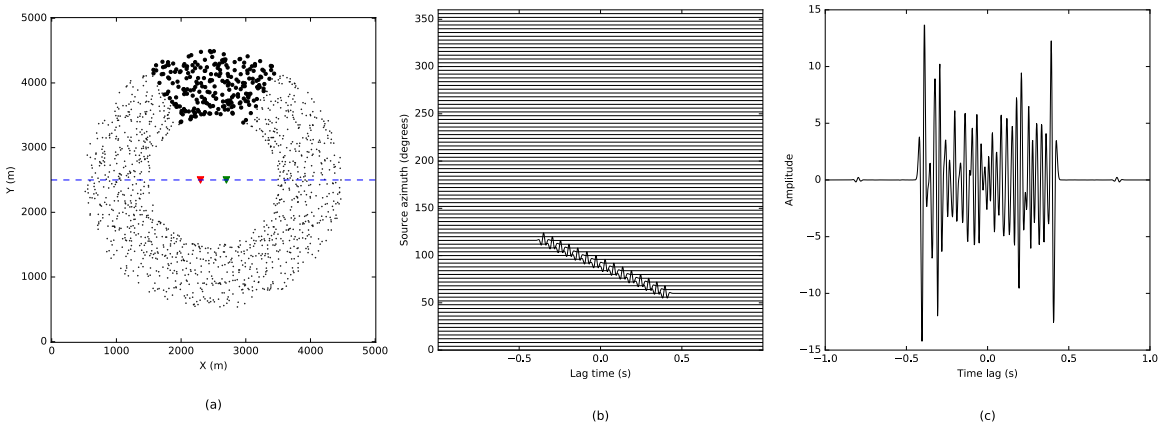

Figure 1.4: Interferometry with strong illumination from sources perpendicular to the line connecting the receivers. (a) Model geometry, with strong noise sources depicted by larger points. (b) Cross-correlation of responses at receivers A and B as a function of source azimuth. (c) Average of correlation responses. [**ER**] chap1/. xline

Note that these 2D synthetic examples also generalize to 3D examples, with stationary phase regions becoming stationary phase volumes. These 2D synthetic examples also hold for body waves, assuming that there is a reflector below the surface and that noise sources also emit body-wave energy. Whereas the stationary phase locations for surface waves and diving waves are anywhere outside and in-line with the receiver orientation, the stationary phase locations for reflected waves are regions in-line with the receivers that produce specular reflections between the two receivers (Nakata et al., 2011; Draganov et al., 2013). For critical refractions, the stationary phase locations are in regions at the critical refraction angle above the receivers. While the same distant critical refraction could be recorded by the receivers, their cross-correlation results in a virtual refraction that has an origin time of 0 s (Mikesell et al., 2009). Chapter 5 discovers critical refractions in microseisms recorded by a deep-water, long-offset array and models a possible method for their natural generation.

Interferometric processing

In practice, the ambient seismic noise field is not composed of individual impulsive sources, but rather of simultaneously acting noise sources. When these noise sources

are uncorrelated in time, averaging over the cross-correlations of recordings of individual noise sources (as done in the previous examples) can be replaced by a single cross-correlation over a long period of time during which noise sources from all directions are recorded.

From this point, there are a number of processing steps that can be performed to improve the quality of the final EGFs. One is to divide individual continuous recordings of ambient seismic noise into short, overlapping time windows, called Welch's method (Welch, 1967). Each subset of continuous recordings is cross-correlated with corresponding recordings from other receivers, with the resulting correlations from each subset averaged to obtain the final EGF. Using Welch's method for seismic interferometry has a number of benefits compared to a single cross-correlation of a long time series. Among them is that high-amplitude transient events (such as earthquakes and instrument spikes) have less effect on the final EGF when they are part of an ensemble average and that this approach appears to lead to faster convergence of EGFs (Seats et al., 2012).

Another major processing decision is how to perform the cross-correlation procedure. While a simple cross-correlation performs well in theory where there is even illumination from all directions, the procedure is susceptible to prevalent monochromatic sources (e.g., electrical noise), biases in the frequency content of the signal (e.g., due to frequency bandpass filters) and general amplitude inaccuracies due to poor coupling of instruments. These are common issues in seismic field data. An alternative approach is to calculate the cross-coherence between continuous recordings rather than the cross-correlation. This approach is equivalent to whitening the spectra of the input recordings by a smoothed version of their respective amplitude spectra (Bensen et al., 2007; Seats et al., 2012). Though the amplitude information is lost, the phase information is maintained. The result is often a more robust, broader-band EGF than from standard cross-correlation. Throughout this thesis, I employ both Welch's method and cross-coherence for passive seismic interferometry.

IMAGING

After successfully performing passive seismic interferometry for each receiver pair in an array, the result is a full virtual seismic survey with a virtual source located at

every receiver position. In practice, the corresponding virtual source gathers are often dominated by surface waves. By measuring the arrival time of the surface waves between each receiver pair, tomography can be performed to produce high-resolution velocity maps (e.g. Shapiro et al., 2005; Lin et al., 2008; de Ridder and Dellinger, 2011). Surface waves are often dispersive (velocity varies with frequency) in practice, as lower frequencies correspond to longer wavelengths that sense deeper, typically faster material. Therefore, by focusing on traveltimes of surface waves at different frequencies, velocity maps corresponding to a range of depths can be generated. In addition to velocity maps, it is also common to invert the dispersion curves associated with the extracted surface waves for a 1D shear-wave velocity profile of the subsurface (e.g., Mordret et al., 2013; Lin et al., 2013). In Chapter 3, I use traveltimes associated with traffic-induced Rayleigh waves in a straight-ray tomography procedure to generate shallow group velocity maps.

Though body waves are more rarely extracted from the ambient seismic noise field, they can in theory be used just like body waves from active seismic surveys to image the subsurface. For instance, Draganov et al. (2013) and Nakata et al. (2011) migrated reflections extracted from the ambient seismic noise field to produce seismic images of the subsurface. The critical refractions in Chapter 5 could potentially be used for refraction tomography.

THESIS OVERVIEW

The primary goal of this thesis is to showcase the ability of passive seismic interferometry to extract wave modes beyond microseism surface waves. To show this, I apply the technique to three different field data sets in three different acquisition environments. The remainder of this thesis is organized as follows:

Ambient noise characterization in an urban environment

Understanding the ambient seismic noise field is vital to the interpretation of EGFs from passive seismic interferometry. In Chapter 2, I characterize the complex spatial and temporal characteristics of the ambient seismic noise field recorded by the dense Long Beach, California, passive seismic array. Because of the array's proximity to the Pacific Ocean and its urban setting, I focus on a broad range of frequencies between

$0.5 - 15$ Hz. Power spectral density maps reveal the location of strong sources within the array. Spectrograms from subsets of recordings within the array reveal how these sources of seismic noise change over time. Beamforming reveals the direction of propagation of ambient seismic noise across different parts of the array.

Ambient noise tomography using traffic noise

In Chapter 3, I perform passive seismic interferometry on ambient seismic noise recordings from the Long Beach array for frequencies between $3 - 4$ Hz. The resulting virtual source gathers contain both fundamental and first-order mode Rayleigh waves induced by local road traffic. Focusing on the fundamental mode, I tailor my traveltime selection criteria based on the ambient seismic noise field characteristics from Chapter 2. Using the selected traveltimes, I perform straight-ray tomography to generate near-surface group velocity maps. I then compare the velocity maps to a geologic map of the region.

P-wave extraction in a shallow marine environment

Because the sea-surface and the sea-bottom act as a waveguide, high-frequency P-waves can propagate long distances through the ocean with little attenuation. In Chapter 4, I perform passive seismic interferometry with phase-weighted stacking on continuous recordings from the Forties shallow-water ocean-bottom node array to extract high-frequency ($40 - 200$ Hz) P-waves. I create virtual source gathers along different source-receiver azimuths for different time periods to determine the directionality of the P-wave events as they cross the array. In an attempt to extract a 1D reflection profile from these P-waves, I adapt the traditional passive fathometry approach for horizontally oriented arrays.

Body-wave extraction in a deep-water marine environment

Though microseisms are typically dominated by surface waves, they can also contain body waves. In Chapter 5, I perform multi-component passive seismic interferometry on continuous recordings of microseisms from the Moere Vest long-offset, deep-water

ocean-bottom node array. Virtual source gathers reveal three different wave modes: Scholte waves, guided acoustic waves, and critical refractions. Given that the latter two events have rarely been extracted from the ambient seismic noise field, I outline evidence for the classification of each wave mode. I then model wave propagation through a simplified elastic model of the region to test a hypothesis for the natural generation of critical refractions.

Appendices

In Appendix A, I show that the virtual super-source gather from the Long Beach array reveals a diving P-wave that originates primarily from northwest of the array. In Appendix B, I show virtual source gathers derived from the microseism energy recorded by the Long Beach array.

Chapter 2

Urban ambient noise characterization

An understanding of the ambient seismic noise field is critical for interpreting the quality and reliability of estimated Green's functions from passive seismic interferometry. In this chapter, I investigate the spatial and temporal characteristics of the ambient seismic noise field recorded by a unique dense seismic array in Long Beach, California. Power spectral density maps, spectrograms, and beamforming analysis in such an urban environment reveal two general sources of continuous seismic energy. The first is ocean-generated noise, which originates from outside the array and influences all recordings at lower frequencies (less than 2 Hz). The second is human-generated noise, which is generated within the array and influences nearby receivers at higher frequencies (greater than 2 Hz). The groundwork laid in this chapter will help guide the preprocessing steps taken when performing tomographic inversion of fundamental Rayleigh waves in the next chapter.

INTRODUCTION

To accurately estimate Green's functions from the ambient seismic noise field, noise sources must be evenly distributed around the receivers, excite all wave modes with equal energy, and be uncorrelated in time (Lobkis and Weaver, 2001; Wapenaar, 2004; Snieder et al., 2010). In this ideal case, noise sources in regions in-line with the two receivers (called the Fresnel zones) contribute most to the estimated Green's function

(EGF), as the noise sources outside these regions destructively interfere with each other (Snieder, 2004; Wapenaar et al., 2010). While these conditions are rarely met in practice, acceptable EGFs can still be obtained when the distribution of noise sources spans at least one of the Fresnel zones (Stehly et al., 2006; Garnier and Papanicolaou, 2009). Thus, the reliability of EGFs from passive seismic interferometry is highly dependent on the temporal and spatial distributions of noise sources.

While ambient seismic noise originates from a number of different sources, two particular sources tend to dominate the recorded data: ocean waves and human activity. Seismic noise generated by the former source is often referred to as microseisms and occurs when ocean waves interact with each other to produce pressure variations at the sea bottom (Longuet-Higgins, 1950) or when ocean waves interact with the shoreline (Hasselmann, 1963). This energy is generated continuously, recorded everywhere, and typically found at frequencies below 2 Hz. Because this particular noise source is located in the oceans, the corresponding seismic energy tends to propagate perpendicular to the coastline on land (Sabra et al., 2005b; Lin et al., 2009) and across all azimuths in marine environments (Mordret et al., 2013; de Ridder and Biondi, 2015). These ocean waves also generate the strongest seismic signals during times of stormy conditions (Gerstoft et al., 2008b; de Ridder and Dellinger, 2011). While most microseisms propagate as surface waves (e.g., Blaik and Donn, 1953; Friedrich et al., 1998; Ekström, 2001), they can also propagate as body waves (e.g., Toksöz and Lacoss, 1968; Landès et al., 2010).

On the other hand, seismic energy originating from anthropogenic sources such as vehicle traffic on land (e.g.. Halliday et al., 2008; Nakata et al., 2011) and shipping and platform noise in marine environments (e.g., Wenz, 1972; Hildebrand, 2009) is typically found at frequencies above 2 Hz. This seismic energy often propagates as surface waves (e.g., Halliday et al., 2008; Behm et al., 2014), although it has also been found to propagate as body waves in both land and marine environments (e.g., Nakata et al., 2011; Mordret et al., 2013). Unlike ocean waves, though, human activity is often highly localized in time and space, making their resulting seismic energy challenging for use in passive seismic interferometry. Thus, careful analysis of noise sources is critical for any ambient seismic noise study, particularly in areas where there is much human activity.

Such an area is Long Beach, California, which is an urban metropolis along the

Pacific Ocean. In January 2012, NodalSeismic deployed a seismic array throughout the city (Figure 2.1). The array spanned an 8.5 km $\times$ 4.5 km region and consisted of approximately 2400 vertical-component geophones with 10-Hz corner frequency and an average receiver spacing close to 100 m. While many ambient seismic noise studies have been performed on land, there have been very few that have benefitted from seismic data recorded by such a large and dense array, let alone in such an urban environment. The use of a non-invasive technique like passive seismic interferometry in this type of densely-populated environment can have a large impact in fields such as earthquake hazard assessment

Given the importance of understanding noise sources for passive seismic interferometry, particularly in the presence of human activity, this chapter focuses on exploiting the density, dimensions, and location of the Long Beach array for pinpointing various noise sources and their influence on the ambient seismic field in both time and space. First, I elaborate on the continuous recordings from the array. I then compute power spectral densities (PSD) of recorded ambient seismic noise, creating both PSD spatial distribution maps to locate potential sources of noise and spectrograms to observe how they vary over time. Finally, I apply beamforming on the raw recordings to determine the slowness and azimuthal distribution of seismic energy propagating from these noise sources.

LONG BEACH CONTINUOUS RECORDINGS

As previously mentioned, the dense Long Beach array consists of approximately 2400 vertical-component geophones and has an average geophone spacing close to 100 m (Figure 2.1). Each geophone recorded continuously for a three-month period and at a sampling rate of 2 ms, resulting in approximately 48 TB of seismic data. To manage such large amounts of data, I downsampled the data to 16 Hz Nyquist frequency and segmented continuous recordings from each geophone into non-overlapping, Hanning-tapered two-hour time windows.

Comparison of the raw, frequency-bandpassed data at midnight (Figure 2.2) and at noon (Figure 2.3) on January 17, 2012, reveal a number of interesting patterns. Note that amplitudes are scaled and clipped differently across the different frequency ranges to account for the 3 Hz low-cut frequency filter that had been applied to the

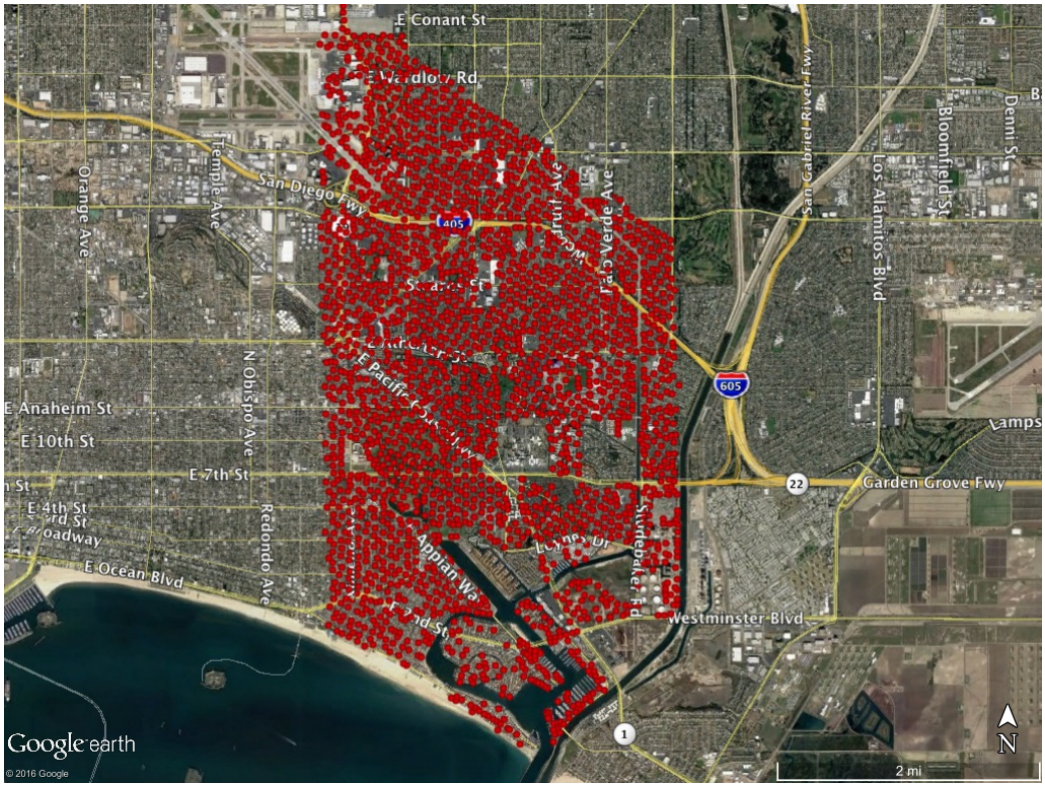

Figure 2.1: Satellite view of receiver locations in the dense Long Beach, California array. [**NR**] chap2/. lb-sat

data, but are comparable across different time periods. For frequencies between 0.5-1.0 Hz (left panels), a continuous but random wavefield is observed at both times across the entire array. This is likely microseism energy, and it appears to be approximately the same strength throughout the entire day.

For frequencies between 3-4 Hz (middle panels), there are high seismic amplitudes in the northern part of the array, which corresponds to an area Interstate 405 passes over. The fact that the amplitudes are higher during the daytime than during the nighttime further suggests that this energy is likely directly related to traffic from the highway. Additionally, there appears to be some high amplitudes during the daytime in the southeast section of the array. Though there are roads in that area, they are unlikely to be as popular as Interstate 405. These relatively high amplitudes could be more indicative of site amplification effects from the artificial fill associated with Alamitos Bay (California Department of Conservation, 2012) than the direct amount of noise from traffic in that area.

For frequencies between 14-15 Hz (right panels), there are high seismic amplitudes with roughly linear patterns at both times. During the night, the high amplitudes appear to coincide with Interstate 405 cutting across northern part of the array and with Studebaker Road along the east side of the array. During the daytime, there are higher seismic amplitudes recorded throughout the array, and they appear along other major roads in addition to those previously mentioned. Thus, traffic noise likely drives the ambient noise field at these frequencies.

Overall, it appears that microseism energy dominates the ambient seismic noise field at lower frequencies while energy from traffic dominates at higher frequencies, as expected. In the next section, I look to examine the continuous recordings in the frequency domain in order to pinpoint the spatial and temporal distributions of these noise sources at Long Beach.

FREQUENCY ANALYSIS OF AMBIENT NOISE

Generating and examining noise power spectral densities (PSD) is the standard method for quantifying seismic background noise (McNamara and Boaz, 2005). PSD reveal how power in a signal is distributed over a range of frequencies. Before calculating the PSD at each receiver, I prepare the recordings by segmenting the previous

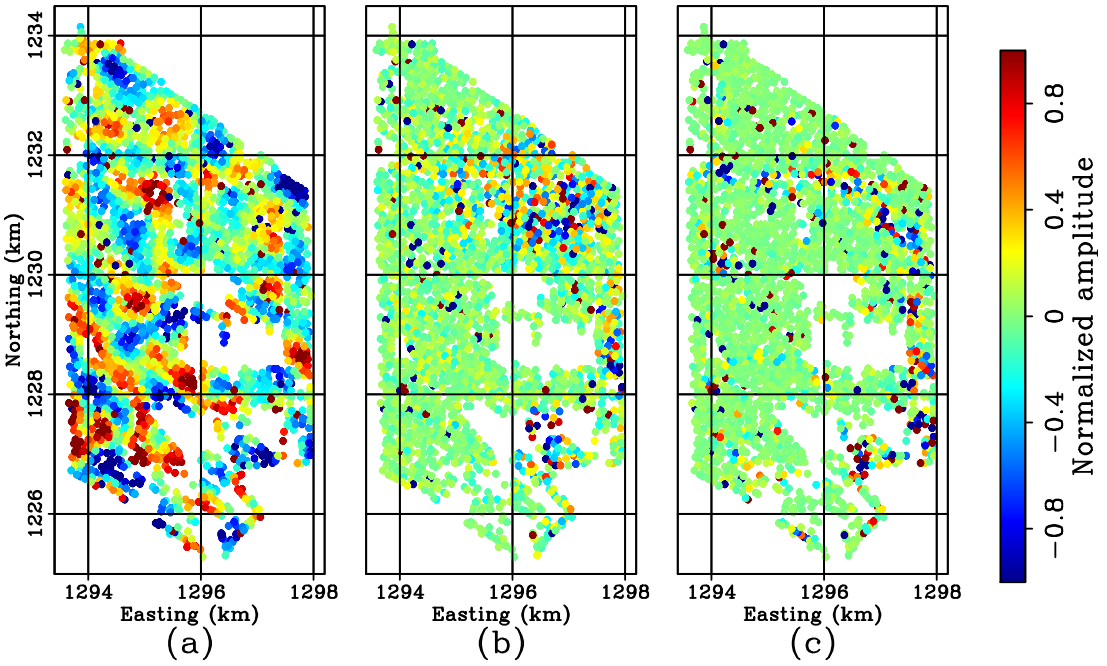

Figure 2.2: Snapshots of the raw data at 00:00 PST on January 17, 2012. (a) 0.5-1 Hz. (b) 3-4 Hz. (c) 14-15 Hz. The amplitudes are clipped and scaled independently from panel to panel to account for the low-cut frequency filter. [**CR**] chap2/. lb-208-snaps

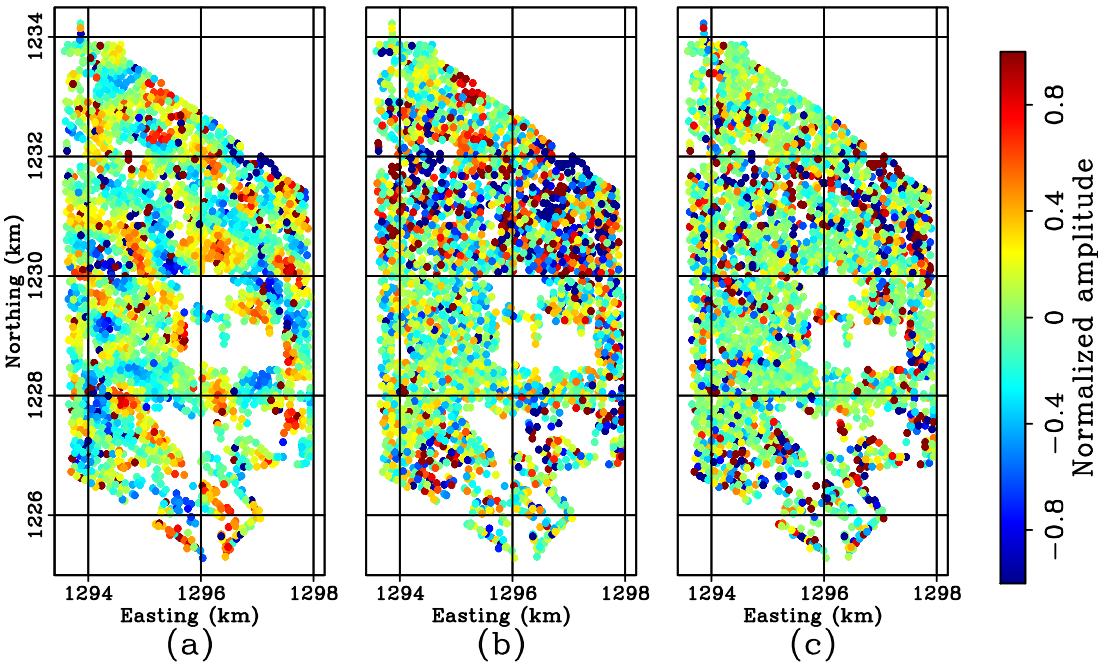

Figure 2.3: Snapshots of the raw data at 12:00 PST on January 17, 2012. (a) 0.5-1 Hz. (b) 3-4 Hz. (c) 14-15 Hz. The amplitudes in each panel are clipped and scaled in the same manner as their counterparts in Figure 2.2. [**CR**] chap2/. lb-214-snaps

two-hour time windows into 5-minute patches with 50% overlap. Next I subtract the mean from each time segment to remove any systematic offset or zero-frequency component. I then apply a smooth Hanning taper to each time segment to reduce artifacts when performing a Fourier transform on a truncated time series. To compute the PSD for a time segment, I take the one-dimensional, discrete Fourier transform and then compute the square of the complex amplitude.

PSD Spatial Distribution Maps

To pinpoint potential sources of noise at Long Beach, I generate spatial distribution maps of the noise PSD by plotting them at their receiver locations. I average the PSD derived from 47 consecutive overlapping 5-minute time segments to obtain a single PSD for a given two-hour time window. By averaging over multiple overlapping time segments, I decrease the variance in the PSD estimates and reduce the influence of spurious events. Much like the plots of the frequency-bandpassed recordings in the previous section, I show results from two different time windows to get a sense of how the spatial distribution of spectral power differs between calmer periods of human activity (00:00 to 02:00 PST of January 17, 2012; Figure 2.4) and periods of peak human activity (12:00 to 14:00 PST of January 17, 2012; Figure 2.5). As before, amplitudes are scaled and clipped differently across the different frequencies to account for the 3 Hz low-cut frequency filter that had been applied to the data, but are comparable across different time periods.

The PSD spatial distribution maps reveal regions where high amounts of seismic energy are being recorded and potentially produced. At 1 Hz (left panels), much of the energy can be found along the coastline, suggesting that microseism energy originating from the Pacific Ocean dominates at these low frequencies. Additionally, energy along the coastline and throughout the array at this particular frequency appears to be stronger during the daytime than during the nighttime. Given that human activity is more prevalent during the daytime hours, there is potential that 1 Hz is near the transition frequency at which ambient seismic noise sources shift from primarily dominated by ocean waves to human activity.

At 4 Hz (middle panels), there is clearly strong energy localized along all of Interstate 405 (northern region the array) and along Studebaker Road (east side of the

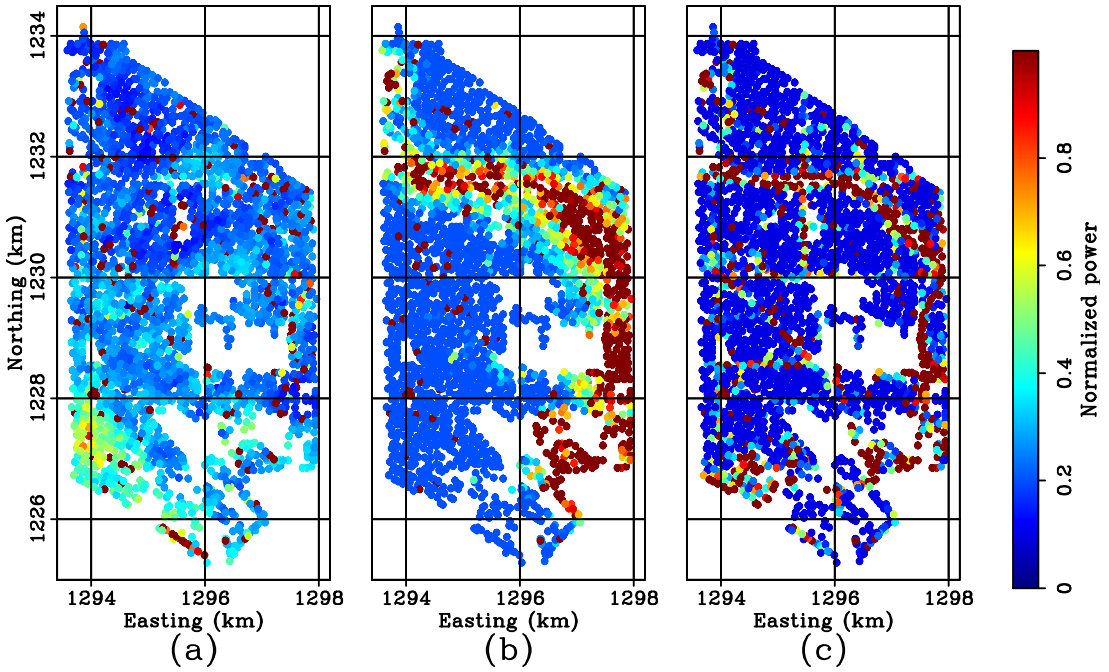

Figure 2.4: Snapshots of averaged PSD between 00:00-02:00 PST of January 17, 2012. (a) 1 Hz. (b) 4 Hz. (c) 15 Hz. The spectral power are clipped and scaled independently from panel to panel to account for the low-cut frequency filter. [**CR**] chap2/. lb-208-fxs

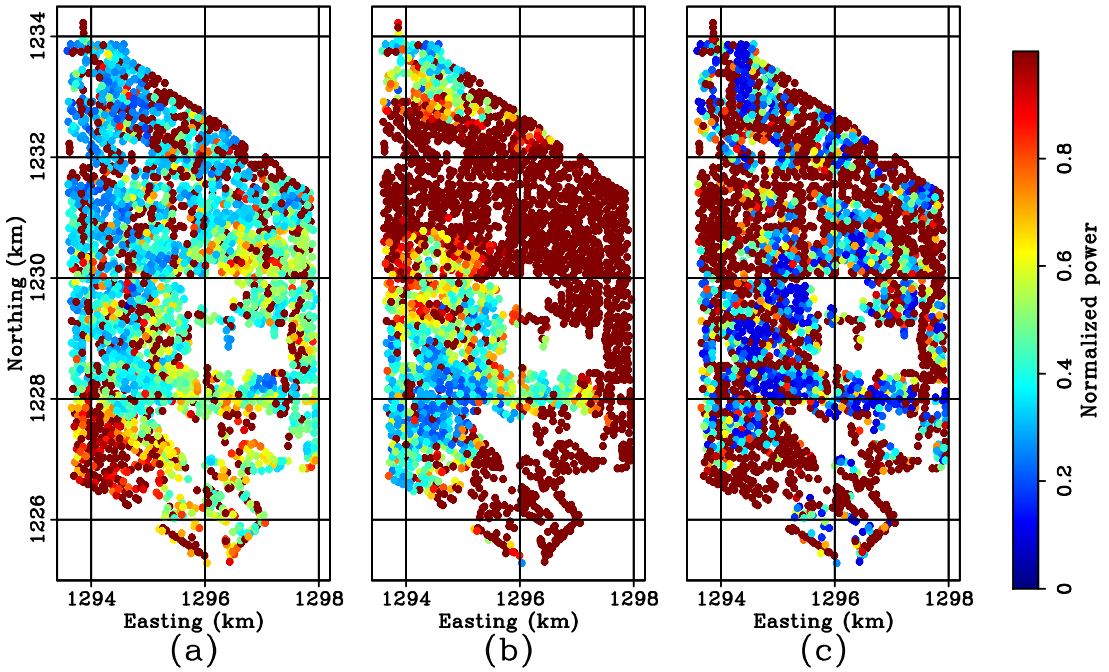

Figure 2.5: Snapshots of averaged PSD between 12:00-14:00 PST of January 17, 2012. (a) 1 Hz. (b) 4 Hz. (c) 15 Hz. The spectral power in each panel is clipped and scaled in the same manner as their counterparts in Figure 2.4. [**CR**] chap2/. lb-214-fxs

array) throughout the day. The extent of the vibrations from these roads reaches significantly further distances during the daytime, when there are many more vehicles on the roads. Furthermore, as in the frequency-bandpassed raw recordings, the southeast region of the array displays strong seismic energy at this frequency during the daytime and to a lesser degree during the nighttime. I previously hypothesized that the high seismic amplitudes in the region were due more to seismic amplification effects of artificial fill than to direct vibrations from traffic. The PSD maps here support this hypothesis, as the border for high spectral power in this region remains fairly consistent (between $1296-1298$ km easting and $1226-1228$ km northing) over time. In other words, the spatial extent of this high spectral power region does not change significantly when there are more cars on the road, suggesting that the seismic energy there is not indicative of more traffic but rather indicative of a geologic boundary. This behavior is different from the regions of high spectral power around Interstate 405, which display greater spatial extent during daytime hours with heavier traffic. Therefore, traffic noise along Interstate 405 and other major local roads appear to dominate the ambient seismic noise field at 4 Hz.

At 15 Hz (right panels), there are high amounts of seismic energy localized at receivers along Interstate 405 and other local roads. The difference in spatial extent of highway energy at 4 Hz and 15 Hz can be attributed to attenuation. The highway energy at 15 Hz is localized because higher frequencies attenuate more rapidly with distance, whereas the highway energy at 4 Hz is more spread out because lower frequencies attenuate more gradually with distance. Much like at 4 Hz, there is generally more seismic energy during daytime hours when there is more traffic, and Alamitos Bay again displays relatively high seismic energy during the daytime, which is likely due more to traffic noise being amplified by artificial fill than to more traffic. Therefore, traffic noise along Interstate 405 and other major local roads appear to dominate the ambient seismic noise field at 15 Hz.

Spectrograms

To better resolve how the ambient seismic noise field at Long Beach changes over time, I generate spectrograms (plots of PSD versus time) for receivers near the coastline (southern circle in Figure 2.6a) and for receivers overlaying a section of Interstate 405 (northern circle in Figure 2.6a) over a three-day period (approximately January

15 – 18, 2012). Each region contains approximately 150 receivers. I first discard recordings in those regions that have maximum PSD amplitudes above a certain threshold, since they will bias the spatial average. I then average the PSD from the remaining receivers in each respective region over all 5-minute time segments and plot the logarithm of the PSD side by side to observe how they change with time. I plot the logarithm of the PSD here to compensate for the 3-Hz low-cut frequency filter applied to the data and allow comparisons to be made across a broad range of frequencies. Additionally, to help examine both the microseisms and anthropogenic seismic energy, I plot spectrograms up to 2 Hz (Figure 2.7) and up to 15 Hz (Figure 2.8), respectively, and scale and clip their values independently from each other. Note that the vertical streaks in these spectrograms are from the original segmenting of the data into tapered two-hour windows.

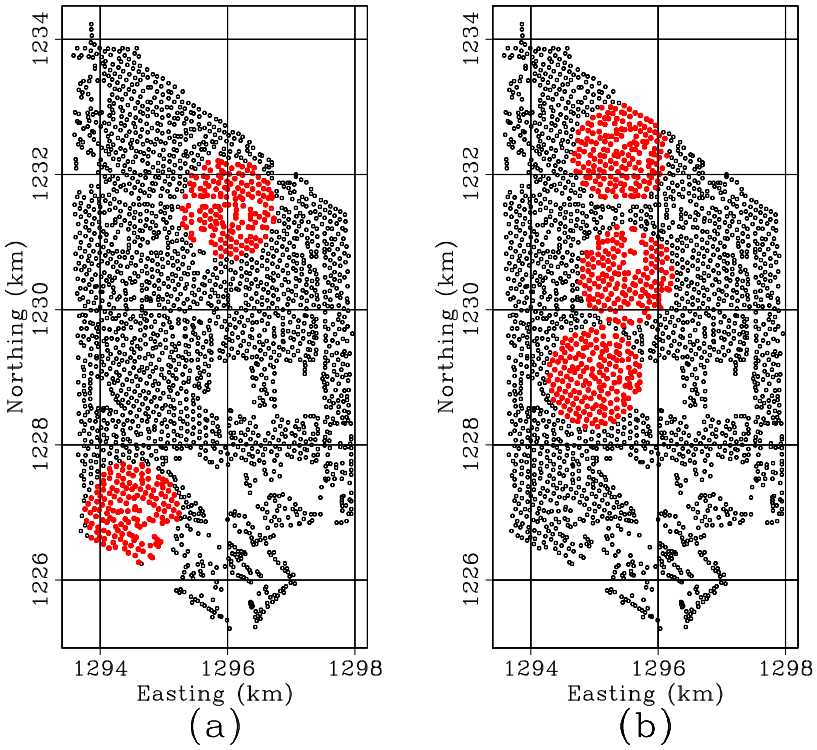

Figure 2.6: Map of the Long Beach array with subsets of stations used for (a) spectrograms and (b) beamforming, colored red. [**CR**] chap2/. lb-map-overlays

Focusing on frequencies below 2 Hz (Figure 2.7), there is consistent seismic energy across all times and both receiver subset locations. The energy appears at frequencies down to approximately 0.3 Hz, although it could exist at even lower frequencies given that a 3-Hz low-cut frequency filter had been applied to the data. The minor

fluctuations in seismic energy over time, including around 1 Hz, do not appear to have a consistent and clear diurnal pattern, suggesting that the observed differences in PSD maps at low frequencies during daytime and nighttime hours (left panels; Figures 2.4 and 2.5) are not due to traffic noise. In general, seismic energy at these low frequencies is slightly stronger for receivers near the coast (Figure 2.7a) than for receivers near the highway (Figure 2.7b), which agrees with the findings from the PSD maps. These observations suggest that the seismic energy at low frequencies is likely driven by microseisms and ocean waves hitting the coastline with slight random fluctuations in strength over time.

Focusing on frequencies up to 15 Hz (Figure 2.8), there is a clear diurnal pattern to the seismic energy, with lows during the nighttime and highs during the daytime. This is consistent with typical traffic patterns. While this pattern is observed both near the ocean (Figure 2.8a) and near Interstate 405 (Figure 2.8b), the spectral power is significantly stronger at 4 Hz and above near the highway. These observations provide more evidence that energy at these higher frequencies is related to traffic noise.

Overall, analysis of the PSD of the ambient seismic noise field in both space (through PSD spatial maps) and time (through spectrograms) supports two prominent sources of noise. One is microseisms, whose energy is strongest along the coastline, dominates at frequencies below 2 Hz, and displays slight random fluctuations in strength over time. The other is traffic noise, whose energy is distributed throughout the array (and preferentially along Interstate 405), dominates at frequencies above 2 Hz, and displays diurnal fluctuations in strength over time. With the spatial and temporal distributions of the noise sources now understood, I turn to beamforming to determine the slowness and azimuthal distribution of seismic energy propagating from these sources across the array.

BEAMFORMING

By applying beamforming to the ambient seismic noise data, I can estimate the slowness and azimuth at which seismic energy passes through the array (Rost and Thomas, 2002). The beamforming procedure I use is effectively a series of slant stacks along different azimuths and slownesses in the time domain (Kostov and Biondi,

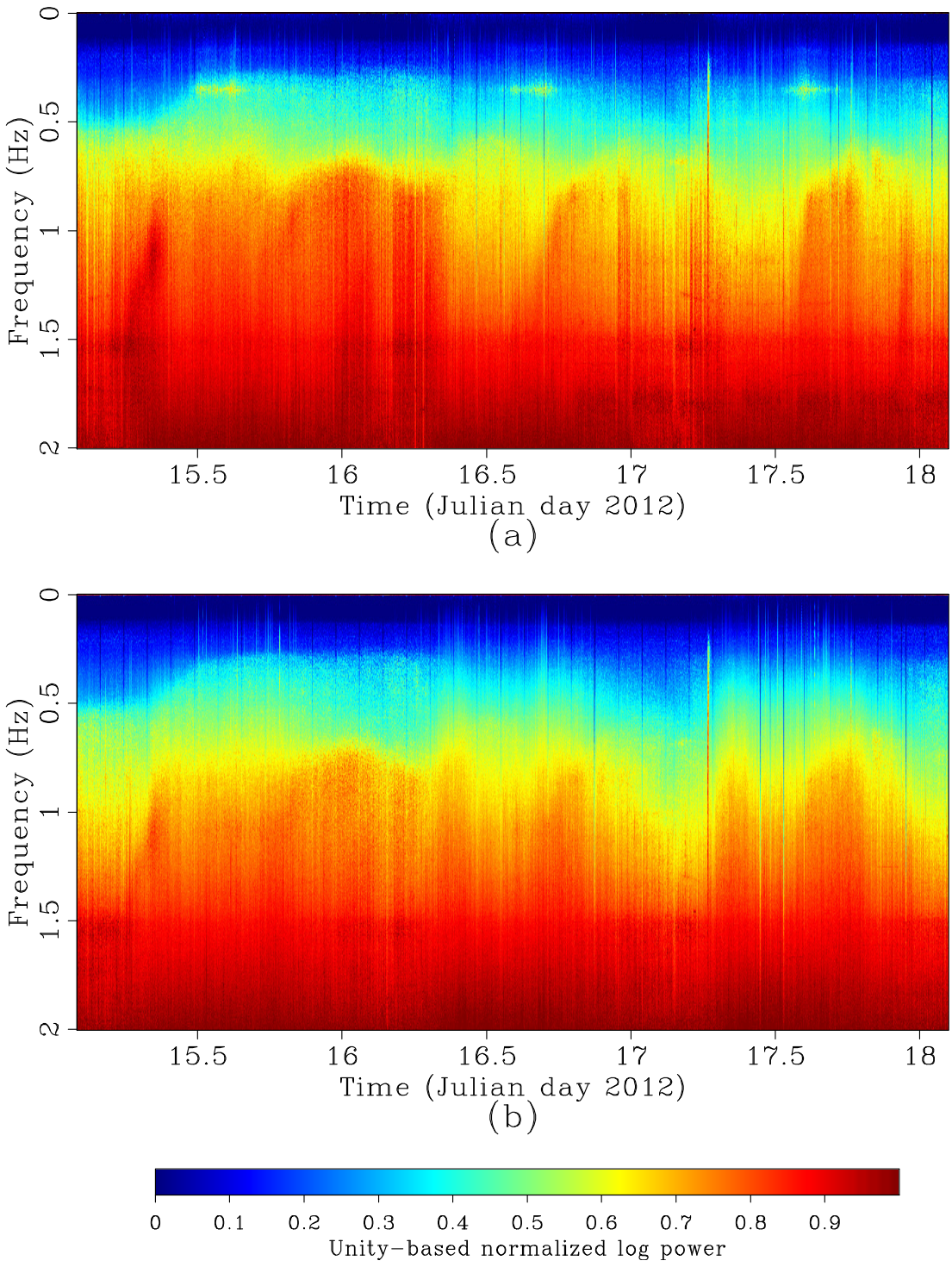

Figure 2.7: Spectrograms up to 2 Hz for subsets of receivers (a) near the ocean and (b) near Interstate 405. Spectral power in both plots are scaled and clipped in the same manner so that they can be compared. [**CR**] chap2/. lb-sps-lo

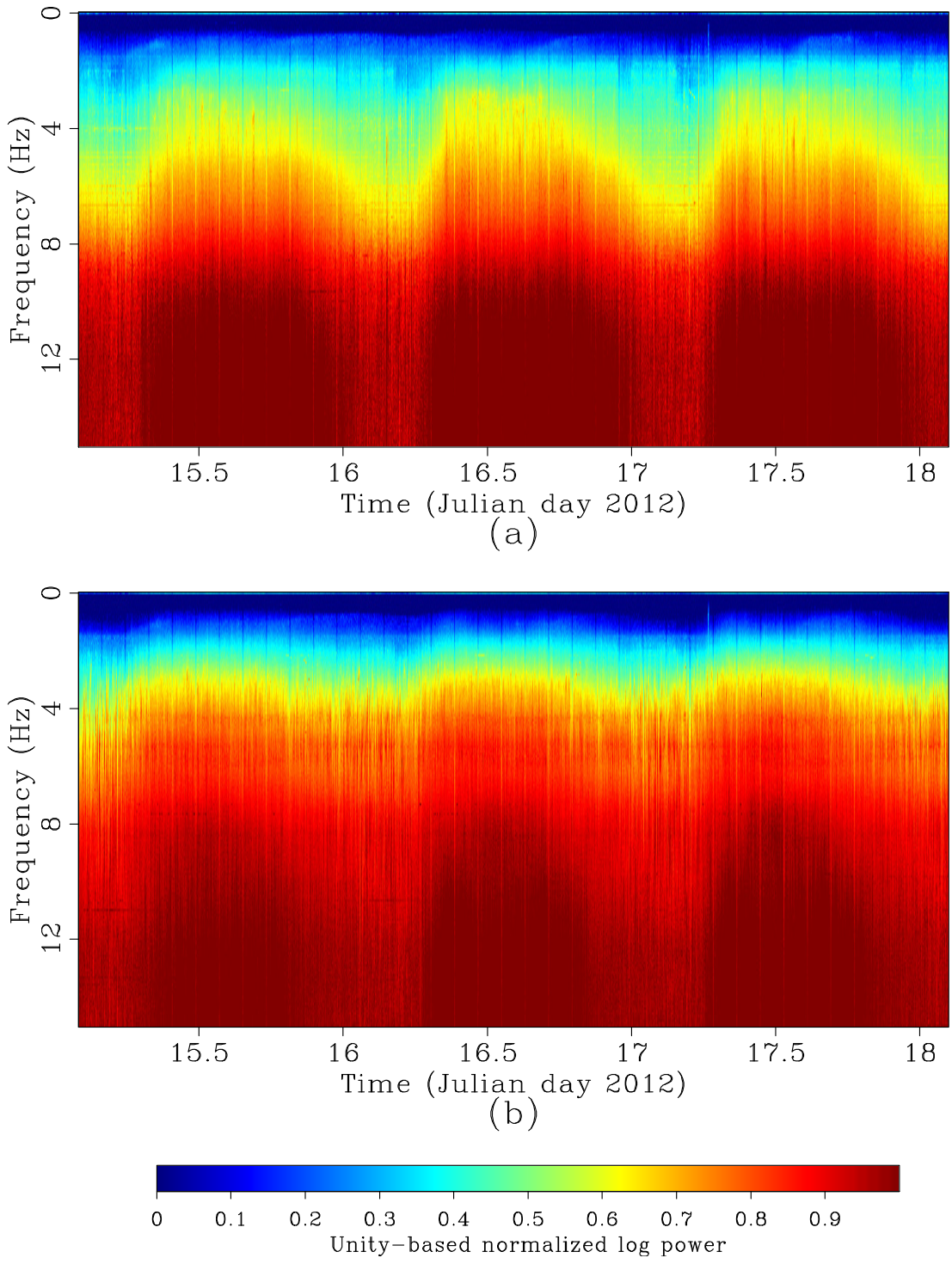

Figure 2.8: Spectrograms up to 15 Hz for subsets of receivers (a) near the ocean and (b) near Interstate 405. Spectral power in both plots are scaled and clipped in the same manner so that they can be compared. [**CR**] chap2/. lb-sps-hi

1987). In equation form, the procedure is expressed as:

$$B(p_x, p_y) = \sum_{j=1}^{T} \sum_{i=1}^{N} \left| U\left(t_j + p_x x_i + p_y y_i\right) \right|, \tag{2.1}$$

where B is the beamformer output power; p_x and p_y are slownesses in the north and east directions, respectively; T is the number of time samples; N is the number of receivers in the array; U is the raw seismic record; x and y are receiver distances in the north and east directions, respectively, relative to some origin; and t is time. If there is signal propagating across the array at a certain slowness and azimuth, it will stack coherently in the beamformer and result in high beam power at those particular slowness values in the north and east directions.

This particular beamforming approach assumes that seismic signals pass through the array as plane waves (and therefore are outside of the array) and are coherent across the entire array. From previous frequency analysis of the raw data, the two major sources of noise at Long Beach are microseisms originating from the Pacific Ocean at low frequencies and traffic noise within the array at high frequencies. Therefore, I perform beamforming on three subsets of receivers in the array (rather than on the entire array) to account for these localized noise sources: one just north of Interstate 405, one just south of Interstate 405, and one in the middle of the array (Figure 2.6b).

I first select multiple two-hour time windows of ambient seismic noise (00:00-02:00 PST and 12:00-14:00 PST on January 17, 2012, as before) recorded at groups of stations throughout the array. I then remove traces with anomalously high amplitudes so they will not bias the beamformer output. I then apply two frequency bandpass filters: one from $0.5 - 1.0$ Hz and one from $3.25 - 3.75$ Hz. The former focuses on the microseism energy while the latter focuses on traffic noise. I do not examine higher frequencies (such as 15 Hz) here because attenuation greatly dampens the signal amplitude as it propagates from roads to across the subarrays. Additionally, aliasing effects are stronger at higher frequencies, which is demonstrated at the end of this section. These two factors lead to weak beamformer output signal that is difficult to interpret. The two-hour, frequency-bandpassed recordings are then put into the beamformer, which produces a map depicting the slowness and azimuthal distribution of noise for those set of receivers.

Figures 2.9 and 2.10 display maps of the beamformer outputs for the low and high frequency ranges, respectively. In both figures, rows from top to bottom correspond to receiver subsets from north to south, respectively, while columns correspond to nighttime (left columns) and daytime (right columns) hours. All panels in Figure 2.9 are clipped identically so that comparisons of beam power at low frequencies can be made between nighttime and daytime hours. However, panels in Figure 2.10 are only identically clipped for the same time of day. In other words, beam power at high frequencies can be compared to each other for a given time of day, but they cannot be compared across different times of the day (across columns). In all panels, the azimuth of high beam power indicates the azimuth from which noise is coming (e.g., an anomaly on the right of the map indicates noise coming from the east) while the radial distance of the anomaly (from zero slowness) represents the apparent slowness at which that signal is traveling across the array.

At the frequency band 0.5-1.0 Hz (Figure 2.9), it is clear that noise is arriving from the southwest at all locations and times. This is yet another indication that the Pacific Ocean is the dominant source of energy at low frequencies and that its influence extends throughout the entire array (although the energy is slightly stronger closer to the coastline). Additionally, the coherent microseism energy appears to be slightly stronger during the nighttime than during the daytime, which suggests that higher spectral power during the daytime (as observed in PSD maps) does not necessarily translate directly to stronger coherent signal passing through the array. One possible reason is that high spectral power in the PSD maps at low frequencies could be incorrectly attributed to microseism source strength rather than site amplification effects or vibrations from random human activity. For this particular frequency band, noise from the ocean arrives generally at a slowness of .001 s/m, or a velocity of 1 km/s. This is likely Rayleigh-wave energy based on the frequency and propagation velocity.

At the frequency band 3.25-3.75 Hz (Figure 2.10), there is more variation in the ambient seismic noise field over time and space. In terms of temporal variation, beam power is significantly higher during the daytime (right columns) than during the nighttime (left columns). Note that this is not directly obvious from the figure, as columns had to be clipped independently in order to draw out other interesting features. This pattern is no surprise given that traffic is heavier during the daytime.

In terms of spatial variation, seismic energy propagates along different azimuths

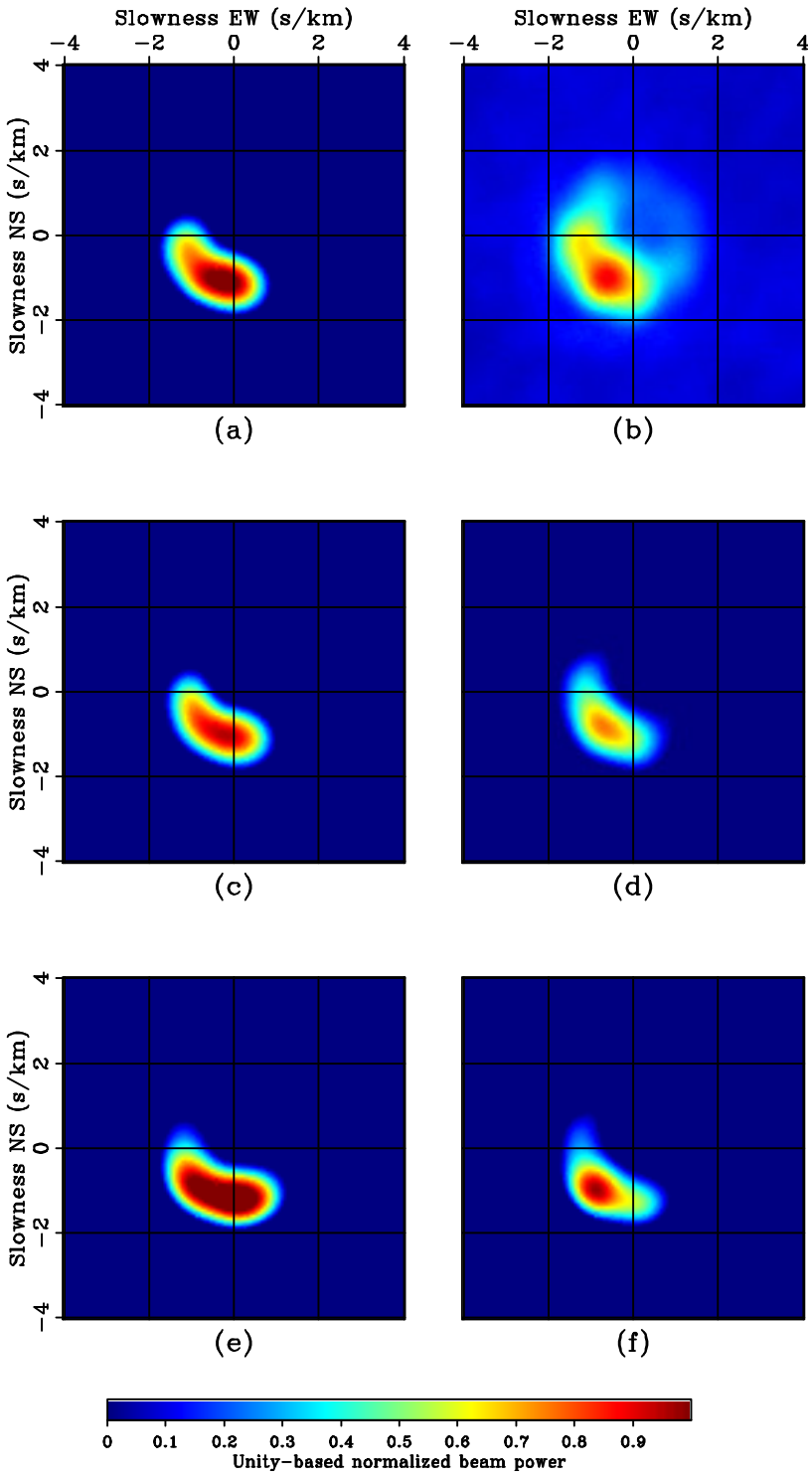

Figure 2.9: Beamforming analysis performed on ambient noise recordings bandpassed for 0.5 Hz to 1.0 Hz. Rows from top to bottom correspond to groups of receivers from north to south in Figure 2.6b. Left columns correspond to nighttime hours and right columns correspond to daytime hours. All panels are clipped identically so they can be compared. [**CR**] chap2/. lb-beam-02freq

at different locations within the array. Receivers just north of Interstate 405 (top row) reveal that coherent energy is primarily approaching from the south, while receivers just south of Interstate 405 (middle row) reveal that coherent energy is primarily approaching from the north. These observations clearly indicate that Interstate 405 is the dominant source of energy for regions near the highway. Further away from the highway (bottom row), seismic energy is better equipartitioned but not as distinguishable from the background energy. This suggests that the weaker but better-distributed local traffic, and not the stronger but localized highway traffic, influences the noise field further away from the highway. This is likely because of attenuation effects on the highway signal, given I am looking at signals at high frequencies.

In each of the high-frequency beamforming results, there are two centered, concentric rings. Because seismic energy associated with these rings appears to mostly propagate along the same directions, these two rings are likely associated with the fundamental and first-order Rayleigh waves, with the former propagating at lower velocities (approximately 350 m/s) than the latter (approximately 500 m/s). These wave modes can be used for tomographic imaging of the subsurface.

The crossing events in primarily the northeast and southwest regions are spatial aliasing artifacts. Given the frequency range of investigation and the apparent velocities of the wave modes, apparent wavelengths are approximately between 100 and 150 m, which are shorter than the minimum wavelength of 200 m (given an average station spacing of 100 m) suggested by the Nyquist sampling theorem to avoid spatial aliasing. To visualize the aliasing effects, I display the beamformer output to a normally-incident plane wave with a frequency of 3.5 Hz in Figure 2.11. As expected, there is a spike in the center of each slowness panel, corresponding to energy reaching all receivers at the same time. However, there are also spikes along the southwest-northeast direction. Since there was no energy modeled at these azimuths and slownesses, these spikes are due to spatial aliasing. The locations of these spikes correspond well with the orientation and slowness offsets of the aliasing artifacts in the field data.

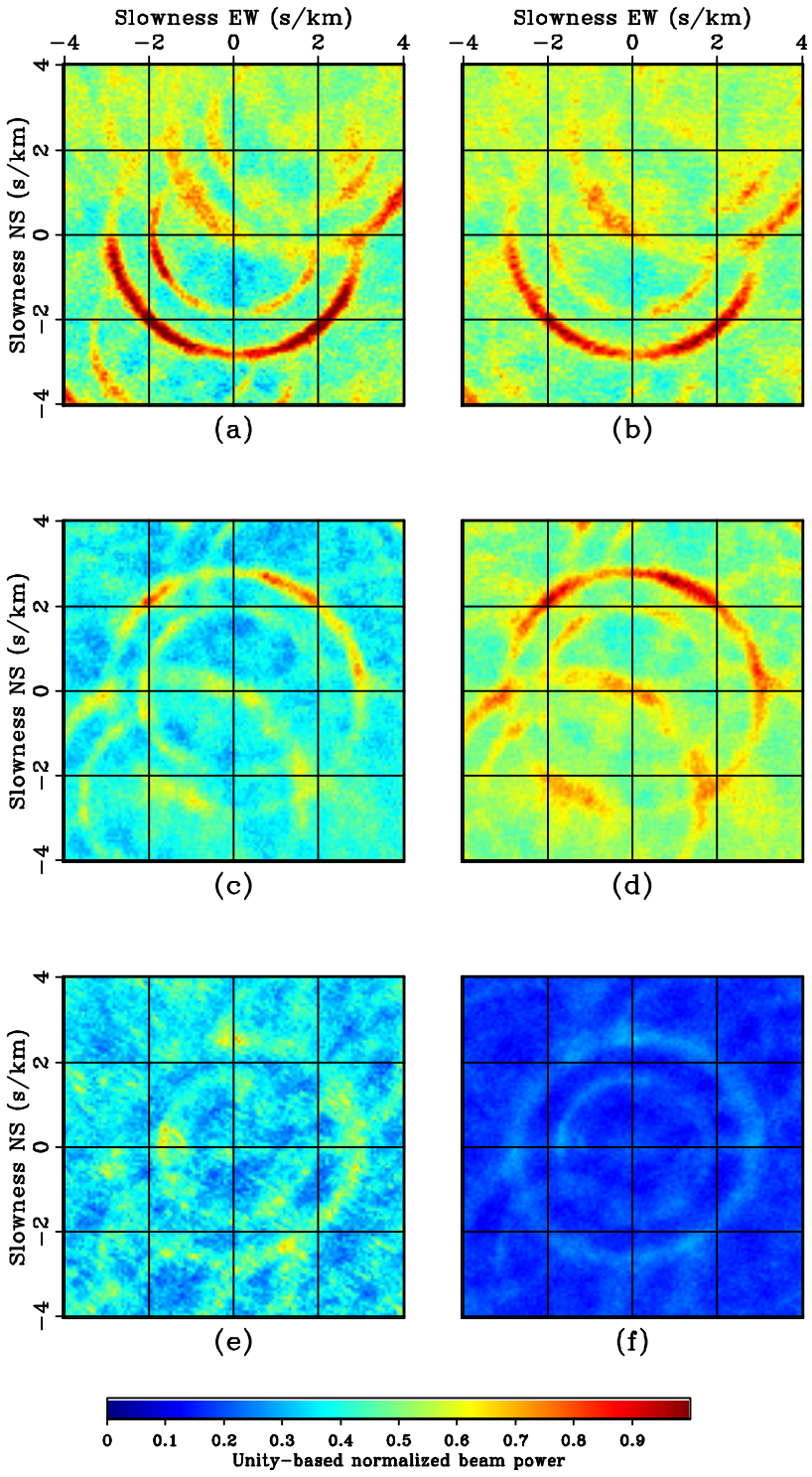

Figure 2.10: Beamforming analysis performed on ambient noise recordings band-passed for 3.25 Hz to 3.75 Hz. Rows from top to bottom correspond to groups of receivers from north to south in Figure 2.6b. Left columns correspond to nighttime hours and right columns correspond to daytime hours. Panels within a given column are clipped identically such that comparisons can be made within a given time of day but cannot be made across different times of the day. [**CR**] chap2/. lb-beam-13freq

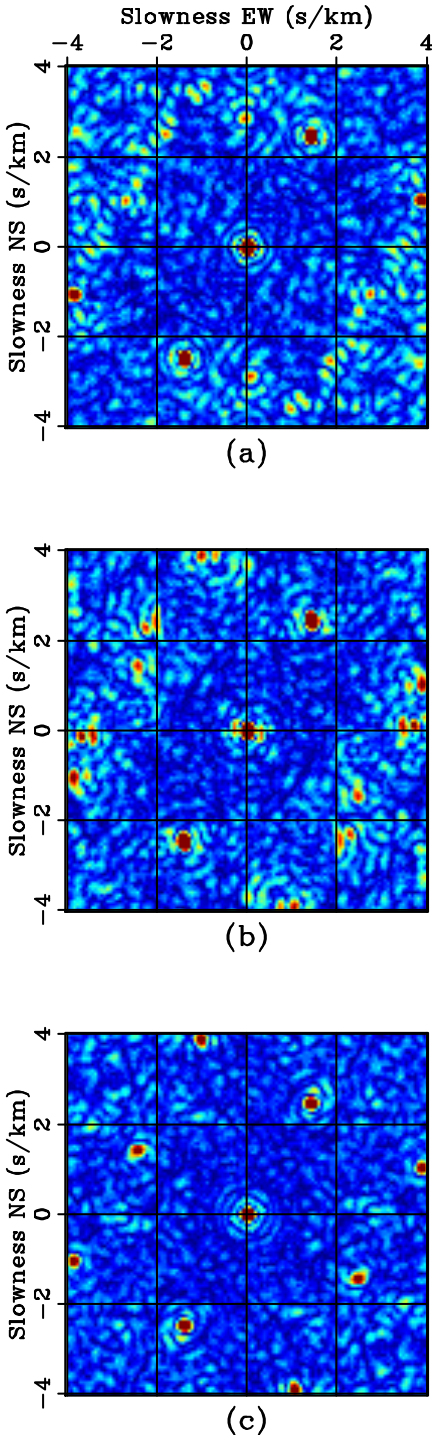

Figure 2.11: Beamforming analysis performed on a normally-incident plane wave with a frequency of 3.5 Hz. Plots from top to bottom correspond to groups of receivers from north to south in Figure 2.6b. Spikes are located not only in the center of the slowness panels but also along a southwest-northeast orientation, particularly near the highway. The orientation of these spikes coincide well with the orientation of beamforming artifacts. All panels are clipped independently to enhance spikes. [**CR**] chap2/. lb-beams-normal

DISCUSSION

Combining the observations from all three analyses (PSD maps, spectrograms, beamforming), it is clear that microseisms dominate the ambient seismic noise field at frequencies below 2 Hz, and traffic noise dominates at frequencies above 2 Hz. The observations here have strong implications for the application of passive seismic interferometry at this site.

With respect to low frequencies, microseism energy in the form of Rayleigh waves appears to be straightforward for use in passive seismic interferometry and subsequent tomography. It is relatively consistent over time (Figure 2.7), which suggests that data from all times can be used when estimating Green's functions. The energy also propagates relatively consistently throughout the entire array (Figure 2.9). Whether near the coastline or near Interstate 405, receivers record the same Rayleigh waves generated by microseisms, which is important when estimating Green's functions from ambient seismic noise. The main challenge is working with the directional propagation of the apparent Rayleigh waves, which is from southwest to northeast. This directionality will likely produce mostly one-sided estimated Green's functions (EGFs) for station pairs oriented roughly southwest-northeast. They will likely be most reliable for station pairs oriented perpendicular to the coastline (Stehly et al., 2006). For station pairs oriented northwest-southeast, it is possible that the EGFs will not be as reliable, as the synthesized Rayleigh waves could arrive too early since the coastline would not be located in one of the Fresnel zones.

While low-frequency microseisms appear to be generally well-suited for extracting reliable EGFs, high-frequency traffic noise at Long Beach is not. While the diurnal pattern of the seismic energy (Figure 2.8) is unlikely to affect the quality of EGFs, the fact that the noise sources (traffic) are spatially localized within the array will have a large and mostly negative effect. The most prominent source of seismic energy at these frequencies is Interstate 405 (top two rows; Figure 2.10), which is only influential near the highway due to attenuation. It is possible to obtain reliable traffic-induced Rayleigh waves between receivers as long as there are sources located in one of the Fresnel zones. Because Interstate 405 curves, many receiver pair orientations near the highway (not just those perpendicular to the highway) could actually yield reliable EGFs. However, receiver pairs on opposite sides of the highway are very unlikely to produce reliable EGFs. The resulting Rayleigh wave arrival times would likely be too

early, as there is effectively an active source between the two receivers (and not in the Fresnel zones). Further away from Interstate 405, the ambient seismic noise sources (local roads) appear to be relatively well-distributed around the receivers (bottom row; Figure 2.10), which suggests that EGFs could be reliable in the southern parts of the array.

It is clear that caution should be exercised when using Rayleigh-wave travel times from EGFs in a tomography procedure. At lower frequencies, receiver pair orientations should be roughly perpendicular to the coastline in order to avoid artificially early travel times. To obtain a reliable Rayleigh wave between two receivers at higher frequencies, the relative distance between receivers cannot be too great because of attenuation, and major roadways like Interstate 405 must be located in at least one of the Fresnel zones. If these conditions are met, surface-wave tomography using these Rayleigh-wave travel times can produce subsurface velocity maps that can help decouple site amplification effects due to geology from noise sources, which could not be done when interpreting the PSD maps.

CONCLUSIONS

Understanding the ambient seismic noise field is important for interpreting estimated Green's functions from passive seismic interferometry and for tailoring preprocessing steps for subsequent tomographic inversion. The dense Long Beach, California, array provides an opportunity for an unprecedented look at ambient seismic noise in an urban environment. From PSD spatial distribution maps, I determined that the major sources of noise energy at Long Beach were the Pacific Ocean at frequencies below 2 Hz, and traffic noise, particularly Interstate 405, at frequencies above 2 Hz. Spectrograms revealed that the ambient seismic noise field at low frequencies is fairly constant, while at high frequencies it goes through diurnal fluctuations in energy that can be attributed to diurnal patterns in human activity. Beamforming analysis showed that noise is consistently arriving from the southwest at low frequencies, further confirming the Pacific Ocean as a dominant noise source. This analysis also showed that high-frequency energy near the Interstate 405 is dominated by the highway. Further away from the highway, the noise arrives at a wider range of azimuths and could potentially be attributed to energy generated from traffic on local roads.

Though there is ample seismic energy propagating throughout the array as Rayleigh waves, caution must be exercised when using resulting estimated Green's functions for tomography. In this sort of environment, there are many receiver pair orientations that will not contain sources in one of the Fresnel zones, particularly at higher frequencies. This will lead to artificially early Rayleigh-wave arrival times, which can harm tomography results. However, with careful travel time picking, it is possible to extract a near-surface velocity map from the ambient seismic noise field. Such a non-invasive technique in such an urban environment could have a potentially large impact in fields such as earthquake hazard assessment.

ACKNOWLEDGMENTS

I would like to acknowledge Signal Hill Petroleum, Inc. and NodalSeismic for allowing me to use the data and to present my results. I especially thank Dan Hollis of NodalSeismic for his help and cooperation throughout the project.

Chapter 3

Ambient noise tomography using traffic noise

By cross-correlating recordings of ambient seismic noise between pairs of receivers, it is possible to obtain an estimate of the Green's function between those two receivers. The wave modes contained in these estimates can then be used for imaging the subsurface. In this chapter, I perform passive seismic interferometry on continuous high-frequency (greater than 3 Hz) seismic recordings at Long Beach, California, to obtain both fundamental and first-order mode Rayleigh waves propagating between individual receiver pairs. I use the resulting traffic-induced fundamental-mode Rayleigh-wave arrival times to generate near-surface group velocity maps that correspond well with known geologic boundaries, including the Newport-Inglewood fault. These maps can be useful for identifying regions that are susceptible to serious damage during earthquake-related shaking. Overall, these results demonstrate the impact a cost-effective, non-invasive technique like passive seismic interferometry can have on densely-populated regions.

INTRODUCTION

Use of the ambient seismic noise field for imaging Earth's shallow structure has gained significant interest in the past decade. Under certain conditions, an estimate of the Green's function between two receivers can be obtained through passive seismic interferometry, which is effectively the cross-correlation of their respective recordings

of ambient seismic noise (Lobkis and Weaver, 2001; Wapenaar, 2004; Snieder, 2004). This estimated Green's function (EGF) is effectively the wavefield that would be recorded at one receiver if the other receiver was acting as an impulsive source. In practice, the dominant wave modes extracted from ambient seismic noise are surface waves in the microseism band (below 2 Hz). A number of studies have used these surface waves to produce high-resolution tomographic images of Earth structures at the regional (e.g., Shapiro et al., 2005; Sabra et al., 2005a) and continental scales (e.g., Lin et al., 2007; Yang et al., 2008; Bensen et al., 2008). The success of these studies has encouraged recent investigation of this technique at the exploration scale. In an ocean-bottom environment, de Ridder and Dellinger (2011) showed that Scholte waves in the microseism band could be used to tomographically image the near surface. Later, de Ridder et al. (2014) and Mordret et al. (2014) used the same types of waves to obtain reliable time-lapse group and phase velocity maps, respectively, of the Valhall overburden, while de Ridder et al. (2015) recovered phase velocity and azimuthal anisotropy maps representative of subsidence patterns at Ekofisk.

In land environments, seismic arrays of sufficient density, size, and recording duration for these types of passive seismic investigations are rare. However, one array in Long Beach, California, met these requirements. Both acquisition phases of this array have produced impressive results from the continuously recorded data. For the first phase, Lin et al. (2013) processed ambient seismic noise recordings up to 4.0 Hz, and they inverted for Rayleigh-wave phase velocity maps for frequencies up to 2.0 Hz and three-dimensional shear velocity cubes. Bowden et al. (2015) showed a phase velocity map at 3.3 Hz using the same approach.

The second phase, which is the focus of this study, had similar survey characteristics as the first phase. Deployed in January 2012 by NodalSeismic, the second phase spanned an 8.5 km $\times$ 4.5 km region and consisted of approximately 2400 vertical-component geophones with 10-Hz corner frequency and an average spacing close to 100 m (Figure 3.1). It recorded ambient seismic noise continuously over a three-month period at a sampling rate of 2 ms. Using passive recordings from this second phase, Nakata et al. (2015) used diving waves to produce three-dimensional P-wave velocity cubes that successfully imaged the Newport-Inglewood Fault (see Appendix A for body-waves at Long Beach). Using data from both acquisition phases, Dahlke et al. (2014) created phase velocity maps at low frequencies (approximately 1 Hz) that resolved the location of the same fault (see Appendix B for low-frequency EGFs).

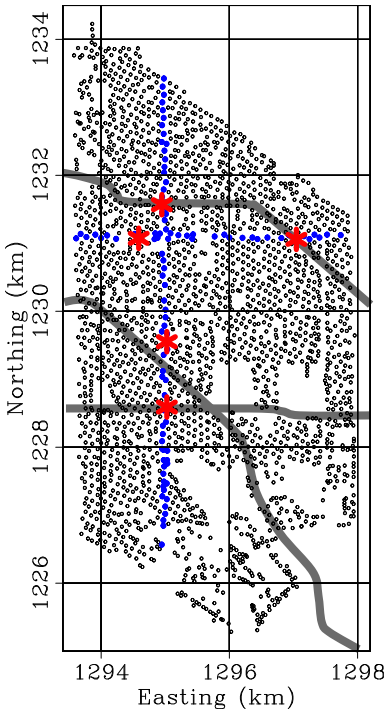

Figure 3.1: Map of the Long Beach seismic array. The red stars and blue lines correspond to virtual source locations and receivers, respectively, used for the virtual source gathers in this chapter. Major roads are outlined in grey. Interstate 405 is in the north, East 7th St runs east-west in the south, and Highway 1 runs northwest-southeast. Coordinates are NAD27, CA State Plane, Zone 7, kilometers. [**CR**] chap3/. lb-map-lines

Given the success of these studies at Long Beach, the goal here is to create high-frequency (greater than 3 Hz) group velocity maps using ambient seismic noise recordings. In the previous chapter, I showed that the ambient seismic noise field at Long Beach at these frequencies is dominated by traffic-induced Rayleigh waves, and particularly those generated by Interstate 405. As a result, I tailor the imaging procedure to account for these local sources. Using the traveltimes associated with the fundamental-mode Rayleigh waves, I produce group velocity maps of the shallow subsurface. I calculate group velocities rather than phase velocities because the former tend to show more variation with structure at depth (Widmer-Schnidrig and Laske, 2007), allowing shallow features to be more easily identified. I am able to resolve major geologic structures, including the north-south lithology dichotomy, the artificial fill associated with Alamitos Bay, and a linear feature in the Newport-Inglewood Fault zone.

While there are studies that have used traffic noise extracted from ambient seismic noise to image the subsurface (e.g., Nakata et al., 2011; Behm et al., 2014), the work in this chapter represents the first to utilize this particular energy to produce group velocity maps at both this spatial scale and this level of resolution. The results here showcase the potential of a cost-effective, non-invasive technique like passive seismic

interferometry to impact densely-populated urban environments where traditional active seismic surveys are challenging to operate. In addition to having lower costs and requiring less manpower, passive seismic techniques produce results that have important and practical implications for fields interested in the near surface. This includes earthquake hazard mapping, as low-velocity features tend to indicate regions susceptible to strong ground motion during earthquake-related shaking (Wills and Silva, 1998). With the development of pre-existing telecom infrastructure for continuous fiber-optic urban seismic acquisition (Martin et al., 2018), the techniques in this chapter have the potential to map hazardous regions in cities across the world at an even lower cost than a traditional passive seismic geophone array.

PASSIVE SEISMIC INTERFEROMETRY

Passive seismic interferometry effectively translates to cross-correlating ambient seismic noise recorded by a pair of receivers to obtain a reliable estimate of the Green's function between them (Lobkis and Weaver, 2001; Wapenaar, 2004; Snieder, 2004). To perform this technique at Long Beach, I apply an ambient-noise processing procedure similar to the one outlined in Bensen et al. (2007). For the preprocessing steps, I divide 32 days of continuous recordings from each station into non-overlapping two-hour time windows. Although it is unlikely I need that much data to synthesize Green's functions from traffic noise (Behm et al., 2014), I processed as much data as could be stored.

I then apply a spectral whitening procedure to each segment prior to cross-correlation. This step is advantageous in this particular seismic survey for a couple of reasons. One reason is that it compensates for expected variations in source amplitude due to varying traffic conditions over time, instrument spikes, and earthquakes. Another reason is that it maintains the phase information of the signal while increasing its bandwidth. By normalizing the complex signal spectrum by a smoothed version of the real-valued amplitude spectrum, the phase information of the signal is unaffected. The bandwidth of the signal is increased at the cost of losing the true correlation amplitude information, as any imbalances in the amplitude spectra (for instance, due to monochromatic noise sources or differences in receiver sensitivity) are compensated for by dividing by a smoothed version of the amplitude spectrum. This spectral amplitude imbalance is particularly significant in this dataset, as this

approach limits bias in frequency content introduced by the 3-Hz low-cut filter that had been applied to the data.

I then average the correlations associated with each individual receiver pair to obtain the final estimated Green's function (EGF). Overall, this process can be referred to as calculating the averaged whitened coherency (Weemstra et al., 2014). In the frequency domain, this procedure is expressed as:

$$[G(x_B, x_A, \omega) + G^*(x_B, x_A, \omega)] \approx \left\langle \left(\frac{U(x_B, \omega)}{\{|U(x_B, \omega)|\}} \right) \left(\frac{U^*(x_A, \omega)}{\{|U(x_A, \omega)|\}} \right) \right\rangle, \qquad (3.1)$$

where G is the Green's function between two receiver locations (x_A, x_B), $U(x, \omega)$ is the spectrum of the wavefield at a given receiver location x, $*$ represents the complex conjugate, $|\cdot|$ represents the magnitude of the spectrum, $\langle\cdot\rangle$ represents the time-averaged ensemble, and $\{\cdot\}$ represents a 0.003 Hz running window average used for normalizing the spectrum.

The result of this procedure (after an inverse Fourier transform into the time domain) can be interpreted as an estimate of the wavefield that would be recorded at receiver B if there was an impulsive source at receiver A. Because this signal is obtained through a correlation-based procedure, there are positive and negative time lags in the output. Positive time lags correspond to wavefields propagating away from the virtual source (like a virtual source gather), while negative time lags correspond to wavefields propagating toward the virtual source (like a receiver gather). If noise sources are well distributed, the correlation result is symmetric with respect to zero time lag. If noise sources cover only one of the Fresnel zones, the correlation result is asymmetric but still reliable (Stehly et al., 2006; Garnier and Papanicolaou, 2009). Given the number of stations and the number of two-hour time windows, I used this procedure to estimate over 2 billion Green's functions (i.e., 32 days $\times$ 12 time windows $\times$ 2400^2 receiver pairs).

By cross-correlating the recording from one receiver with recordings from all other receivers, I can create a virtual source gather centered at the one receiver. In practice, these virtual source gathers are dominated by surface waves in both the microseism band (Appendix B) and at high frequencies because noise sources are often located on the surface and because surface-wave amplitudes decay less rapidly than body-wave amplitudes. However, it is possible to extract body waves through various processing

approaches (see Appendix A for body wave analysis at Long Beach). Because I am focusing on traffic noise, each subsequent virtual source gather in this section is frequency bandpassed between $3 - 5$ Hz (based on the analysis is the previous chapter).

Virtual source gathers in map view

One major advantage of working with a dense passive seismic array is that the wavefronts in the virtual source gathers can be observed in map view. When the virtual source is in the southwest region of the array (1295.0 km easting, 1228.6 km northing) (Figure 3.2), there are hints of a circular wavefront propagating at both negative (Figures 3.2a-b) and positive time lags (Figures 3.2d-e). From the high-frequency beamforming results in the previous chapter, it appeared that there were Rayleigh waves propagating in all directions when far from Interstate 405. Taking this into account, and given the relatively slow moveout of the wavefront here, the observed seismic energy is likely Rayleigh waves generated by well-distributed traffic noise from local roads.

When the virtual source is centered on Interstate 405 (1294.9 km easting, 1231.6 km northing) (Figure 3.3), it is clear that the circular wavefront is strongest at positive time lags (Figures 3.3d-e). The pattern suggests that seismic energy is propagating primarily away from the virtual source location (the highway). This makes sense when taking into account the beamforming results, which suggested that the highway is the primary source of seismic energy when near the highway. Therefore, this wavefront is likely related to Rayleigh waves originating from Interstate 405.

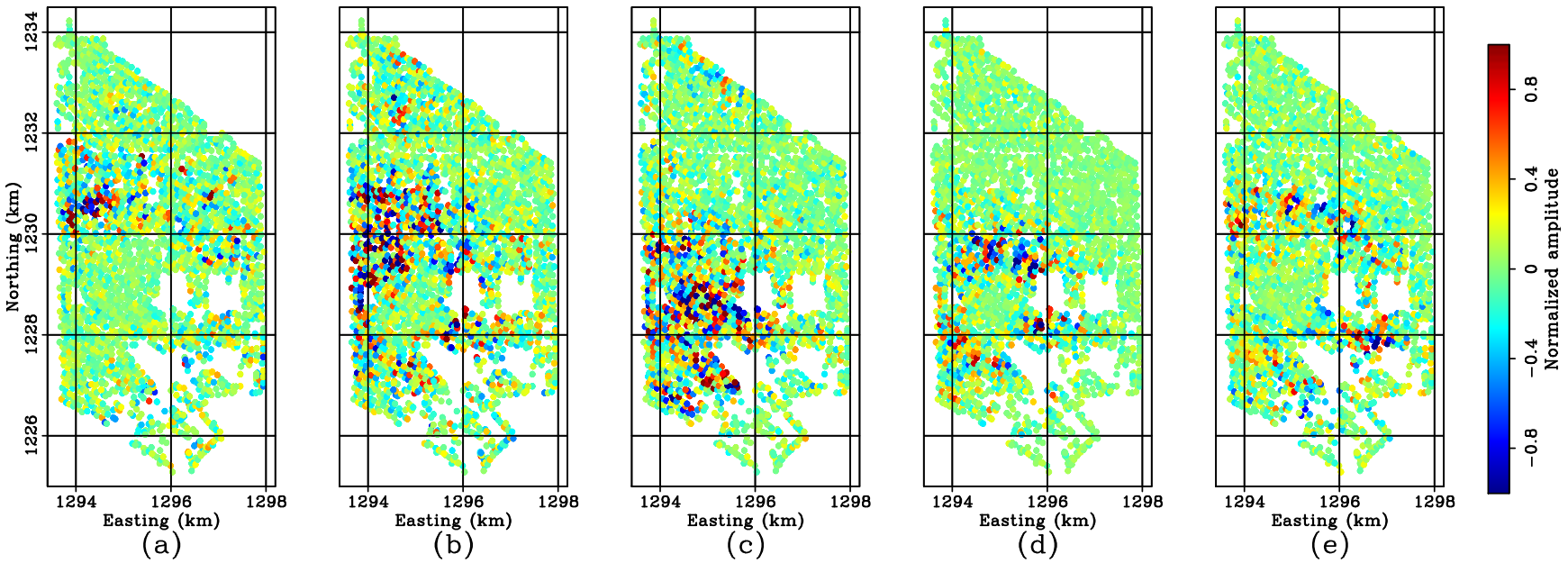

Figure 3.2: Snapshots of virtual source gathers centered in the southwest region of the array (1295.0 km easting, 1228.6 km northing) at (a) -8 s, (b) -4 s, (c) 0 s, (d) 4 s, and (e) 8 s. Snapshots are bandpassed for frequencies between $3-5$ Hz. All panels are clipped identically. Though messy, there are apparent Rayleigh waves propagating at both negative and positive time lags. [**CR**] chap3/. lb-01-si-low

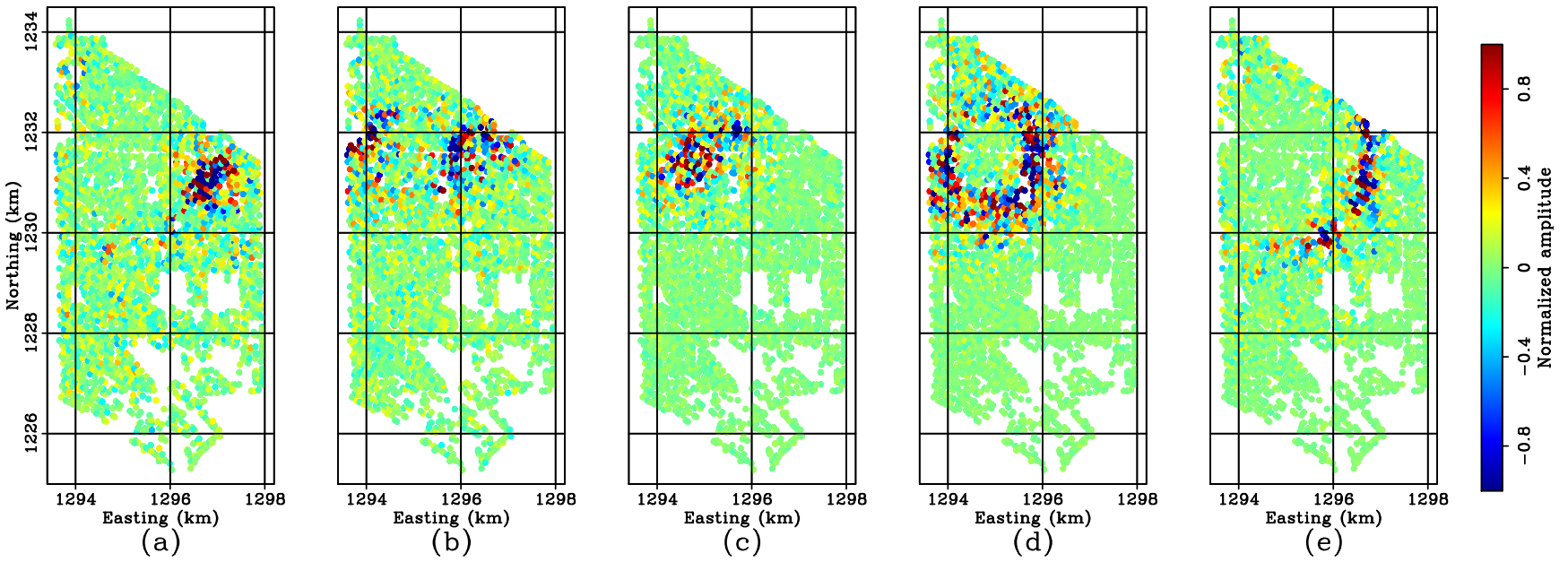

Figure 3.3: Snapshots of virtual source gathers centered over Interstate 405 (1294.9 km easting, 1231.6 km northing) at (a) -8 s, (b) -4 s, (c) 0 s, (d) 4 s, and (e) 8 s. Snapshots are bandpassed for frequencies between $3-5$ Hz. All panels are clipped identically. Note that most of coherent energy appears to be Rayleigh waves propagating, particularly at positive time lags. [**CR**] chap3/. lb-03-si-low

Virtual source gathers along receiver lines

To better understand how virtual source gathers are affected by receiver orientation relative to traffic noise sources, I focus on receiver lines oriented north-south and east-west in Figures 3.4 and 3.5, respectively (map in Figure 3.1). The EGFs in all panels are sorted by offset from the virtual source. I shift the offset limits in each panel so that the receiver locations do not visually shift from panel to panel. This allows the influence of major roads to be more easily observed.

Figure 3.4 shows three virtual-source gathers along a receiver line running perpendicular to Interstate 405. I examine this line orientation first because it ensures that the strongest noise source (Interstate 405) is in one of the Fresnel zones. The virtual sources are located on Interstate 405 (Figure 3.4a), on E 7th St (Figure 3.4c), and between the two roads (Figure 3.4b). Although there is a noticeable amount of noise, there are clear fundamental-mode Rayleigh waves in the EGFs traveling at approximately 250 m/s in all panels. There are also hints of a first-order mode Rayleigh wave traveling at approximately 450 m/s at positive time lags and positive offsets in Figure 3.4c.

Two observations indicate that the Rayleigh waves being extracted at these frequencies are generated by traffic noise. The first indication is that virtual-source gathers centered on roads and highways (Figures 3.4a and 3.4c) show Rayleigh waves at mostly positive time lags at near offsets. This indicates that energy is primarily radiating away from the virtual source locations (in these cases, roads and highways) and not towards it. The second indication is the presence of sharp peaks in the gather when the virtual source is between E 7th St and the highway (Figure 3.4b). These peaks are indicative of nearby active sources, and their offsets from the virtual source location consistently correspond to the locations of the highway and local road. Note that signal from E 7th St likely appears strong because the receiver line passes through a golf course, which is a relatively quiet area of the array.

I observe similar characteristics in the virtual source gathers along a line oriented parallel (east-west) to Interstate 405 (Figure 3.5). When the virtual source is centered on the highway, energy is mostly found at positive time lags, as expected (Figure 3.5b). When the virtual source is not on the highway, there are still fundamental-mode Rayleigh waves with reasonable moveout velocities (Figure 3.5a).

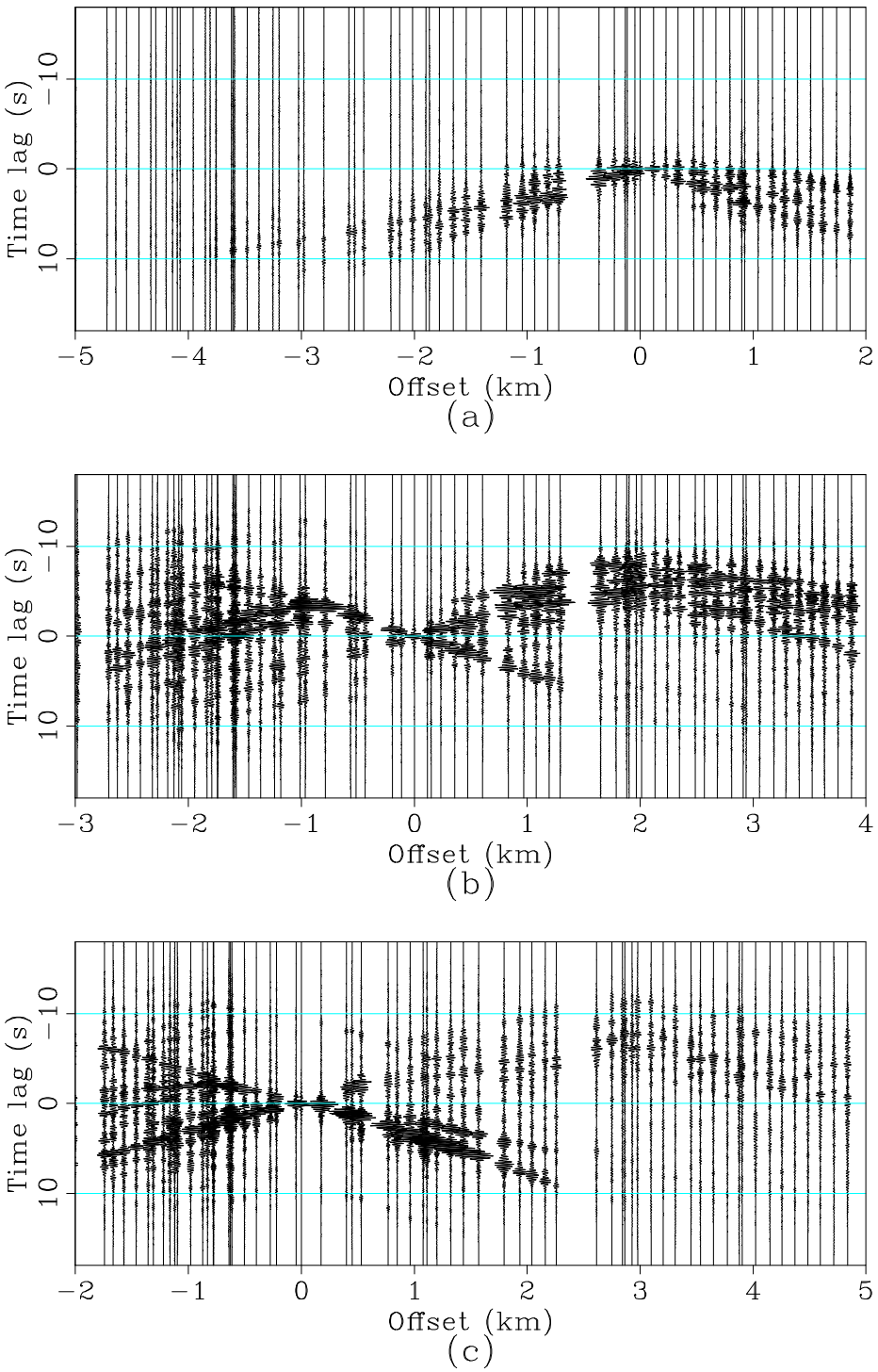

Figure 3.4: Virtual source gathers along a line of receivers oriented north-south (Figure 3.1). Virtual sources are located (a) at Interstate 405, (b) between Interstate 405 and E 7th St, and (c) at E 7th St. Positive offsets correspond to waves propagating toward the north, while negative offsets correspond to waves propagating toward the south. Each panel has been bandpassed for frequencies between $3 - 5$ Hz and is clipped independently. [**CR**] chap3/. nslines

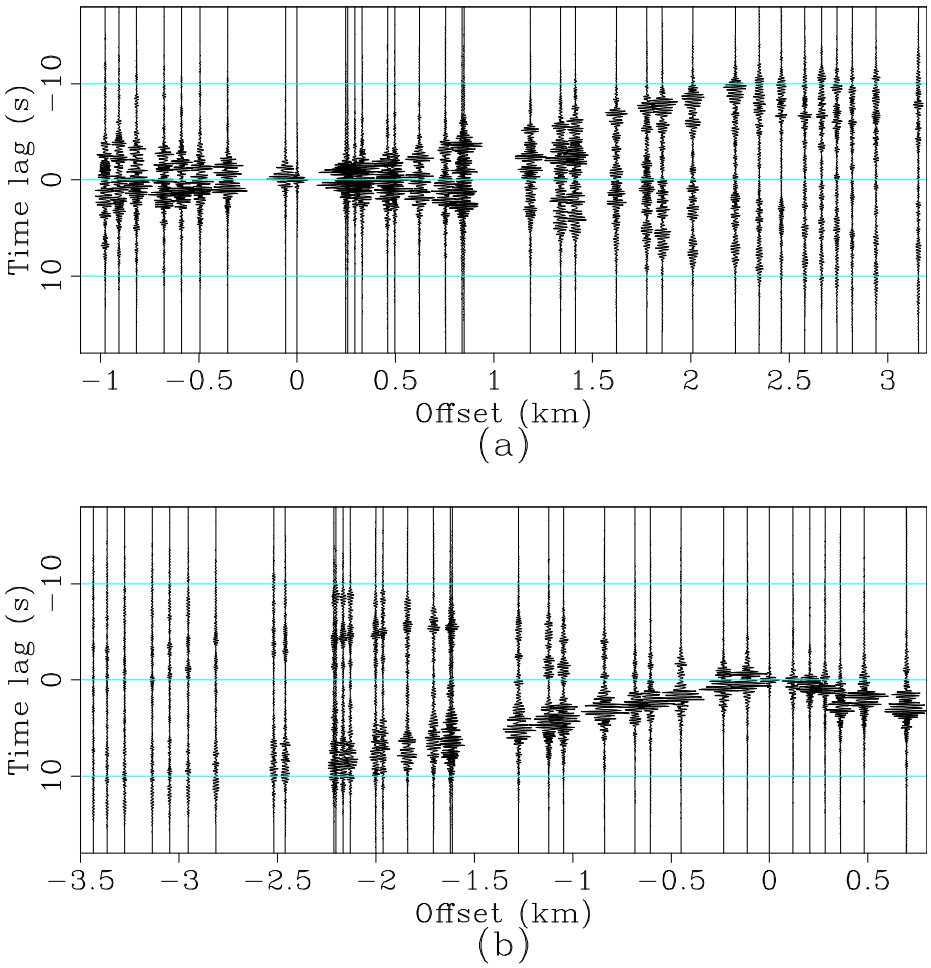

Figure 3.5: Virtual source gathers along a line of receivers oriented east-west (Figure 3.1). Virtual sources are (a) west and (b) east. Positive offsets correspond to waves propagating toward the east, while negative offsets correspond to waves propagating toward the west. Each panel has been bandpassed for frequencies between $3 - 5$ Hz and is clipped independently. [**CR**] chap3/. ewlines

The virtual source gather in this particular case may be surprising since energy from the highway, which runs roughly parallel to this line of receivers, is primarily arriving perpendicular to the axis formed by the virtual source and receivers, making it the least ideal source distribution for estimating reliable Green's functions from ambient seismic noise. One possible reason I am still able to obtain reasonable Rayleigh waves is that the eastern portion of the highway and other strong local roads are still located inside the Fresnel zones. Furthermore, although the highway primarily runs parallel to the receiver line, it does not necessarily contribute significantly to the EGF. First, the highway does not act as a stationary point source. Vibrations emanating from the highway are generated by moving vehicles with different source signatures, and as a result the contribution of each vehicle to the EGF destructively interferes with itself as it moves parallel to the receiver line. Second, although the highway is seemingly the strongest source in the array, there is still energy generated from local roads that are not only in the Fresnel zones but also very close to the receiver(s). As a result, Rayleigh waves generated by ideally positioned local roads appear more energetic and thus contribute most to the EGF.

Altogether, I conclude that passive seismic interferometry applied at Long Beach can extract traffic-generated Rayleigh waves from not only Interstate 405, but also from local roads. Though the arrivals are noisy (compared to low-frequency EGFs in Appendix B), the associated traveltimes could be reliable enough to use in a tomography procedure.

GROUP VELOCITY TOMOGRAPHY

I focus on the fundamental-mode Rayleigh waves because they are the most easily identified and consistent wave modes in the virtual source gathers. Further work is needed to utilize the first-order mode Rayleigh waves, which can have a number of benefits when constraining near-surface seismic velocities, particularly when inverting surface-wave dispersion curves for 1D S-wave velocity depth profiles (Socco et al., 2010). They include allowing for deeper investigation depths, stabilizing the dispersion curve inversion process, and enhancing the resolution of the inverted velocity model. Here, I choose to investigate group velocities because they tend to show more variation with structure at depth than phase velocities (Widmer-Schnidrig and Laske, 2007).

Travel time selection

To pick fundamental-mode Rayleigh-wave group traveltimes, I apply frequency-time analysis (FTAN) (Levshin et al., 1972). I first calculate the envelope of the EGFs and apply narrow Gaussian bandpass filters centered at the frequencies of interest (here, 3.0 Hz and 3.5 Hz). I then average the positive and corresponding negative time lag signals in an effort to compensate for the inhomogeneous noise source distribution. Note that while this symmetrization of the EGF is commonly performed, it is not agreed upon that it is the best strategy (e.g., Witek et al., 2014).

Because there are two possible Rayleigh wave modes in the EGFs (Figure 3.4c), I calculate two linear moveout windows to guide traveltime picking: one based on the fundamental mode and one based on the first-order mode. I estimate moveout velocities by creating a virtual source gather centered on Interstate 405 (Figure 3.6a), sorting the traces by radial offset, and then transforming the result into the frequency-wavenumber domain. I chose this particular source location because the highway is the strongest source in the array and is thus expected to produce the most reliable virtual source gather.

Figure 3.6b shows two clear wave modes, although the first-order mode energy is relatively weak above 3 Hz. For the fundamental mode I estimate velocities of 300 m/s and 250 m/s at 3.0 Hz and 3.5 Hz, respectively, while for the first-order mode I estimate velocities of 550 m/s and 500 m/s, respectively. To account for potential deviations from the estimated velocities, all moveout windows are 2.5 s wide. I choose the peak of the envelope inside the fundamental-mode window as the group traveltime. Limiting traveltimes to inside this window helps to pick signals generated by noise sources in the Fresnel zones while avoiding strong, artificially early peaks that are attributed to local noise sources outside the Fresnel zones (Figure 3.7a), such as in between the virtual source and receiver. I then avoid all energy inside the first-order mode window in the signal-to-noise ratio (SNR) calculation, as the early peak of the first-order mode (relative to the later peak of the fundamental mode) should not be considered noise that would degrade the SNR (Figure 3.7b). Here, SNR is calculated as the ratio of the maximum amplitude of the envelope inside the fundamental-mode window to the root-mean-square of the envelope outside both the fundamental and first-order mode moveout windows.

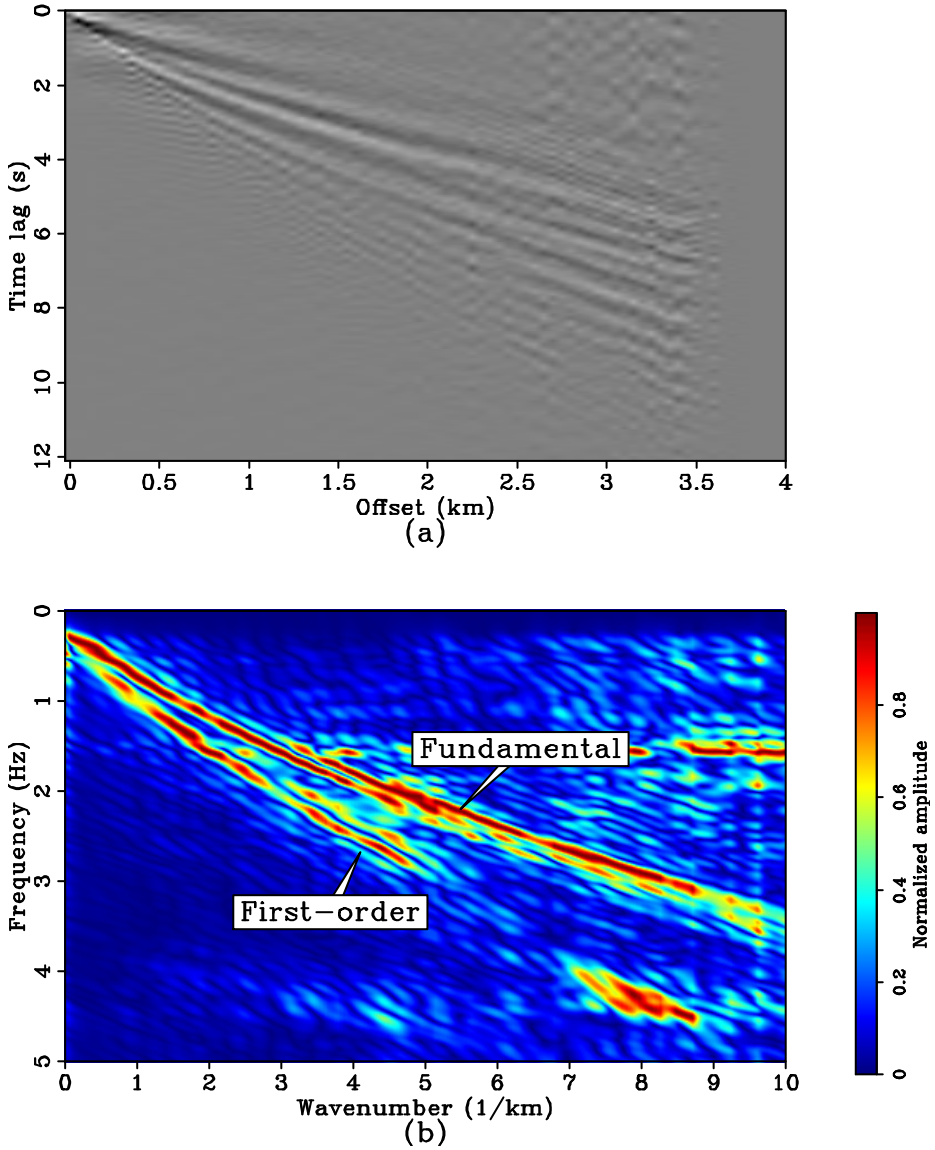

Figure 3.6: (a) Virtual source gather centered at Interstate 405 and (b) the resulting frequency-wavenumber plot. The two sloping events correspond to the fundamental- and first-order mode Rayleigh waves. [**CR**] chap3/. gather-fk

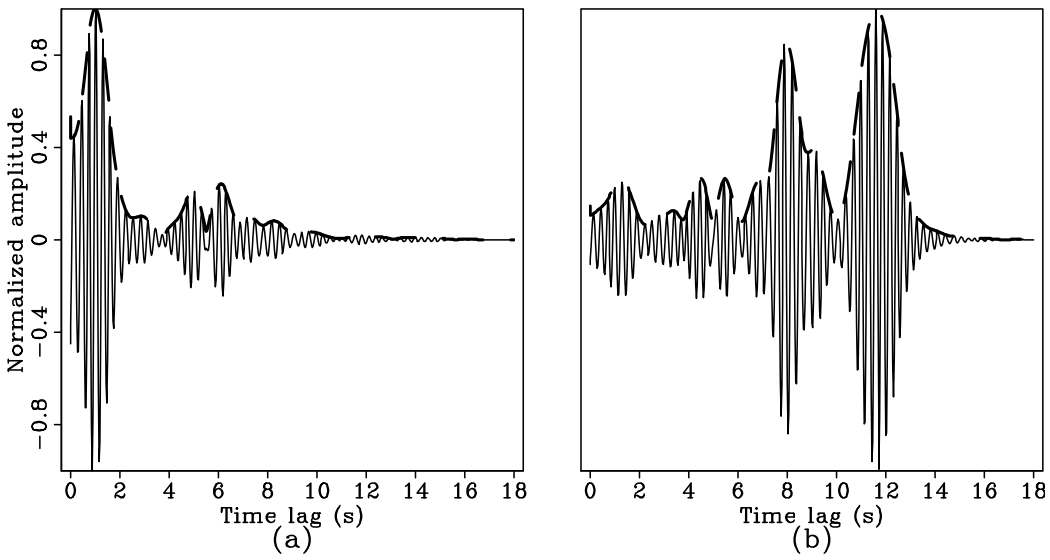

Figure 3.7: Examples of Rayleigh waves extracted from ambient noise processing. (a) Trace containing a strong, artificially early arrival associated with the fundamental-mode Rayleigh wave (at 1 s). The distance between the virtual source and receiver is over 2 km. This early arrival is attributed to the presence of the highway between the two locations. (b) Trace containing the first-order (at 6.5 s) and fundamental (at 9 s) mode Rayleigh wave arrivals. [**CR**] chap3/. lb-traces

For both examined frequencies, I kept correlations with SNR greater than 5. Figures 3.8 and 3.9 show traveltime maps associated with three virtual source locations at 3.0 Hz and 3.5 Hz, respectively. These plotted traveltimes correspond to fundamental-mode Rayleigh waves that have surpassed my SNR criterion. The influence of a localized noise source such as Intestate 405 on the correlations is clear when the virtual source is near the highway (left columns; Figures 3.8 and 3.9). When the receiver is on the same side of the highway as the virtual source, nearly all corresponding correlations meet the SNR criterion. When the receiver is on the opposite side of the highway, nearly all corresponding correlations fail to meet the SNR criterion. This trend is expected because when a strong source is located between a virtual source and receiver, there are artificially early peaks in the resulting correlations. These early peaks degrade the SNR and result in a lack of accepted traveltimes on the other side of the highway.

When the virtual source is near the center of the array (middle columns; Figures 3.8 and 3.9), the influence of the highway on the correlations significantly decreases. As supported by the beamforming analysis in the previous chapter, the ambient seismic noise field is instead driven by noise from local roads, which are more evenly distributed in space. Thus, the acceptable traveltimes are well-distributed azimuthally in this region. Due to the greater effect of attenuation at higher frequencies, the maximum offset between the virtual source and receivers with accepted traveltimes is greater at 3.0 Hz (Figure 3.8b) than at 3.5 Hz (Figure 3.9b).

When the virtual source is in Alamitos Bay (right columns; Figures 3.8 and 3.9), there are fewer acceptable traveltimes. This is likely explained by the lack of local roads in the area. Without traffic noise, there is relatively little Rayleigh-wave energy to be extracted from the ambient seismic noise field at these frequencies. As when the virtual source is in the center of the array, the maximum offset between the virtual source and receivers with accepted traveltimes is greater at 3.0 Hz (Figure 3.8c) than at 3.5 Hz (Figure 3.9c) due to signal attenuation. Altogether, these traveltime maps suggest that the fundamental-mode Rayleigh-wave traveltime selection procedure is reliable.

For the tomography procedure, I only use traveltimes from virtual sources and receivers with offset between $0.5 - 1.7$ km at 3.0 Hz and between $0.4 - 1.5$ km at 3.5 Hz. The minimum offset is approximately four wavelengths and is longer than the suggested three wavelengths (Bensen et al., 2007; Moschetti et al., 2007) because I wanted to avoid traces where the fundamental and first-order modes arrive at similar times. In these types of traces, a reliable fundamental-mode traveltime is difficult to measure. I enforce maximum offsets in an attempt to limit potential artifacts in the tomography results caused by ray-bending. The maximum acceptable offset is shorter at higher frequencies because of attenuation effects. After applying these picking criteria to $2,980,143$ correlations, we are left with $530,876$ traveltimes (18%) at 3.0 Hz and $403,523$ traveltimes (13%) at 3.5 Hz.

Straight-ray tomography

To obtain group velocity maps, I employ a straight-ray tomography procedure with regularization (Sabra et al., 2005b; Aster et al., 2013). The choice of using straight

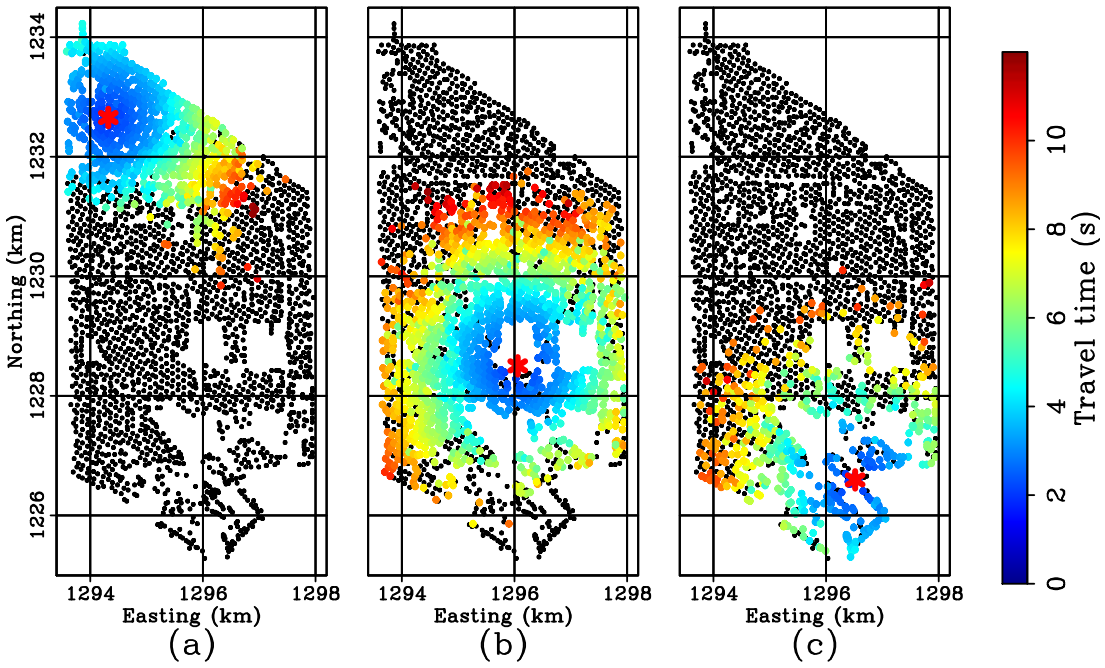

Figure 3.8: Travel time maps for the 3.0-Hz fundamental-mode Rayleigh waves generated at three virtual source locations (indicated by red stars). Only travel-times associated with correlations with SNR greater than 5 are displayed. [**CR**] chap3/. tt-3p00hz-maps

rays is consistent with the inability of group traveltimes to be computed using bending rays in a group velocity map. The tomography problem is solved in terms of slowness perturbation, $\Delta\mathbf{m}$, with respect to an average constant slowness value, m_o, calculated from the measured traveltimes and distances between all input virtual sources and receivers. The final slowness model, $\mathbf{m}$, is given by $\mathbf{m} = \mathrm{m}_o + \Delta\mathbf{m}$. I subtract the contribution of the average slowness from each measured traveltime to obtain the measured residual traveltimes, $\Delta\mathbf{t}$, needed for the inversion.

I model residual traveltimes by applying a straight-ray tomography operator, $\mathbf{F}$, to a slowness perturbation model. Rows of the operator contain information about the length of a straight ray through each model grid cell for a single virtual source-receiver path. The final slowness model domain is composed of a 110×200 regular grid with 50 m $\times$ 50 m cells. I use a conjugate gradient approach to minimize the objective function:

$$J(\Delta\mathbf{m}, \epsilon) = ||\mathbf{W}\,(\mathbf{F}\Delta\mathbf{m} - \Delta\mathbf{t})\,||_2^2 + \epsilon||\nabla^2\Delta\mathbf{m}||_2^2, \tag{3.2}$$

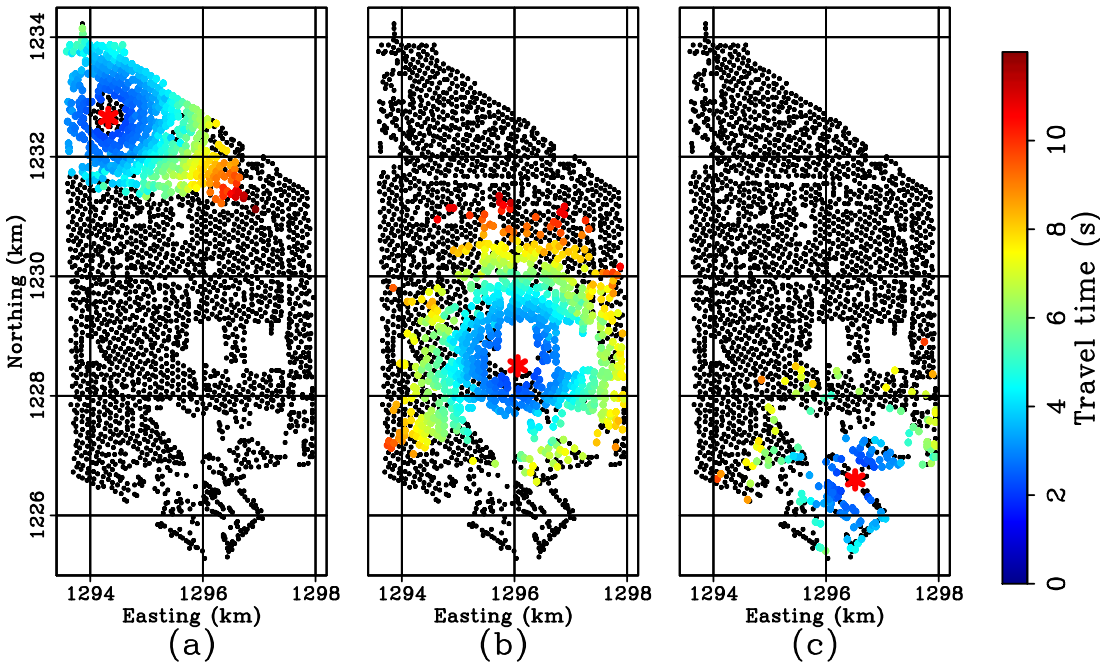

Figure 3.9: Travel time maps for the 3.5-Hz fundamental-mode Rayleigh waves generated at three virtual source locations (indicated by red stars). Only travel-times associated with correlations with SNR greater than 5 are displayed. [**CR**] chap3/. tt-3p50hz-maps

where Laplacian ∇^2 is the roughening operator used for model-smoothing, ϵ is the regularization strength that balances the data-fitting objective and the model-smoothing objective, and $\mathbf{W}$ represents a diagonal weighting matrix. I use the approach of weighted least squares because there is variability in traveltime measurement errors from one virtual source-receiver pair to another.

Values along the diagonal of the weighting matrix are based on the standard deviation of daily traveltimes for each virtual source-receiver pair (32 picks for 32 days of data). Typically, these values are taken to be the inverse of these standard deviations. In this case, the standard deviations are a reflection of precision but not necessarily accuracy. For instance, if there is an active source (e.g., Interstate 405) between a virtual source and receiver, the traveltime picks may be precise over a span of time but their arrival times are artificially early. Because some precise picks may not be accurate, I do not want to weight precise picks significantly higher than less-precise picks. Additionally, the upper bound of standard deviations appears to increase with distance between the virtual source and receiver (Figure 3.10), regardless

of the frequency examined. This results in traveltimes associated with shorter offsets generally being weighted higher than those associated with longer offsets.

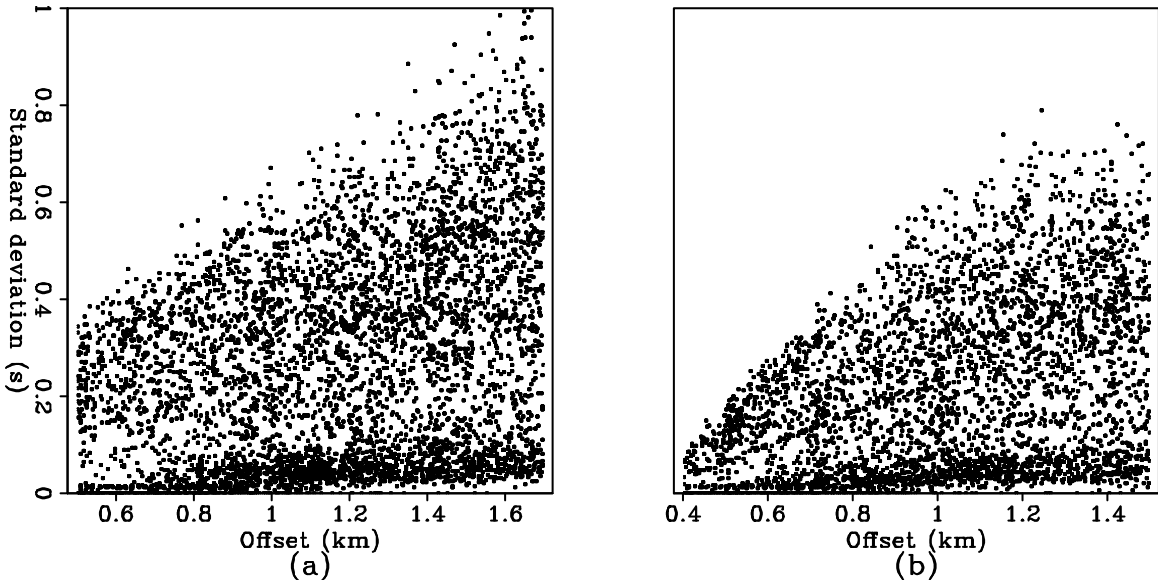

Figure 3.10: Distribution of standard deviations with virtual source-receiver offset. Results are for picks at (a) 3.0 Hz and (b) 3.5 Hz. 0.1 % of the total traveltime picks are shown for both frequencies. [**CR**] chap3/. stdevs

Given these biases in the standard deviation calculations, I choose to limit their effect on the spread of weights. Thus, I calculate the weight for the ith traveltime pick, w_i, with the following original functional (rather than the inverse of the standard deviation):

$$w_i = \frac{1 + \mathrm{e}^{-\sigma_i/k}}{2}, \tag{3.3}$$

where σ_i is the standard deviation for the ith traveltime pick and k is a parameter set to determine the spread of weights. I choose k such that most station pairs are closely weighted (close to 1) while station pairs with high standard deviations are down-weighted toward 0.5. For these traveltime picks, I set $k = 0.5$ through manual tuning. The resulting weights as a function of offset are shown in Figure 3.11. By limiting the overall spread of weights, I down-weight noisy picks without overly up-weighting precise but inaccurate picks.

To select a regularization strength, and hence a final slowness model, I perform an L-curve analysis. This approach involves the construction of a trade-off curve between the weighted data misfit, $||\mathbf{W}\left(\mathbf{F}\Delta\mathbf{m} - \Delta\mathbf{t}\right)||_2^2$, and the smoothed model semi-norm, $||\nabla^2\Delta\mathbf{m}||_2^2$, in Equation 3.2 above (Aster et al., 2013). Inversions using different

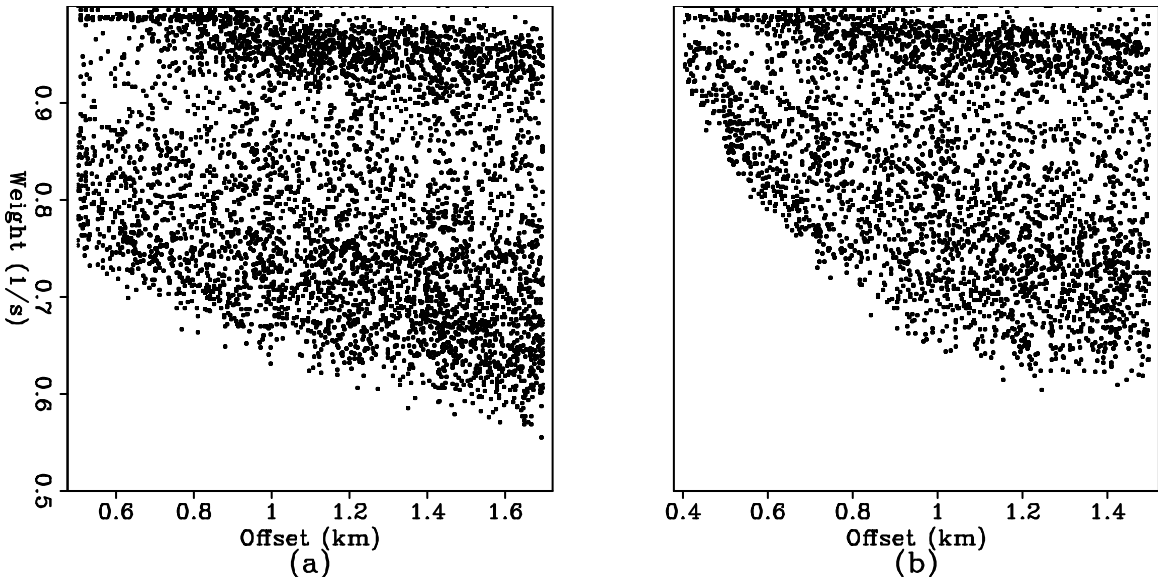

Figure 3.11: Distribution of weights with virtual source-receiver offset using the functional in Equation 3.3. Results are for picks at (a) 3.0 Hz and (b) 3.5 Hz. 0.1 % of the total traveltime picks are shown for both frequencies. [**CR**] chap3/. weights

regularization strengths, ϵ, plot to different points along this curve, as lower values of ϵ reduce the data misfit while increasing the model roughness, and higher values of ϵ increase the data misfit while decreasing the model roughness. The resulting curve typically resembles the shape of an "L", and the value that produces a solution closest to the corner of this curve is selected as the regularization strength, as it balances the two fitting goals best.

For this study, I examine regularization strengths from 0 to 5 in increments of 0.25. The resulting trade-off curves (after taking the logarithm of the model semi-norm and weighted data residual norm) at 3.0 Hz and 3.5 Hz leads me to choose a regularization strength of 1.50 for both frequencies (Figure 3.12). For each inversion, I ran 25 iterations, which was enough to converge to a solution (Figure 3.13). Note that this inversion problem is under-determined, as there are insufficient data to constrain velocity in certain regions.

Near-surface group velocity maps

The group velocity maps derived from fundamental-mode Rayleigh waves at 3.0 Hz and 3.5 Hz are shown in Figures 3.14b and 3.14c, respectively. Due to the dispersive

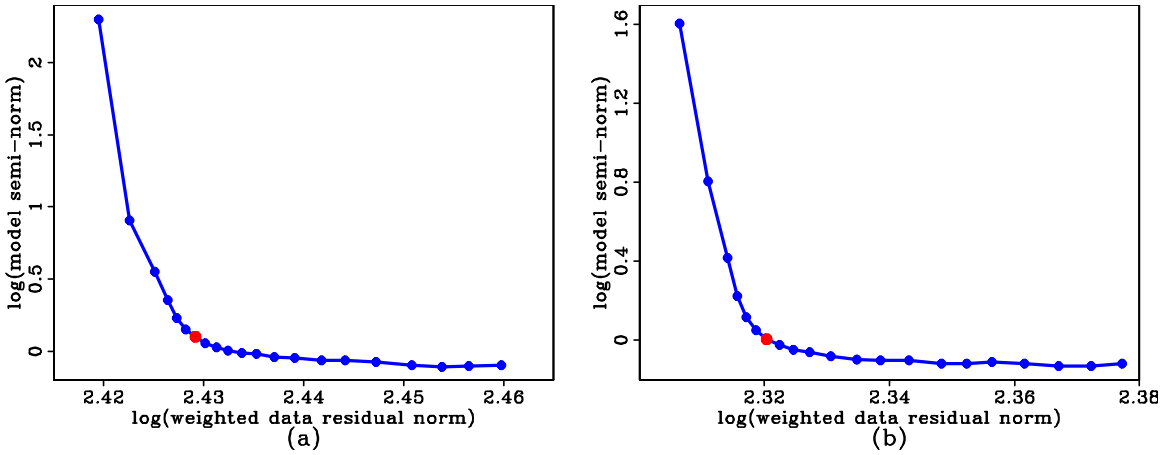

Figure 3.12: Trade-off curves between the logarithm of the norm of the weighted data residual and the logarithm of the semi-norm of the resulting model given different regularization strengths for tomographic inversion at (a) 3.0 Hz and (b) 3.5 Hz. Smaller points represent regularization strengths, ϵ, from 0 (top left) to 5 (bottom right) in increments of 0.25. The red point corresponds to a regularization strength of 1.50, which is the value used in the tomographic inversion. [**CR**] chap3/. lcurve

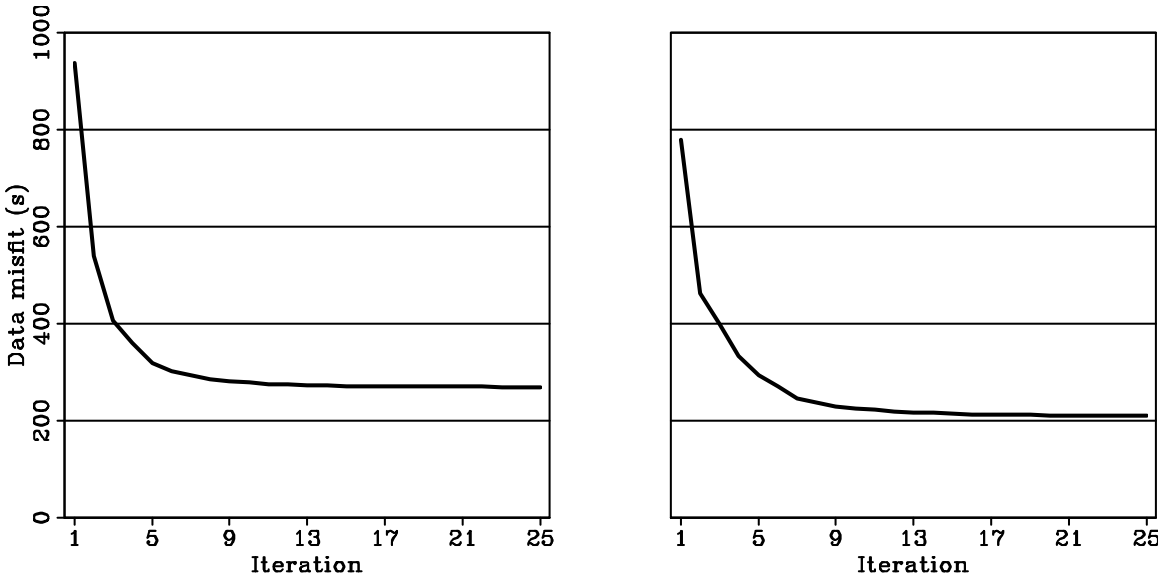

Figure 3.13: L2 norm of the data misfit as a function of iteration from inversion of traveltimes at (a) 3.0 Hz and (b) 3.5 Hz, with regularization strength of 1.50. [**CR**] chap3/. convergence

nature of Rayleigh waves, the velocities at lower frequency are generally higher than the velocities at higher frequency. Both velocity maps display similar trends, likely because the average wavelengths at these frequencies are similar (approximately 85 m at 3.0 Hz and 70 m at 3.5 Hz). Assuming Rayleigh waves are sensitive to a depth approximately one-third of the wavelength (Forsyth et al., 1998), the velocity maps at 3.0 Hz and 3.5 Hz correspond to depths of approximately 28 m and 23 m, respectively. To interpret these trends, I compare the results to a geologic map of the survey area in Figure 3.14a (California Department of Conservation, 2012).

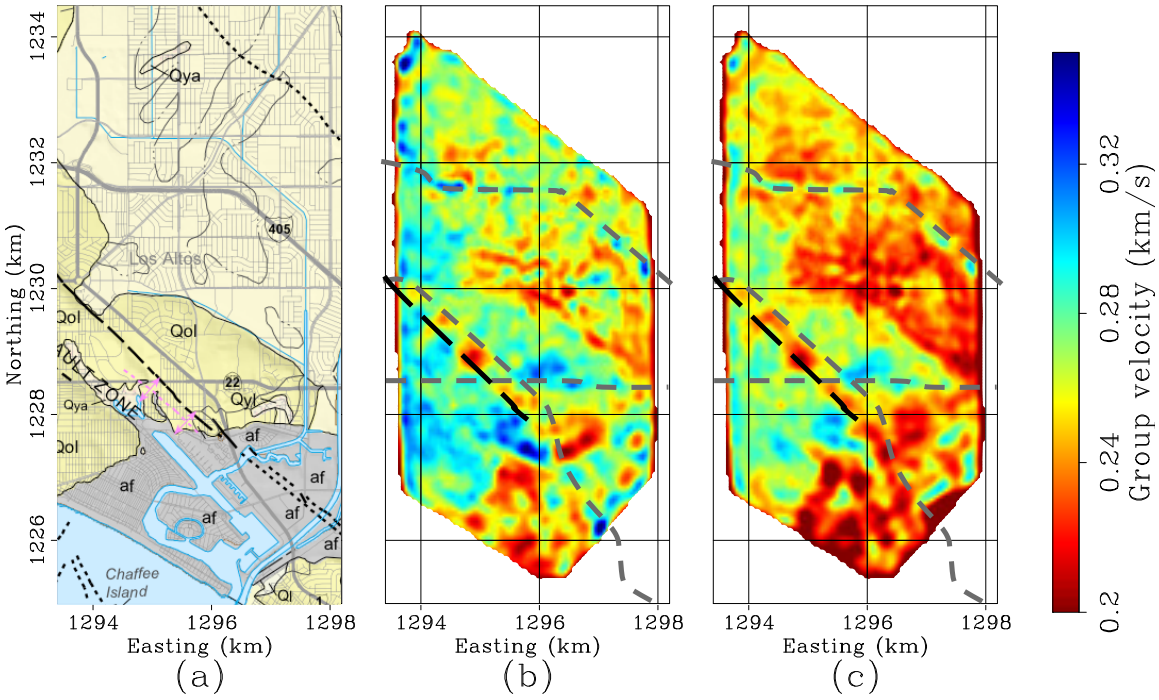

Figure 3.14: (a) Geologic map of the survey area (California Department of Conservation, 2012). Light yellow indicates Holocene to late Pleistocene alluvial fan deposits, dark yellow indicates late to middle Pleistocene lacustrine, playa, and estuarine deposits, and grey indicates artificial fill. Group velocity maps generated at (b) 3.0 Hz and (c) 3.5 Hz. Grey lines in the maps correspond to major roads. The north line is Interstate 405, the east-west line to the south is E 7th St, and the northwest-southeast diagonal line is Highway 1. The black line in the west represents the location of the Newport-Inglewood Fault. [**CR**] chap3/. lb-tomo

DISCUSSION

The most prominent trend in the group velocity maps is a boundary running northwest-southeast across the array that separates a lower velocity region (north) from a higher

velocity region (south); it is most distinct south of the eastern section of Interstate 405 at 3.5 Hz (Figure 3.14c). This boundary coincides well with a boundary in the geologic map that separates Holocene to late Pleistocene alluvial fan deposits (north; light yellow) from late to middle Pleistocene lacustrine, playa, and estuarine deposits (south; dark yellow). The deposits in the north are unconsolidated to slightly consolidated material, while the deposits in the south are slightly to moderately consolidated material. The nature of these deposited materials support the lower velocities in the north and the higher velocities in the south that are observed.

Another prominent feature in both group velocity maps is a low-velocity zone in the southeast region of the array. This zone corresponds to Alamitos Bay, and the geologic map indicates that it was built on artificial fill, which is expected to display relatively low velocities (Wills and Silva, 1998). Overall, the significant trends in the group velocity maps match the surface geology at Long Beach well.

Two smaller but notable features in the velocity maps are the low-velocity linear trend in the western portion of the Newport-Inglewood Fault zone and the high velocities overlaying Interstate 405 in the north. One possible explanation for the low-velocity trend is that it is the fault itself, as the location of the anomaly coincides well with the surface projection of the fault in the geologic map (black dashed line). A relatively low-velocity fault signature at shallow depths (approximately 25 m) would be different from the relatively high-velocity fault signature at deeper depths (approximately 100 m) observed by Dahlke et al. (2014), Nakata et al. (2015), and Lin et al. (2013). The last study hypothesized that the high-velocity signature was related to deeper material being pushed up during the fault deformation process. Here, the low-velocity signature could represent the fault damage zone. Material in this zone becomes fractured during slip and is thus likely to display a relatively low seismic velocity (Mooney and Ginzburg, 1986).

Another possible explanation for the low-velocity linear trend is that it is related to the narrow region of less-consolidated material seen in the geologic map (light yellow, extending from grey; Figure 3.14a). Although the features are spatially offset from each other, the geologic map is representative of the surface while the tomography results are sensitive to features tens of meters below the surface. Thus, I could be sensing a dipping, low-velocity geologic structure, which may or may not be related to the presence of a fault.

There is also the possibility that this low-velocity trend is related to Highway 1. Though they do not overlap perfectly with each other, they both follow similar trajectories in the west and bend toward the south in the southeast region of the array (most noticeably in the velocity map at 3.5 Hz). However, resolution is expected to be poor in the southeast region of the array given that there are fewer receivers and less traffic in the area, leading to poor ray coverage. Therefore, one cannot fully believe such narrow features in this area, let alone confidently associate it with the path of Highway 1. More importantly, Highway 1 is more likely to produce a high-velocity signature than a low-velocity one based on the following analysis of the high-velocity trend overlaying Interstate 405.

The previously mentioned high-velocity trend is likely an artifact explained by the combination of the temporal width of the picking window for the fundamental mode and the highway acting as an active noise source. As seen in the virtual-source gathers (Figures 3.4 and 3.5), when the virtual source and receiver are on opposite sides of the highway, I measure an artificially early traveltime. For a receiver just a few hundred meters on the other side of the highway from the virtual source, the traveltime is still artificially early, but not early enough to arrive outside of the fundamental-mode picking window. Thus, the picking procedure accepts slightly early traveltimes associated with receivers near the highway (as seen in Figures 3.8a and 3.9a), which results in an artificial high-velocity trend aligned with the highway.

While there are other busy roads (e.g., E 7th St and Highway 1; Figure 3.1), they do not appear as high-velocity trends because the signal they generate is not as strong relative to its surroundings as the signal from Interstate 405 (as seen in the previous chapter). As a result, these roads do not act as overwhelmingly strong active noise sources like Interstate 405, which makes them less susceptible to these picking artifacts.

Resolution analysis of tomographic results

To assess the spatial resolution of the group velocity maps, I take two approaches. First, I plot the number of rays passing through each model grid cell for all ray paths associated with correlations used in the tomography procedure. Figure 3.15 shows the ray count for 3.5 Hz correlations; the map for 3.0 Hz correlations is similar. More

straight rays passing through a cell suggests better resolution.

As expected, the ray count is highest in the center of the map due to the array geometry and the presence of a strong noise source (Interstate 405) in that region. The low-count areas correspond to gaps in the receiver distribution. This lack of coverage is particularly evident in the southeast region of the array, where the effect of the lack of receivers is compounded by the relative lack of traffic noise due to the presence of the marina. Therefore, I expect higher resolution in the center of the array and lower resolution along the edges of the array, particularly in the marina.

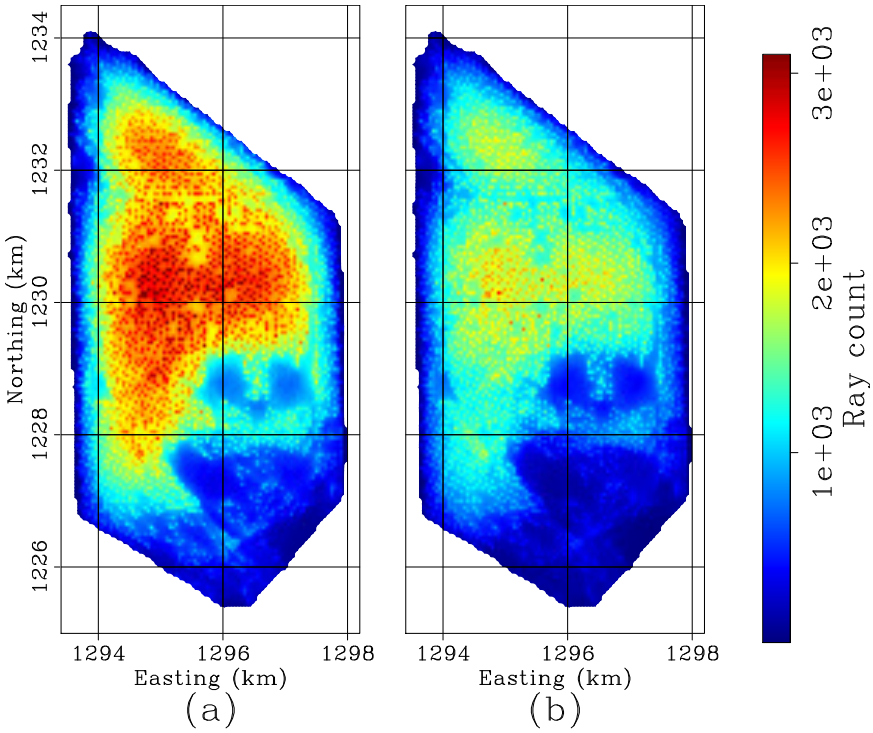

Figure 3.15: Number of rays passing though each grid cell for all correlations used at (a) 3.0 Hz and (b) 3.5 Hz. [**CR**] chap3/. raylengths

To qualitatively assess how poor the spatial resolution is along the edges of the array, I perform checkerboard tests. I add a sinusoidal, or checkerboard, velocity perturbation to the final inverted velocity model. Maximum perturbations are set to 15% of the modeled velocity, which is smaller than the minimum percent difference between the major low- and high-velocity regions. I examine checkers that are 500 m $\times$ 500 m (Figure 3.16a) and 200 m $\times$ 200 m (Figure 3.17a). I generate synthetic traveltimes through the perturbed model and add random Gaussian noise with a mean of 0 and a standard deviation based on the distribution of traveltime picks

from daily correlation stacks (32 picks for 32 days of data). In this procedure, each virtual source-receiver pair has its own standard deviation. I then invert the noisy traveltimes using the same parameters as in the inversion of the actual data. I use ray coverages associated with both 3.0 Hz and 3.5 Hz inversions.

For large checker sizes (Figure 3.16), the overall checkerboard pattern is reasonably well resolved throughout the entire array, even along most of the edges of the model. The exception is the southeast region of the array. Traffic noise is inconsistent and weak in that area, which can lead to relatively low SNR in the correlations and large error in the traveltime picks. Combined with the sparse ray coverage, it is no surprise that these checkers cannot be well resolved in that region. Note that the recovered checkerboards are similar for both ray coverage distributions.

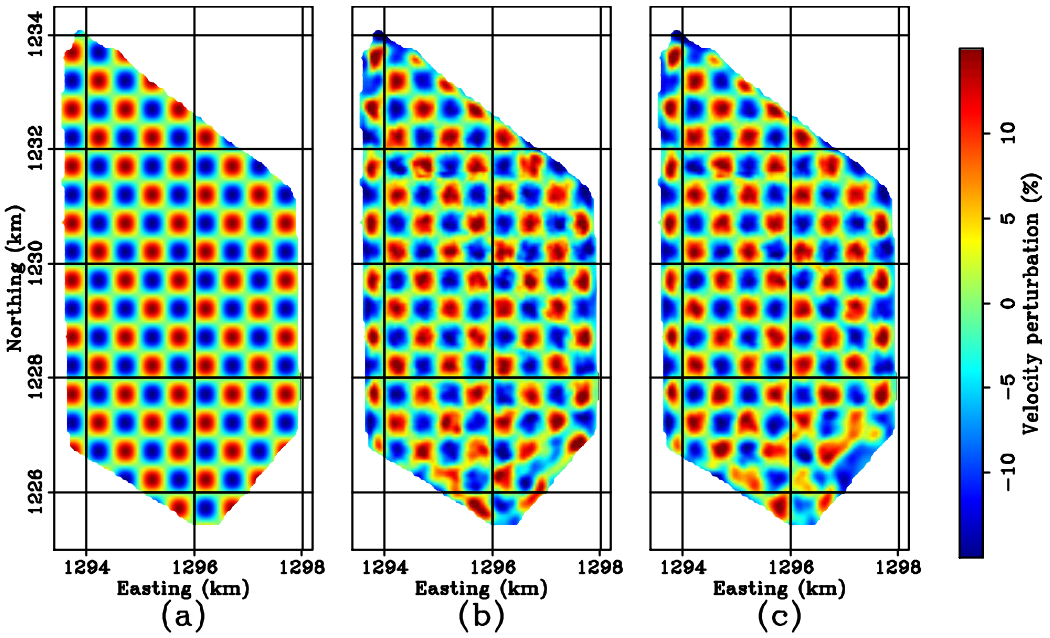

Figure 3.16: Checkerboard tests with checkers spanning 500 m × 500 m squares. (a) True model. (b) Recovered checkerboard using ray coverage associated with inversion at 3.0 Hz. (c) Recovered checkerboard using ray coverage associated with inversion at 3.5 Hz. [**CR**] chap3/. checker500

For small checker sizes (Figure 3.16), the overall checkerboard pattern is reasonably well resolved in the center of the array but not particularly along the edges of the array. Again, resolution is especially poor in the southeast region of the array, likely because of the reasons previously outlined. Additionally, some checkers in the

northeast region of the array are only well resolved in the southwest-northeast direction. This is likely due to the directionality of the majority of accepted ray paths at these frequencies, which run perpendicular to the highway. Given the accepted ray paths and the noise model, these results suggest that there is at least 200 m × 200 m resolution in the center of the array and at least 500 m × 500 m resolution along the fringes of the array.

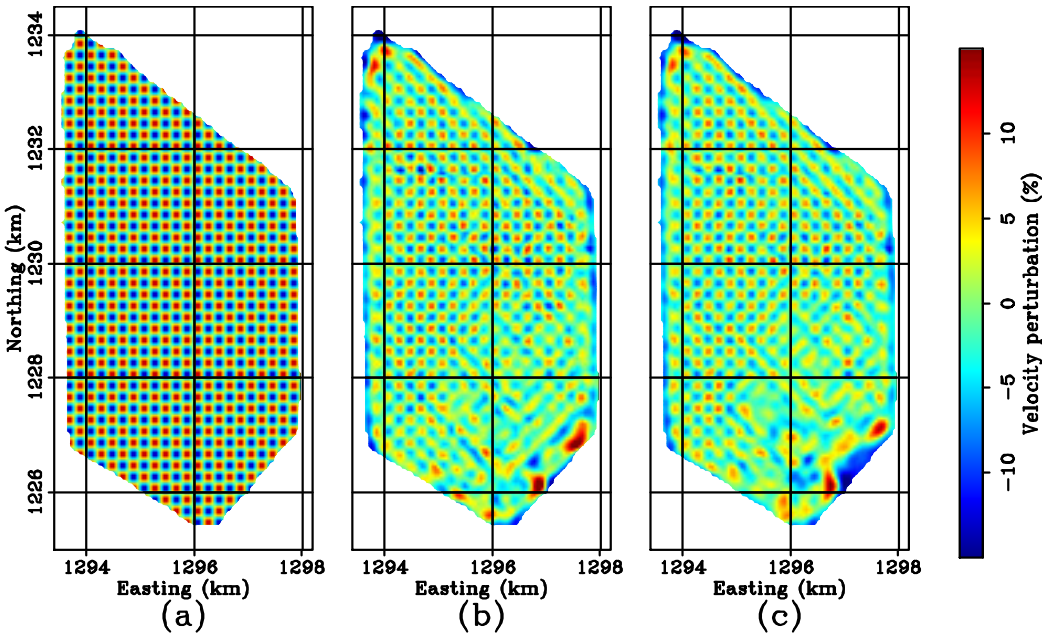

Figure 3.17: Checkerboard tests with checkers spanning 200 m × 200 m squares. (a) True model. (b) Recovered checkerboard using ray coverage associated with inversion at 3.0 Hz. (c) Recovered checkerboard using ray coverage associated with inversion at 3.5 Hz. [**CR**] chap3/. checker200

Overall, these results demonstrate that a cost-effective, non-invasive technique like passive seismic interferometry can benefit fields interested in the near surface, such as earthquake hazard analysis and foundation design. Shear velocity is proportional to the impedance of the material, and seismic wave amplitudes typically increase with lower impedance (Wills and Silva, 1998). Thus, regions with low shear velocity (and hence low impedance) at shallow depths are more susceptible to earthquake-induced damage than regions with high shear velocity. Although Rayleigh wave group velocities are not a direct measurement of shear velocity, group velocity dispersion curves can be inverted to obtain shear velocity estimates as a function of depth (e.g., Wu et al., 1997; Karagianni et al., 2005). These velocity maps can constrain group velocity dispersion curves at high frequencies and thus help constrain shear velocity

estimates in the near surface. While active seismic surveys could produce similar results, the required cost and manpower, particularly in urban settings, make them less appealing than passive approaches.

CONCLUSIONS

In this chapter, I showed that the non-invasive passive seismic interferometry approach could transform urban traffic noise into near-surface velocity maps. Using a cross-correlation technique, I was able to extract Rayleigh waves between $3 - 5$ Hz generated by traffic noise. Though noisy, the traveltimes of the fundamental-mode Rayleigh waves appeared reliable enough to perform straight-ray group velocity tomography over the entire array. From the group velocity maps at 3.0 Hz and 3.5 Hz, I was able to distinguish velocity trends that agree with a geologic map of the survey area. Among the most prominent features resolved are a region of less-consolidated material in the north, a region of more-consolidated material in the south, Alamitos Bay, and a narrow low-velocity feature in the Newport-Inglewood Fault zone.

Overall, these results suggest that ambient-noise tomography techniques can reliably resolve shallow geologic structures in areas with dense infrastructure and urbanization. These near-surface velocities can be useful for identifying regions that are susceptible to serious damage during earthquake-related shaking. Requiring only an array of receivers and long recording times, the demonstrated methodology is a low-cost and practical alternative to traditional active seismic approaches to near-surface imaging, particularly in densely-populated urban environments.

ACKNOWLEDGMENTS

I would like to acknowledge Signal Hill Petroleum, Inc. and NodalSeismic for allowing us to use the data and to present our results. I especially thank Dan Hollis of NodalSeismic for his help and cooperation throughout the project.

Chapter 4

P-wave extraction in a shallow marine environment

While the seismic noise field in shallow marine environments is dominated by ocean-generated surface waves at low frequencies, it can be dominated by P-waves originating from natural or anthropogenic sources at very high frequencies. In this chapter, I extract high-frequency (greater than 40 Hz) P-waves from the ambient seismic noise field at the Forties ocean-bottom node array using two methods: passive seismic interferometry and passive fathometry. Seismic interferometry extracts P-waves propagating in the water layer that appear to be generated by distant seismic surveys as well as the operating platform in the center of the array. To extract a 1D reflection profile from this P-wave energy, I adapt the traditional passive fathometry approach for horizontally oriented arrays. Results indicate that this method could potentially be used to estimate the water depth in shallow marine environments.

INTRODUCTION

Extraction of the surface-wave portion of Earth's ambient seismic noise field using passive seismic interferometry has been successful at the continental, regional, and local scales (e.g., Shapiro et al., 2005; Bensen et al., 2008; de Ridder and Dellinger, 2011; Chang et al., 2016). Many studies have used the associated traveltimes of the surface waves to perform tomography and produce near-surface velocity maps,

including the previous chapter. As a result, focus has shifted to extracting the body-wave portion of the Earth's ambient seismic noise field for subsurface imaging. This task is challenging for multiple reasons, including the fact that Earth's ambient seismic noise field is dominated by surface waves due to most noise sources being located near the surface, and because surface waves are subject to less attenuation and weaker geometrical spreading effects than body waves.

At the local scale on land, Nakata et al. (2011) and Draganov et al. (2013) were able to recover reflection events from passive seismic data collected in seismically quiet regions containing major roads. The subsequent reflections from both studies were then migrated to obtain shallow reflection images. Additionally, Nakata et al. (2015) were able to recover diving P-waves using a dense array at Long Beach, California, which were subsequently used to produce a 3D tomographic image of the subsurface. Each of these studies employed methods to enhance the body-wave energy in the presence of relatively strong surface waves (e.g., f-k filtering to dampen surface-wave arrivals, selecting times with relatively strong body-wave arrivals).

There have also been successful examples of extracting non-surface waves in shallow marine environments. Using continuous recordings from an ocean-bottom cable network in the Valhall oil field, Mordret et al. (2013) extracted an apparent acoustic wave generated by an operating platform using passive seismic interferometry. Using a small L-shaped (vertical and horizontal) hydrophone array in offshore New Jersey, Brooks and Gerstoft (2009) extracted direct, sea-surface reflected, and sea-bottom reflected events in the water column generated by shipping and breaking-wave noise using similar techniques. In a different approach, a collection of studies (e.g., Gerstoft et al., 2008a; Siderius et al., 2010) introduced a technique called passive fathometry to obtain shallow subsurface reflection images using energy generated by breaking waves at the sea surface recorded by vertically-oriented geophone and hydrophone arrays in the water column. The method effectively performs up-down separation of naturally occurring acoustic energy using an adaptive beamforming approach to limit the influence of broadside energy. Each of these studies focused on high frequencies (greater than 20 Hz) to extract these P-waves.

In this chapter, I attempt to extract acoustic P-waves from a shallow marine environment using both traditional passive seismic interferometry and an adaptation of passive fathometry. First, I introduce the continuous ocean-bottom node recordings

from the Apache Forties dataset and discuss the temporal and spatial patterns in the ambient seismic noise field. Second, I apply passive seismic interferometry processing with phase-weighted stacking to generate high-frequency ($40 - 80$ Hz) virtual source gathers throughout the array and across different time periods. To get a sense of the directionality of the events, I examine virtual source gathers along approximate lines of receivers in the north-south and east-west directions across different time periods. I then perform linear moveout on these source gathers to estimate the apparent velocities of these events. Finally, I adapt traditional passive fathometer processing for use on horizontal arrays in an attempt to recover 1D reflection profiles of the subsurface. Results appear to retrieve the water-column multiple, whose timing can be used to estimate water depth.

CONTINUOUS RECORDINGS AT APACHE FORTIES

The Forties data set, provided by the Apache Corporation, consists of three clusters of ocean-bottom nodes (OBNs) centered at three different platforms in the North Sea. The four-component nodes were deployed as part of an active seismic survey aimed at imaging shallow gas pockets that could pose potential drilling hazards. In this chapter, I examine the hydrophone and vertical-geophone components of the Bravo group of OBNs. This cluster of OBNs consists of 52 nodes arranged in a hexagonal shape and centered around an operating platform (Figure 4.1). The average node spacing is 50 m, and the maximum array offset is approximately 400 m. Each node continuously records for approximately 4 days at 2 ms sampling and is located roughly 120 m below the sea surface.

I perform basic preprocessing to prepare the continuous recordings for ambient seismic noise processing. First, the geophone recordings are rotated into standard north-east-vertical orientation using the provided tilt angles (Levin and Chang, 2015). Next, the continuous recordings from each node are rounded up to the nearest quarter of an hour and rounded down to the nearest quarter of an hour, as not all nodes were deployed at the same time. Because the convergence of cross-correlations is improved by stacking results over short time windows (Seats et al., 2012), I segment the continuous recordings from each node into tapered 30-minute time windows with 50% overlap. This procedure results in 307 time windows spanning over 3.1 days.

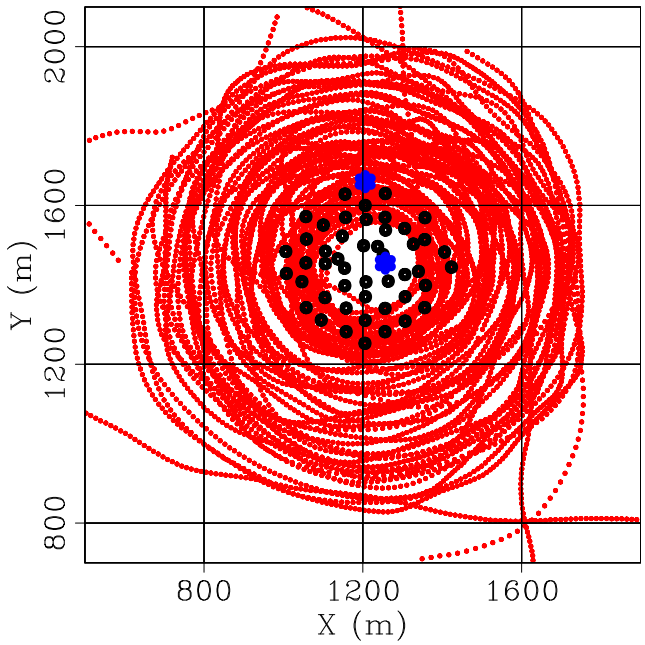

Figure 4.1: Map of the Apache Forties acquisition survey. Black points: receivers. Red points: shot locations. Blue points: nodes used for spectrograms. The operating platform is located in the center of the cluster of nodes. Coordinates have been redatumed. [**CR**] chap4/. forties-map

Because I am interested in extracting P-waves from the ambient seismic noise field at Forties, I focus on data collected during quiet periods. Thus, it is important to determine which time windows contain active seismic shooting so they can be excluded from further analysis. To characterize the type of seismic energy being recorded by the array, I generate spectrograms for nodes near the platform and north of the platform (blue points; Figure 4.1). I create a spectrogram for a single node by estimating the logarithm of the power spectrum of each 30-min window and plotting the results from each time window side-by-side. Note that the instrument responses of the hydrophone and geophones have not been removed, so the approximate amplitude roll-offs below 30 Hz and above 200 Hz have not been accounted for (Figure 4.18).

The low-frequency seismic energy recorded by the hydrophones near the platform and north of the platform (Figures 4.2a and b, respectively) share similar patterns. First, the consistent high-spectral power at frequencies below 1 Hz are a nice example of microseism energy, which is constantly being generated by the natural interaction of ocean waves. Closer inspection of the lower end of the microseism energy (approximately 0.2 Hz) indicates a gradual increase in relative power over time between

days $110-110.5$ and days $112.5-113$. This signature is indicative of stormy weather, where ocean waves become move violent and thus generate stronger microseisms. Second, the comb patterns across frequencies between $2-5$ Hz during certain time periods are indicative of a consistent signal reaching the nodes at regular time intervals. This repeating signal is related to active seismic shooting. Here, each tooth of the comb is separated by approximately $1/7$ Hz, indicating a length of 7 s between each seismic shot.

Note that whenever the microseism energy begins to increase in power (e.g. days 110.25 and 112.5), active seismic shooting stops. This is an indication that there are stormy weather conditions during the Forties recording period, which create ideal conditions for extracting signal from ambient seismic noise in ocean-bottom environments by not only halting active seismic surveys but also by generating stronger seismic signals to extract. For instance, Brooks and Gerstoft (2009) showed that stormy weather produces more breaking waves at the sea surface, which enable better extraction of vertically-propagating energy in the water column. Additionally, de Ridder and Dellinger (2011) suggested that stormy weather was ideal for extracting Scholte waves from microseism energy recorded by OBNs.

When focusing on the full frequency range (up to 250 Hz) for the same hydrophones (Figure 4.3), the times of active seismic shooting are even clearer, as their signatures extend across nearly the entire frequency band. Because I am also working with vertical-component geophones, I show their corresponding spectrograms in Figure 4.4. While their corresponding signature of active seismic shooting is similar to that seen in the hydrophones, there is a pattern that is only observed in the vertical-component geophones. Focusing on frequencies below 40 Hz, there is strong spectral power only when the geophone is near the platform. Combined with the fact that geophones are coupled to the ground whereas hydrophones are coupled to the water, this particular energy is likely related to platform-generated Scholte waves. Because I am interested in energy propagating close to vertical when looking for P-waves, I will focus on frequencies over 40 Hz to avoid this energy when performing further analysis.

To identify the time windows containing active-source seismic shooting, I calculate the maximum absolute amplitude of all traces and discard those with corresponding values over a certain threshold. After filtering out these time windows, I am left

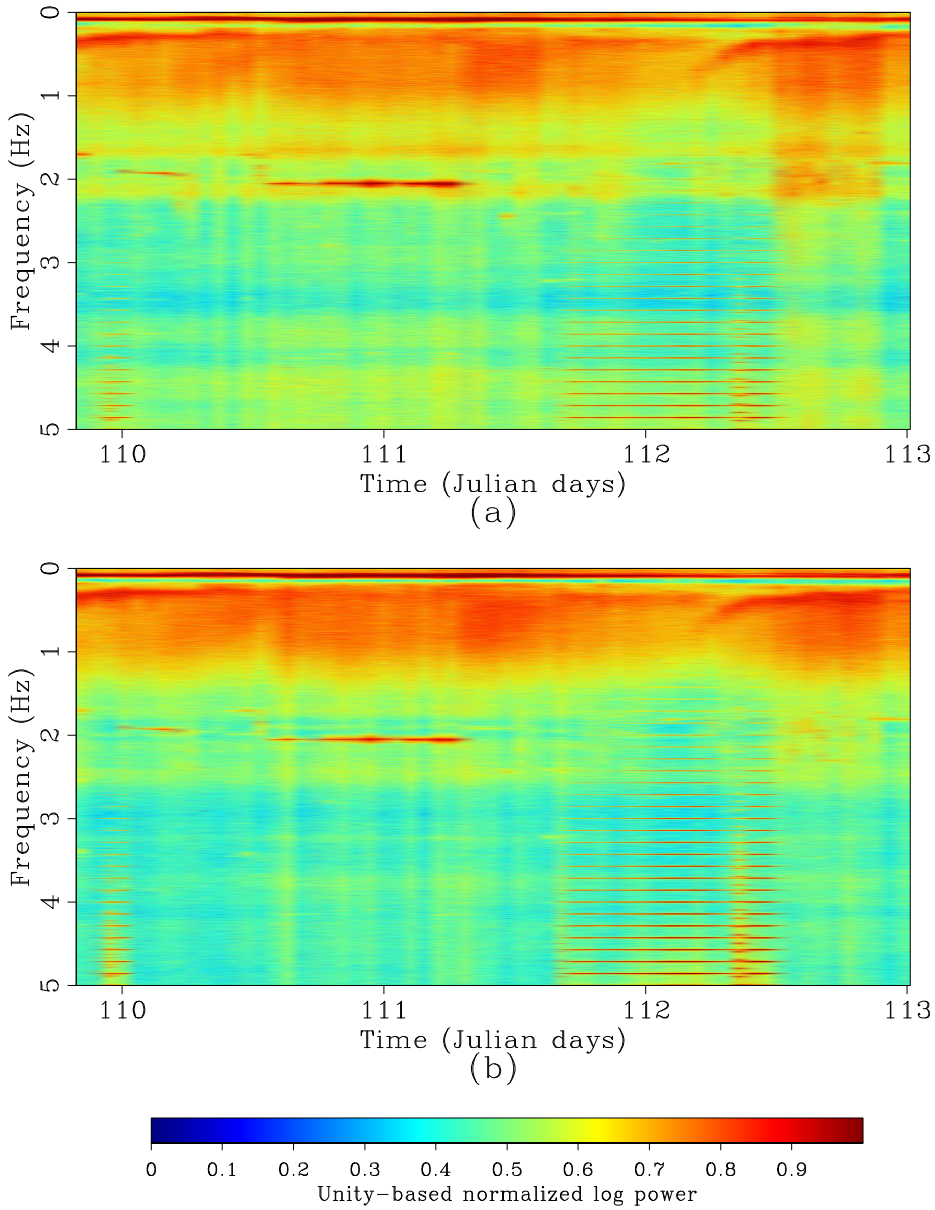

Figure 4.2: Hydrophone spectrograms up to 5 Hz for a node (a) near the platform, and (b) north of the platform (see Figure 4.1 for node locations). Spectrograms are clipped identically so that comparisons can be made. [**CR**] chap4/. forties-h-sp-lo

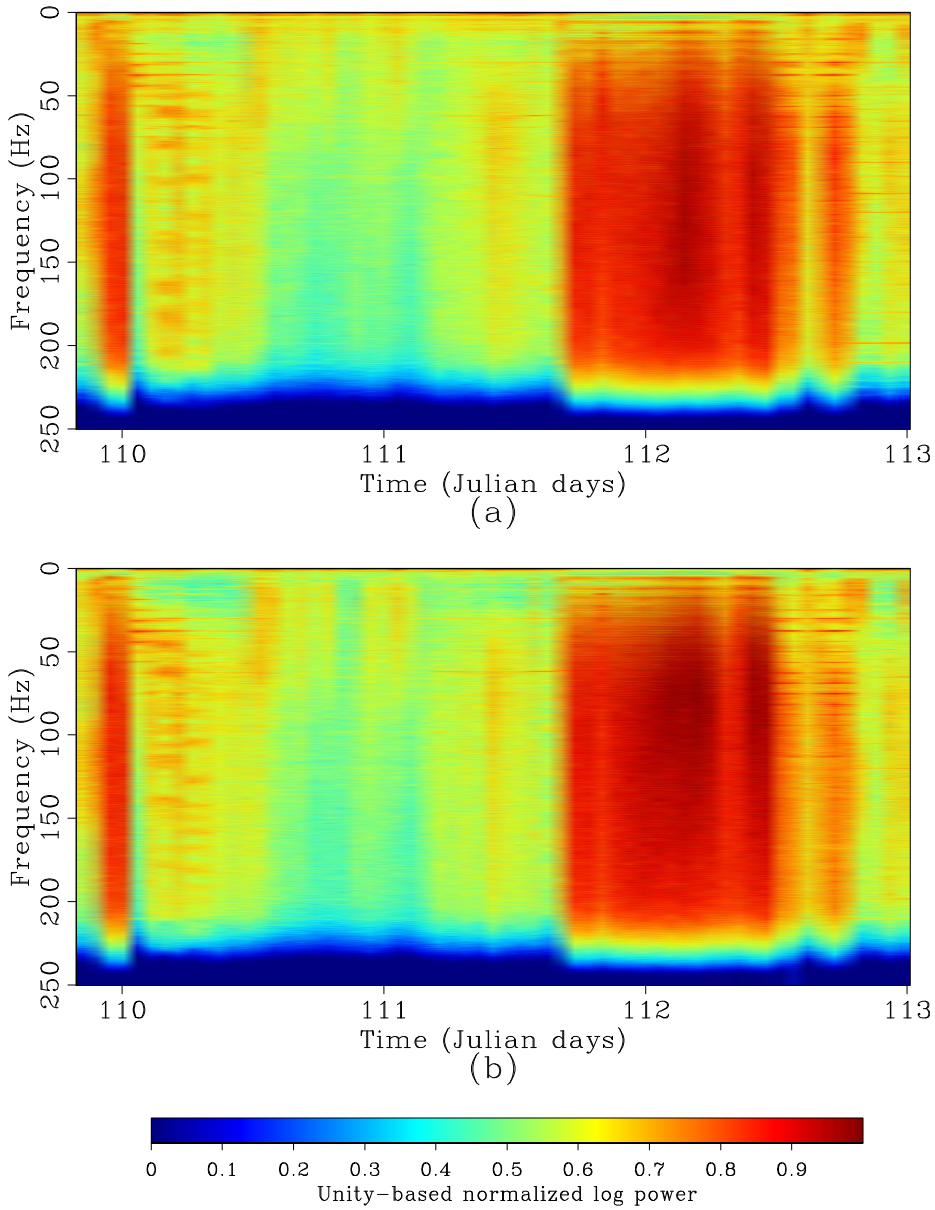

Figure 4.3: Hydrophone spectrograms up to 250 Hz for a node (a) near the platform, and (b) north of the platform (see Figure 4.1 for node locations). Spectrograms are clipped identically so that comparison can be made. [**CR**] chap4/. forties-h-sp-hi

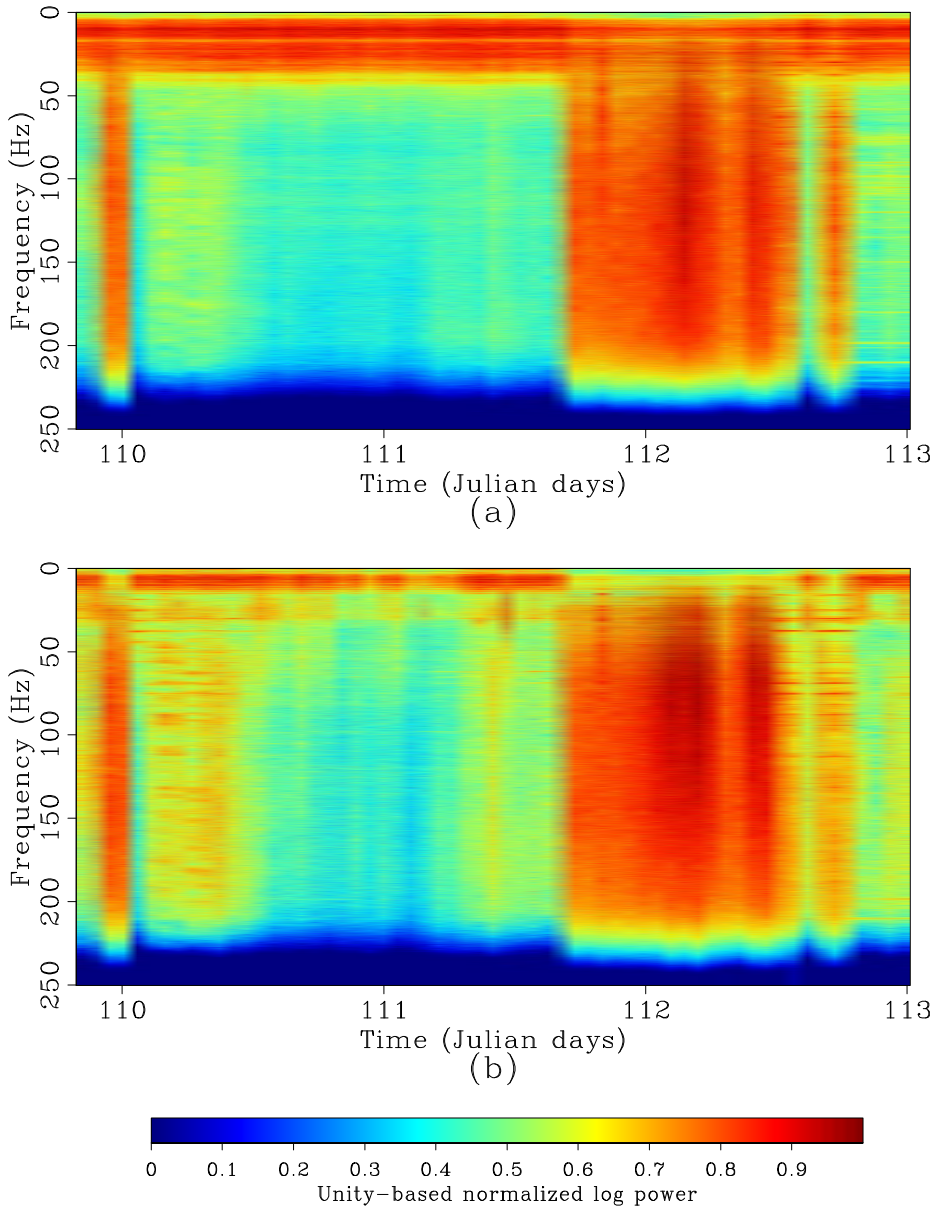

Figure 4.4: Vertical-geophone spectrograms up to 250 Hz for a node (a) near the platform, and (b) north of the platform (see Figure 4.1 for node locations). Spectrograms are clipped identically so that comparison can be made. [**CR**] chap4/. forties-v-sp-hi

with 193 30-min time windows, which span approximately 2 days. I also remove all spurious nodes, which leaves 49 of 52 nodes to work with. These time windows compose the passive seismic data that I will use for further analysis.

Looking more closely at the spectrograms of the remaining times of no active seismic shooting, there appear to be roughly three different quiet periods. To make these time periods clearer, I display these three periods for the hydrophone near the platform in Figure 4.5; these are the same spectrograms in Figure 4.3a but divided up. The first is an 8.25-hour period (T1) after the first round of active seismic shooting (Figure 4.5a), where there is relatively high power across all frequencies. Note that this is a time period associated with the storm. Looking at this time period in the other spectrograms, spectral power appears to be stronger north of the platform than near the platform, which could be indicative of a strong source north of the array. The second time period (T2) is a 15.0-hour period after period T1, when there is relatively less power across frequencies (Figure 4.5b). This could be indicative of a truly quiet period when there are no strong sources outside the array. The third time period (T3) is a 10.0-hour time window with a weaker but similar spectral pattern as T1 (Figure 4.5c). Again, it appears that spectral power is higher closer north of the platform than close to the platform, which suggests that this could be a strong source north of the array. I will analyze the passive seismic data from each of these time period independently in the next section to determine how noise sources change over time.

PASSIVE SEISMIC INTERFEROMETRY

Passive seismic interferometry is performed by effectively cross-correlating the recordings of ambient seismic noise at two receivers. Under certain conditions, the result is an estimate of the Green's function between the two receivers (Wapenaar et al., 2010). By correlating the recording at one receiver with recordings from all other receivers, one can create virtual source gathers, much like in the previous chapter.

To perform passive seismic interferometry on the Forties' passive seismic data, I calculate the averaged whitened coherency (Weemstra et al., 2014) between each pair of nodes over all 30-min time windows. This procedure is also referred to as calculating the cross-coherence. By normalizing the input spectra by a smoothed

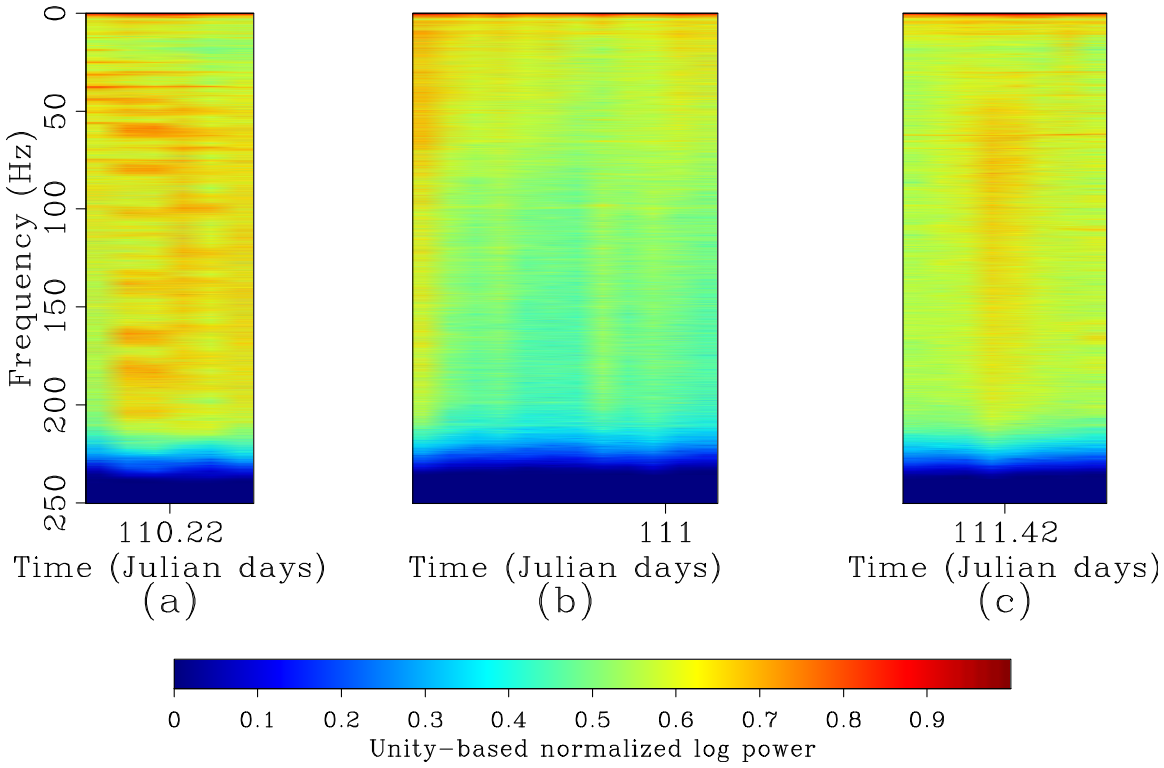

Figure 4.5: Hydrophone spectrogram for the node close to the platform over different time periods of no active seismic shooting. (a) T1: 8.25-hour time window beginning at Julian day 110.05 (right after the first period of active seismic shooting). (b) T2: 15.0-hour time window beginning at Julian day 110.48 (after T1). (c) T3: 10-hour time window beginning at Julian day 111.21 (after T2). All panels are clipped and scaled identically. [**CR**] chap4/. forties-32-spH-quiet-hi

version of the amplitude spectra, the approach typically increases the bandwidth of the signal without modifying the phase information. In the frequency domain, the procedure is generally expressed as:

$$[G(x_B, x_A, \omega) + G^*(x_B, x_A, \omega)] = \left\langle \left(\frac{U(x_B, \omega)}{\{|U(x_B, \omega)|\}} \right) \left(\frac{U^*(x_A, \omega)}{\{|U(x_A, \omega)|\}} \right) \right\rangle, \qquad (4.1)$$

where G is the Green's function between two receiver locations (x_A, x_B), $U(x, \omega)$ is the spectrum of the wavefield at a given receiver location x, $*$ is the complex conjugate, $\langle \cdot \rangle$ is an averaging operation, $|\cdot|$ is the magnitude of the spectrum, and $\{\cdot\}$ is a 0.003 Hz running window average used for normalizing the signal. The result is then inverse Fourier transformed into the time domain. Given the parameters of the data set, I used this procedure to estimate over 450 thousand Green's functions (193 time windows $\times$ 49^2 receiver pairs).

I employ two processing procedures enhance potential P-waves. First, I frequency bandpass the resulting estimated Green's functions (EGFs) for frequencies between $40 - 80$ Hz. As conjectured based on the spectrograms in the previous section, the platform generates Scholte waves below 40 Hz. By ignoring frequencies below 40 Hz, I can avoid extracting surface-wave energy. Second, I perform phase-weighted stacking across all time windows rather than standard linear stacking. Phase-weighted stacking is a method that suppresses incoherent noise better than linear stacking, and can thus be effective at detecting weak but coherent arrivals (Schimmel and Paulssen, 1997; Schimmel et al., 2011) such as P-waves. The method essentially weighs each time sample from the linear stack by a stack based on the corresponding instantaneous phase (called a phase stack). Time samples with incoherent instantaneous phase are weighted toward 0, while time samples with coherent instantaneous phase are weighted toward 1. Specifically, the weight is the stack of the corresponding sample-by-sample-normalized analytic traces. In equation form, the phase-weighted stacking procedure is expressed as:

$$p(t) = \frac{1}{N} \sum_{j=1}^{N} s_j(t) \left| \frac{1}{N} \sum_{k=1}^{N} \exp\left[i \Phi_k(t) \right] \right|^v, \qquad (4.2)$$

where $p(t)$ is the phase-weighted stack result, N is the number of traces being stacked, $s_j(t)$ are the traces being stacked, $\Phi_k(t)$ is the instantaneous phase of the trace, and v is a phase sharpness factor (chosen empirically here to have a value of 2). Though

this stack is not a linear procedure, the time-consistent signal in the stack should not be distorted much while incoherent noise in the stack is dampened to allow weaker coherent signals to become more apparent.

Virtual source gathers sorted by absolute offset

I first create source gathers with a virtual source located near the platform (centered blue point in Figure 4.1) for frequencies between $40 - 80$ Hz. Traces are sorted by absolute offset. To compare the effects of the two processing approaches on virtual source gathers, I plot the results from using linear stacking and using phase-weighted stacking.

Focusing on the hydrophone-hydrophone (PP) virtual source gathers, there are similar events extracted when using linear stacking (Figure 4.6a) and when using phase-weighted stacking (Figure 4.6b). Specifically, there appear to be linear events with apparent velocities close to water velocity at both positive and negative time lags, and another linear event with apparent velocity faster than water velocity at only positive time lags. Because positive time lags correspond to wavefields propagating away from the virtual source while negative time lags correspond to wavefields propagating toward the virtual source, these events are likely generated by sources outside of the array rather than the platform. However, phase-weighted stacking appears to reveal a faster-propagating, earlier-arriving event at positive times lags that is not as apparent with linear stacking.

Focusing on the vertical-vertical geophone (ZZ) virtual source gathers, there is a dramatic difference when using linear stacking and when using phase-weighted stacking. When using linear stacking (Figure 4.7a), there is one clear event at only positive time lags. This suggests that this event is moving away from the virtual source location, which in this case is away from the operating platform. When using phase-weighted stacking (Figure 4.7b), not only is the previously mentioned event apparent but also a second, later event at positive time lags that appears to have similar move-out velocity. The intercept time of this second event is approximately 0.15 s, which is close to the two-way traveltime through the water column (given an approximate water depth of 120 m and a water velocity of 1500 m/s).

In general, phase-weighted stacking appears to sharpen the events in the virtual

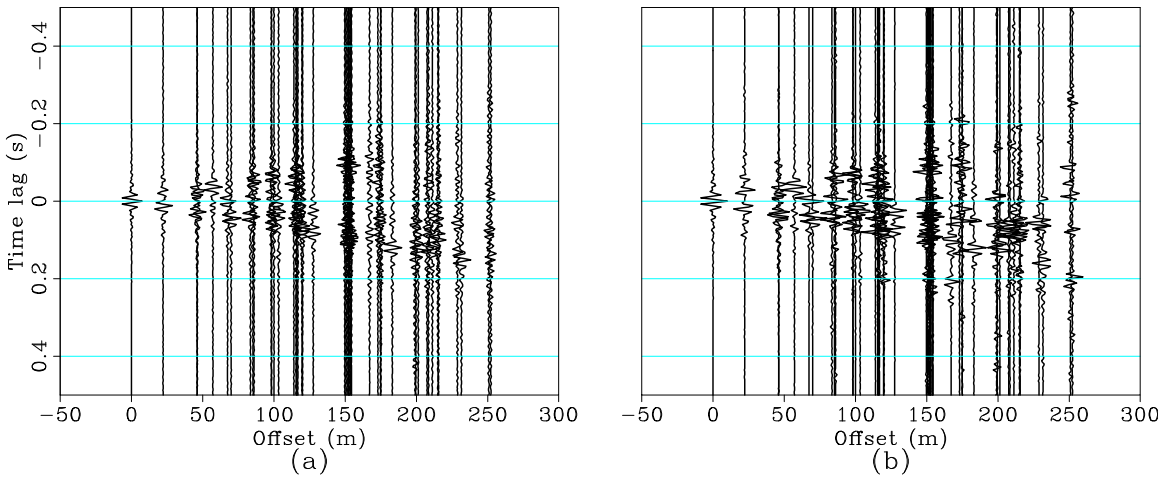

Figure 4.6: PP source gathers for frequencies between $40 - 80$ Hz with the virtual source located near the platform (centered blue star in maps in Figure 4.1). Traces are sorted by absolute offset. (a) Using linear stacking. (b) Using phase-weighted stacking. [**CR**] chap4/. forties-HH-abs

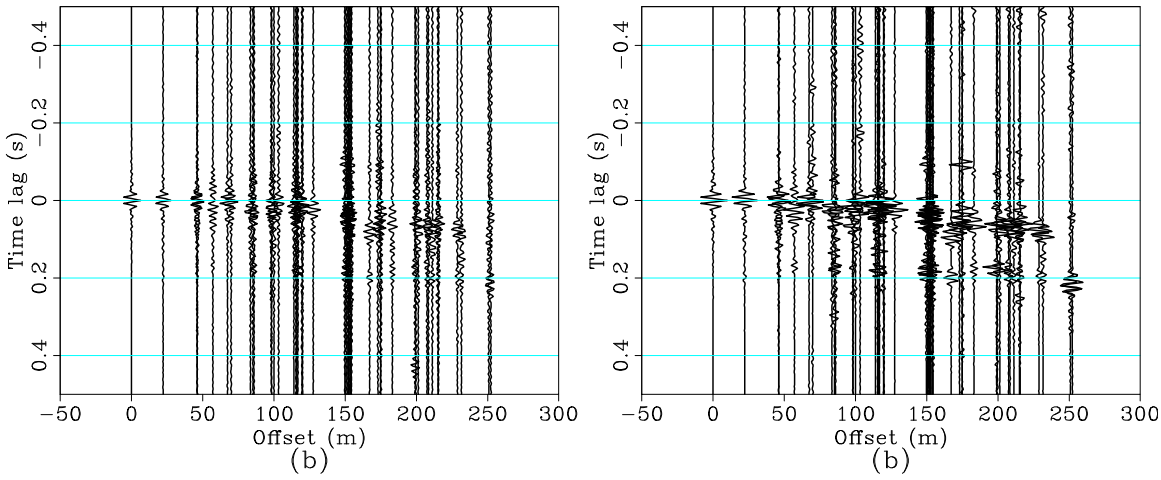

Figure 4.7: Vertical-vertical geophone source gathers for frequencies between $40 - 80$ Hz with the virtual source located near the platform (centered blue star in maps in Figure 4.1). Traces are sorted by absolute offset. (a) Using linear stacking. (b) Using phase-weighted stacking. [**CR**] chap4/. forties-VV-abs

source gathers. This non-linear stacking procedure appears to particularly reduce noise in the ZZ correlations, allowing the secondary event at later positive time lags to become more apparent. Though phase-weighted stacking appears to weaken the dominant arrivals in the PP correlations, it seems to also dampen the overall amount of noise as well as reveal a faster-propagating event at positive times lags not apparent in when using linear stacking.

Overall, these virtual source gathers sorted by radial offset appear to reveal three clear events:

1. A strong linear event propagating towards and away from the platform, observed in the PP correlations (Figure 4.6).

2. A strong, faster linear event with 0 s intercept time propagating away from the platform, observed in both the PP and ZZ correlations (Figures 4.6 and 4.7, respectively).

3. A weaker but fast linear event with approximately 0.15 s intercept time propagating away from the platform, observed in the ZZ correlations (Figure 4.7; most evident at far offsets).

Virtual source gathers along different receiver lines

To understand the direction of propagation of each of these events beyond just towards or away from the platform, I create virtual source gathers along two receiver line orientations: north-south and east-west (Figure 4.8). To understand how the potential sources of passive seismic energy change over time, I also display these virtual source gathers stacked over four time periods (based on the temporal divisions in Figure 4.5): all times, period T1, period T2, and period T3. For the virtual source gathers stacked across all times, I perform linear moveout (LMO) to estimate moveout velocities of the observed linear events. While beamforming is typically an effective way to estimate the directionality and propagation velocity of these events, it is not effective in this scenario due to the spatial aliasing artifacts when working at such high frequencies and relatively large average receiver separations. Note that I use results from phase-weighted stacking for all figures in this section.

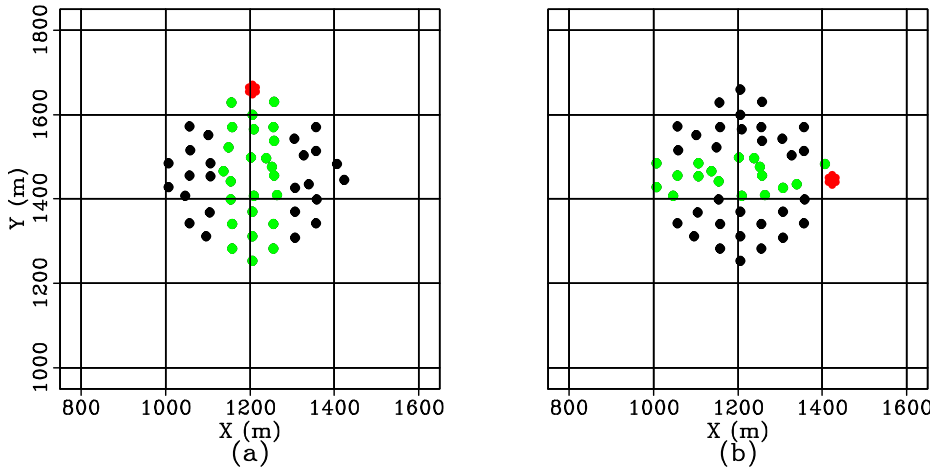

Figure 4.8: Map of different receiver line orientations. (a) North-south. (b) East-west. Red points are virtual source locations while green points are receiver subsets. [**CR**] chap4/. forties-lines

I first focus on apparent north-south receiver lines. Looking at the PP source gather with a virtual source located in the north of the array stacked over all recording times (Figure 4.9a), there are indications of two types of events. At positive time lags, there is a clear linear event. Because the virtual source is located north of the platform, the asymmetric signal (in time) indicates that this particular event is propagating south toward the platform. Since energy is moving away from the virtual source, I perform LMO centered at the virtual source location with a velocity of 1500 m/s and find that this particular event is flattened (Figure 4.9b). Therefore, it appears that this particular event originates north of the array and propagates at approximately water velocity.

At negative time lags, there is a clear event with a peak centered at an offset of approximately -200 m. This 'V'-shaped pattern is indicative of an active source within the line of receivers, and the peak of this event corresponds to the approximate location of the operating platform. Because energy appears to move away from the platform location, I perform LMO centered at the platform location (rather than the virtual source location) with an apparent velocity of 3000 m/s. Doing so appears to flatten the event (Figure 4.9c).

The corresponding PP virtual source gathers stacked over the three different time periods are displayed in Figure 4.10. Over period T1 (Figure 4.10a), there is a clear linear event at negative time lags, which suggests that energy is propagating across

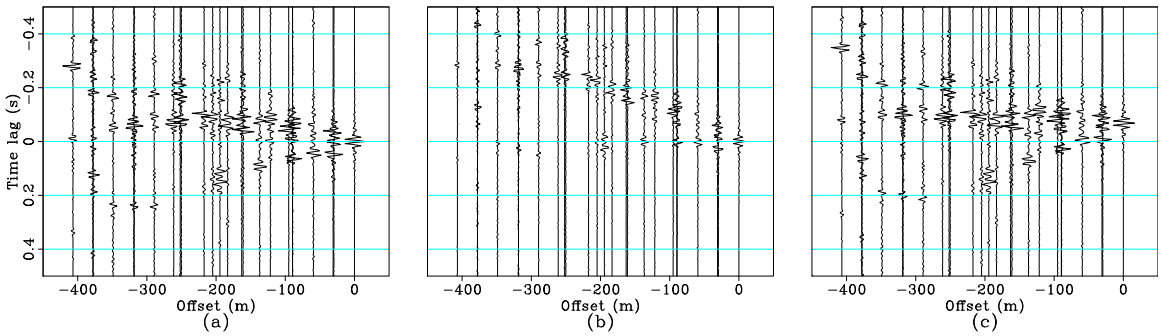

Figure 4.9: PP source gathers corresponding to a virtual source in the north of the array after phase-weighted stacking over all times for frequencies between $40-80$ Hz with receivers along approximate lines in the north-south direction. (a) Original source gather. (b) Source gather after LMO at 1500 m/s centered at the virtual source location (0 m offset). (c) Source gather after LMO at 3000 m/s centered at the platform location (-200 m offset). Negative offsets correspond to receivers toward the south. [**CR**] chap4/. forties-s03-nslinesHH

the array from south to north. Because this event does not display the 'V' shape associated with platform noise, this energy is likely propagating at water velocity. Over period T2 (Figure 4.10b), the previously observed 'V'-shaped pattern is clear, which is indicative of platform-generated energy. Over period T3 (Figure 4.10c), there is a dominant linear event propagating at water velocity at positive time lags, which suggests that energy is propagating across the array from north to south. This is the opposite of the pattern observed during period T1. These patterns are potentially indicative of differences in relative locations of distant seismic surveys or shipping noise.

The 'V'-shaped pattern at negative time lags and centered at the approximate platform location is clearly observed when looking at the corresponding ZZ virtual source gathers after stacking over all time periods (Figure 4.11a). Additionally, there is a clear second event at greater negative time lags with similar 'V'-shape and move-out velocity. This secondary event likely corresponds to the secondary event at positive time lags in the ZZ virtual source gather sorted by radial offset (Figure 4.7), with the differences in intercept time and time lags due to differences in the relative locations of virtual sources and receivers for the gathers. Performing LMO using a velocity of 3000 m/s centered at the platform location flattens both these events (Figure 4.11b).

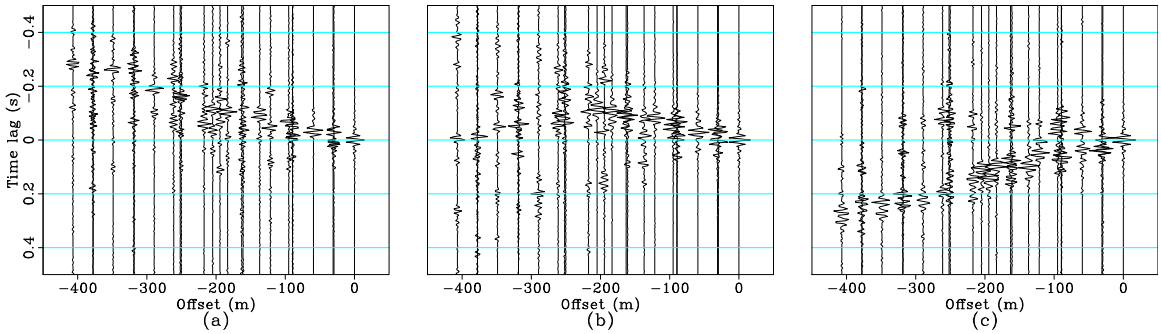

Figure 4.10: PP source gathers corresponding to a virtual source in the north of the array after phase-weighted stacking over different quiet time periods for frequencies between $40 - 80$ Hz with receivers along approximate lines in the north-south direction. (a) Period T1. (b) Period T2. (c) Period T3. [**CR**] chap4/. forties-s03-nslinesHH-quiet

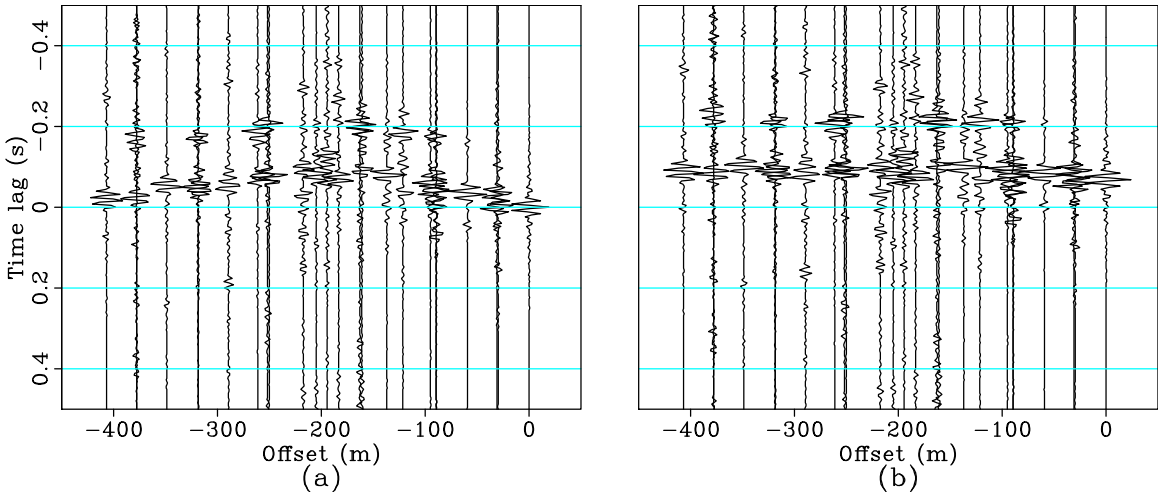

Figure 4.11: ZZ source gathers corresponding to a virtual source in the north of the array after phase-weighted stacking over all times for frequencies between $40 - 80$ Hz with receivers along approximate lines in the north-south direction. (a) Original source gather. (b) Source gather after LMO at 3000 m/s centered at the platform location (-200 m offset). Negative offsets correspond to receivers toward the south. [**CR**] chap4/. forties-s03-nslinesVV

The corresponding ZZ virtual source gathers stacked over the three different time periods are displayed in Figure 4.12. Over period T1 (Figure 4.12a), there is a strong linear event at negative time lags. This indicates that energy is propagating from south to north at water velocity, which is very similar to the corresponding PP virtual source gather. Over periods T2 and T3, the platform energy dominates the virtual source gathers. Note that there are indications of a linear event at positive time lags, which corresponds to energy propagating at water velocity from north to south (similar to the corresponding PP virtual source gathers).

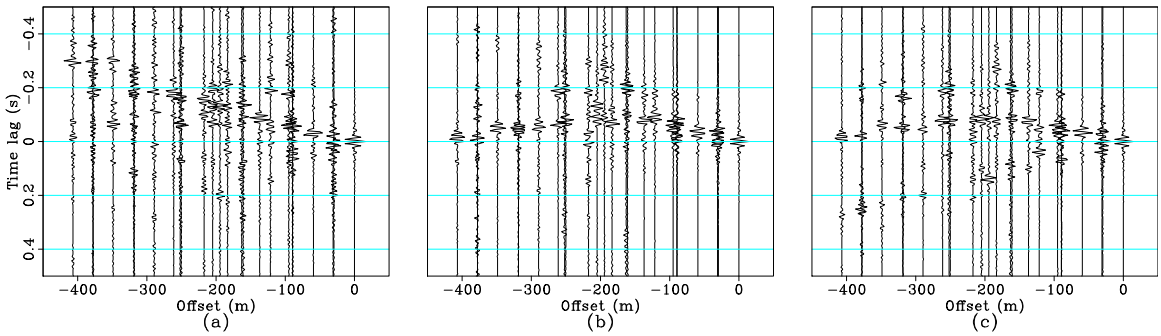

Figure 4.12: ZZ source gathers corresponding to a virtual source in the north of the array after phase-weighted stacking over different quiet time periods for frequencies between $40 - 80$ Hz with receivers along approximate lines in the north-south direction. (a) Period T1. (b) Period T2. (c) Period T3. [**CR**] chap4/. forties-s03-nslinesVV-quiet

Similar observations can be made when looking at source gathers along an apparent line of receivers in the east-west direction and a virtual source in the east of the array (Figure 4.8b). I first focus on the results from stacking over all times. From PP virtual source gathers, there are hints of a linear event at positive time lags and a 'V'-shaped event at negative time lags (Figure 4.13a). To estimate the velocity of the former event, I again perform LMO with moveout velocity of 1500 m/s with respect to the virtual source location (Figure 4.13b). It is clear that the corresponding linear event is not quite flattened. The event is pointing toward negative time lags after LMO, which suggests that the event is reaching the receivers at an apparent velocity faster than water velocity. Given the sign of the time lag, this event is propagating from east to west. Performing LMO with a moveout velocity of 3000 m/s with respect to the platform location indicates that, much like in the north-south virtual source gathers, the platform in the center of the array is the source of high-velocity events (Figure 4.13c).

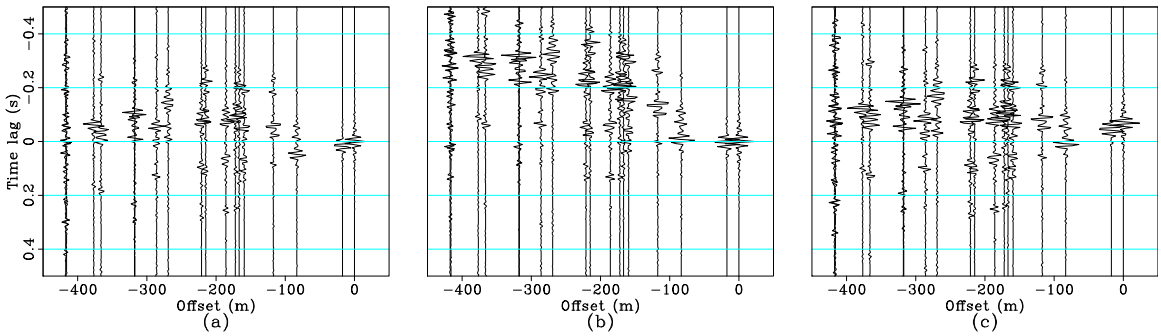

Figure 4.13: PP source gathers corresponding to a virtual source in the east of the array after phase-weighted stacking over all times for frequencies between $40 - 80$ Hz with receivers along approximate lines in the east-west direction. (a) Original source gather. (b) Source gather after LMO at 1500 m/s centered at the virtual source location (0 m offset). (c) Source gather after LMO at 3000 m/s centered at the platform location (-200 m offset). Negative offsets correspond to receivers toward the west. [**CR**] chap4/. forties-s05-ewlinesHH

The corresponding PP virtual source gathers stacked over the three different time periods are displayed in Figure 4.14. Over period T1 (Figure 4.14a), there are hints of an event that reaches all stations at nearly zero time. This pattern could be indicative of energy propagating from directly south to north (based on the previous north-south gathers), thus reaching all nodes at nearly the same time. Over period T2 (Figure 4.14b), there are hints of both the platform energy at negative time lags and a linear event at positive time lags that suggests that energy is propagating at water velocity from east to west. Over period T3 (Figure 4.14c), there is a similar linear event at positive time lags, which again suggests that energy is propagating at water velocity from east to west.

Much like in the north-south virtual source gathers, there are two 'V'-shaped events at negative time lags in the ZZ virtual source gathers along the east-west direction when stacking over all time periods (Figure 4.15a). Again, performing LMO with a velocity of 3000 m/s centered at the platform location appears to flatten these two events (Figure 4.15b). Therefore, it appears that the platform is generating multiple high-velocity events across multiple azimuths.

The corresponding ZZ virtual source gathers stacked over the three different time periods are displayed in Figure 4.16. Over period T1 (Figure 4.16a), there are hints of platform energy at negative time lags. Periods T2 (Figure 4.16b) and T3

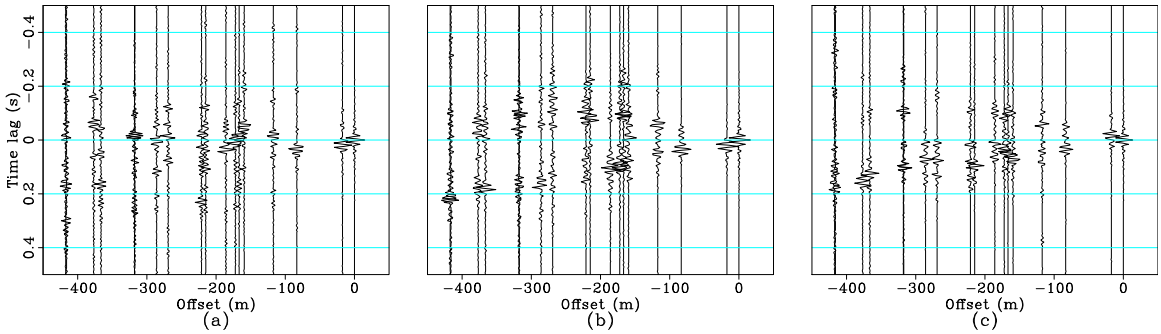

Figure 4.14: PP source gathers corresponding to a virtual source in the east of the array after phase-weighted stacking over different quiet time periods for frequencies between $40 - 80$ Hz with receivers along approximate lines in the east-west direction. (a) Period T1. (b) Period T2. (c) Period T3. [**CR**] chap4/. forties-s05-ewlinesHH-quiet

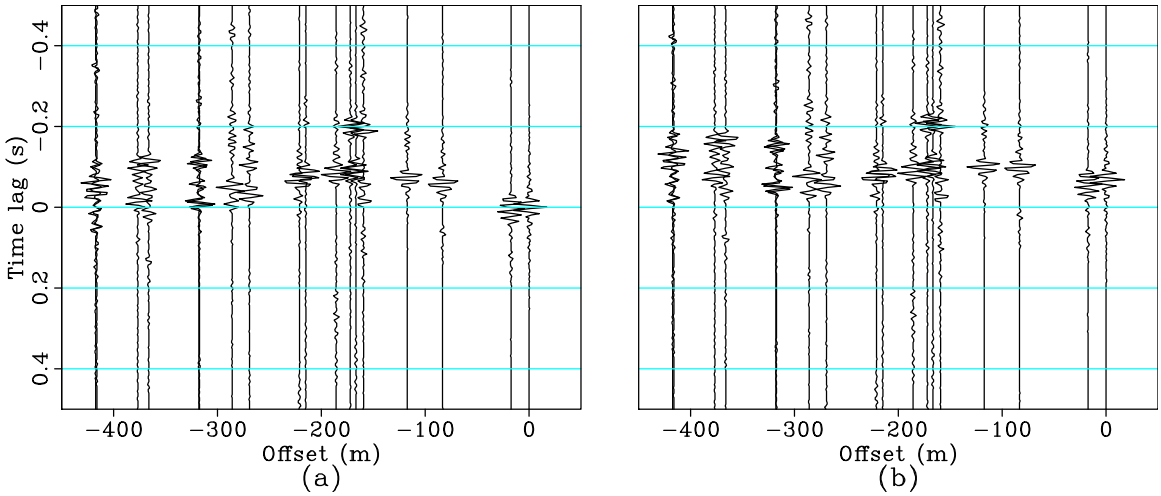

Figure 4.15: ZZ source gathers corresponding to a virtual source in the north of the array after phase-weighted stacking for frequencies between $40 - 80$ Hz with receivers along approximate lines in the east-west direction. (a) Original source gather. (b) Source gather after LMO at 3000 m/s centered at the platform location (-200 m offset). Negative offsets correspond to receivers toward the west. [**CR**] chap4/. forties-s05-ewlinesVV

(Figure 4.16c) display much clearer platform energy. This relative difference in the strength of platform-induced energy is similar to what is observed in the corresponding north-south ZZ virtual source gathers (Figure 4.12).

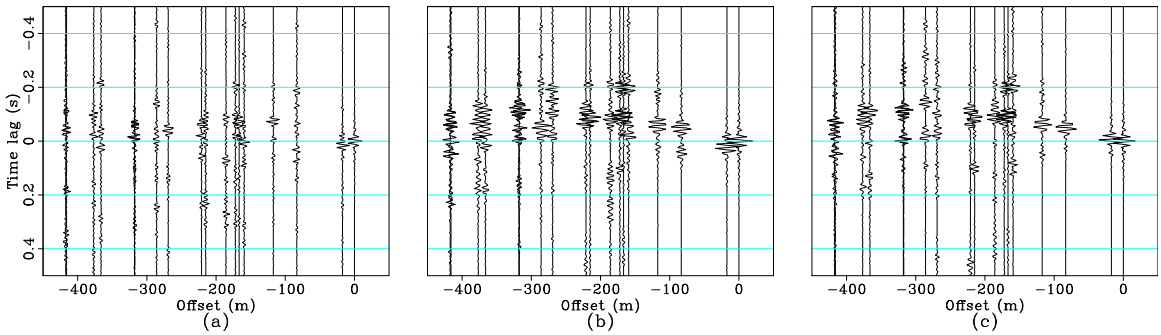

Figure 4.16: ZZ source gathers corresponding to a virtual source in the east of the array after phase-weighted stacking over different quiet time periods for frequencies between $40 - 80$ Hz with receivers along approximate lines in the east-west direction. (a) Period T1. (b) Period T2. (c) Period T3. [**CR**] chap4/. forties-s05-ewlinesVV-quiet

From these virtual source gathers along apparent receiver lines, I can elaborate on each of the three previously mentioned events in the virtual source gathers sorted by radial offset (Figures 4.6 and 4.7):

1. The linear event propagating at 1500 m/s observed in the PP virtual source gathers appears to be arriving from outside the array and propagates along different azimuths over time. Specifically, energy is arriving from due south during T1 and from the northeast during T2 and T3 (stronger during T3).

2. The linear event propagating at an apparent velocity of 3000 m/s with 0 s intercept time observed in both the PP and ZZ virtual source gathers is generated by the platform and propagates in all directions. The corresponding energy is most apparent during T2 and T3.

3. The linear event propagating at an apparent velocity of 3000 m/s with 0.15 s intercept time observed in the ZZ virtual source gathers is also generated by the platform and propagates in all directions. Again, the corresponding energy is most apparent during T2 and T3.

Given the apparent velocities of these three events, these arrivals are likely either

acoustic P-waves traveling in the water or body waves propagating through the subsurface. The events propagating at approximately 1500 m/s are likely energy traveling horizontally across the array at water velocity, which would explain why this event is relatively weak in the ZZ geophone correlations (hydrophones are coupled to water while geophones are coupled to the ground). The strong change in directionality of these events over time (particularly between T1 and T3 in Figure 4.10) suggest that the origin of these signals could changing over time. Since the sea-surface and sea-bottom effectively act as a waveguide, signals from distant sources experience little attenuation and typically display mostly horizontally-propagating wavefronts (Brooks and Gerstoft, 2009). One potential source is distant commercial shipping noise in the North Sea, which dominates the marine ambient seismic noise field at frequencies between $25 - 250$ Hz (Wenz, 1972). Another potential source is active seismic shooting from another survey in the North Sea.

As for the events propagating at an apparent velocity of approximately 3000 m/s, they are likely energy traveling with some vertical component of movement because they are clearly observed in both the PP and ZZ virtual source gathers (particularly the primary event closer to zero intercept time). Though they could be body waves propagating through the subsurface, it appears more likely that they are both acoustic P-waves traveling through the water layer. This is because the secondary event propagating at an apparent velocity of 3000 m/s in the ZZ virtual source gathers has an intercept time approximately 0.15 s after the intercept time of the primary event, which is approximately the two-way traveltime of a vertically-propagating wave reverberating through a water column 120 m deep.

Additionally, the source of these high-velocity events appears to be the platform, and it is strong across time periods T2 and T3. Note that these times are not during stormy weather (time period T1). While it is possible that the apparent acoustic P-waves are due to breaking waves hitting the side of the platform, the fact that these platform-generated events are not more apparent during stormy weather suggests that the source of energy could be normal operations on the platform. Alternatively, the energy from the platform during stormy weather could just be masked by the strong source to the north. Regardless of the true source of platform energy, given an apparent velocity of 3000 m/s and assuming a plane wave traveling through the water at 1500 m/s, P-wave energy could be hitting the array at approximately 30 degrees with respect to normal. Assuming there is indeed some vertical component of propagation

to these high-velocity events, there is potential to obtain subsurface reflections. I turn to passive fathometer processing in an attempt to extract these types of reflections from the ambient seismic noise field.

PASSIVE FATHOMETRY

Passive fathometry is based on the idea that the cross-correlation of energy generated from breaking waves at the sea surface and its echo return from the seabed can be used to estimate traveltimes to subsurface reflectors. Therefore, the technique is similar to passive seismic interferometry in that both approaches are based on the cross-correlation of noise wavefields. It has been successfully applied to vertical arrays of hydrophones and geophones in shallow marine environments (Gerstoft et al., 2008a; Siderius et al., 2010). The vertical orientation of these arrays allows for efficient separation of up- and down-going events using an adaptive beamforming approach. Here, I adapt this processing procedure for use with horizontally oriented ocean-bottom arrays and apply the procedure to individual nodes in an attempt to extract reflection profiles beneath select OBNs.

PZ summation for up- and down-going wavefield separation

Because passive fathometry depends on the separation of up- and down-going energy in the water column, I need a method for similar separation with a horizontal array. Many OBN arrays contain both vertical-geophone and hydrophone components, making it possible to perform up- and down-going wavefield separation using PZ summation. In the acoustic decomposition (Schalkwijk et al., 1999), the up- and down-going pressure wavefields are obtained by:

$$P_{\text{up}}(\omega,k) = \frac{1}{2}\left[P(\omega,k) + a(\omega)\frac{\rho}{q(\omega,k)}Z(\omega,k)\right] , \tag{4.3}$$

and

$$P_{\text{down}}(\omega,k) = \frac{1}{2}\left[P(\omega,k) - a(\omega)\frac{\rho}{q(\omega,k)}Z(\omega,k)\right] , \tag{4.4}$$

respectively, where P is the pressure component, Z is the vertical velocity component, ω is frequency, k is horizontal wavenumber, ρ is density of water, and q is vertical slowness in the water layer defined as $q(\omega,k) = \sqrt{c^{-2} - p^2(\omega,k)}$, where c is water

velocity and p is the ray parameter. a is a calibration filter, which accounts for the differences in coupling effects between the hydrophone and geophone.

I apply passive fathometry to individual nodes rather than to between different pairs of nodes so that horizontally-propagating energy (e.g., surface waves, guided waves) can be avoided in the results. To simplify the analysis, I assume that passive seismic energy primarily arrives at the nodes at near-vertical incidence. Although virtual source gathers in the previous section suggested that the dominant events could be arriving at a 30-degree incident angle from the platform, there could be normally incident energy masked by these events. This is particularly possible in this dataset because data was recorded during a storm. Brooks and Gerstoft (2009) showed that there is more acoustic energy from breaking waves at frequencies below 100 Hz than usual during stormy periods, and that this energy propagates at higher angles.

This assumption of normally incident energy allows for a couple simplifications when estimating the calibration filter for PZ summation using active-source seismic data. First, I can focus on performing up-down separation on the zero-offset trace rather than the entire gather. Second, I can take the vertical slowness in the water layer to be the inverse of water velocity, which allows Equations 4.3 and 4.4 to simplify to:

$$P_{\text{up}}(\omega) = \frac{1}{2}\left[P(\omega) + a(\omega)\rho c Z(\omega)\right] \ , \tag{4.5}$$

and

$$P_{\text{down}}(\omega) = \frac{1}{2}\left[P(\omega) - a(\omega)\rho c Z(\omega)\right] \ , \tag{4.6}$$

respectively.

After these simplifications, I can estimate the calibration filter, a, for any node. To do so, I follow the approach from Biondi and Levin (2014) using the zero-offset active-source data. To demonstrate the steps taken when estimating the calibration filter, I show the processing steps for a single node. The initial receiver gathers with respect to a line of sources running east-west for the hydrophone and vertical-component geophones are shown in Figure 4.17 after being bandpassed for frequencies between $40-200$ Hz. The low end is selected to be 40 Hz because spectrograms from the vertical-component geophone (Figure 4.4) suggested that surface waves from the platform dominated at lower frequencies. Avoiding energy below this frequency also

allows me to avoid the low-frequency ringing effects of the air-gun bubble on the recordings. The high end is selected to be 200 Hz because acoustic energy from breaking waves becomes more dominant in the ambient seismic noise field as frequency increases. Thus, I want to include very high frequencies in the analysis.

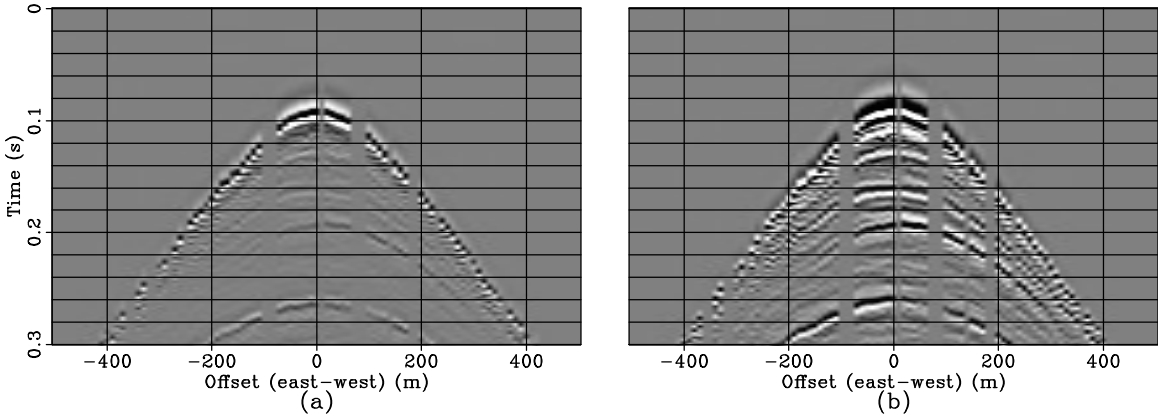

Figure 4.17: Initial receiver gathers for the (a) hydrophone and (b) vertical-component geophone for a single node. [**CR**] chap4/. forties-orig-gather

Next, I remove the provided instrument responses from both the hydrophone and vertical-geophone recordings using deconvolution. The procedure is based on dividing the recorded data by the instrument response in the frequency domain, with a noise term added in the denominator to avoid division by zero. The amplitude and phase spectra of the instrument responses are shown in Figures 4.18 and 4.19, respectively. Based on these plots, the amplitudes of the signal after instrument designature at the low and high frequencies should be boosted, and there should be clear differences in phase. After removing the instrument responses, the previous receiver gathers are more closely matched in terms of amplitude and phase (Figure 4.20). For example, the direct arrival (approximately 0.09 s) in the hydrophone receiver gather has opposite polarity as its counterpart in the vertical-geophone receiver gather, as expected.

Next, I calculate the calibration filter for the given node. This filter can be estimated by minimizing the energy of the down-going pressure field in a window containing only up-going events. Here, I use a manually-selected time window near zero offset around a shallow reflection event in the active-source data. I then compute a Wiener shaping filter that shapes the vertical-component reflection to the reflection recorded by the hydrophone within the picked window. This particular filter incorporates the density and slowness factors in Equations 4.5 and 4.6.

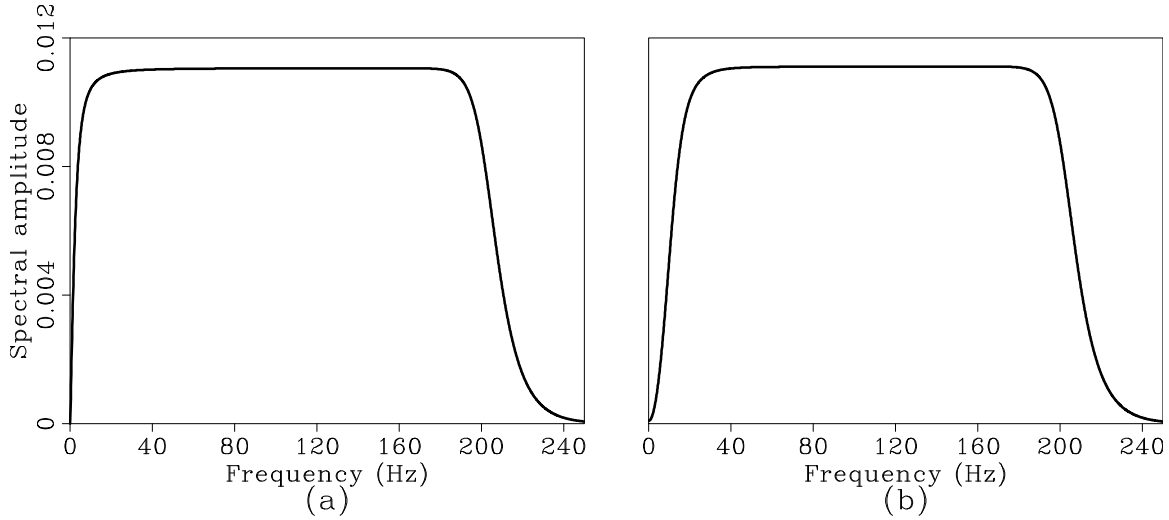

Figure 4.18: Amplitude spectrum of instrument response. (a) Hydrophone. (b) Vertical-component geophones. [**CR**] chap4/. a-response

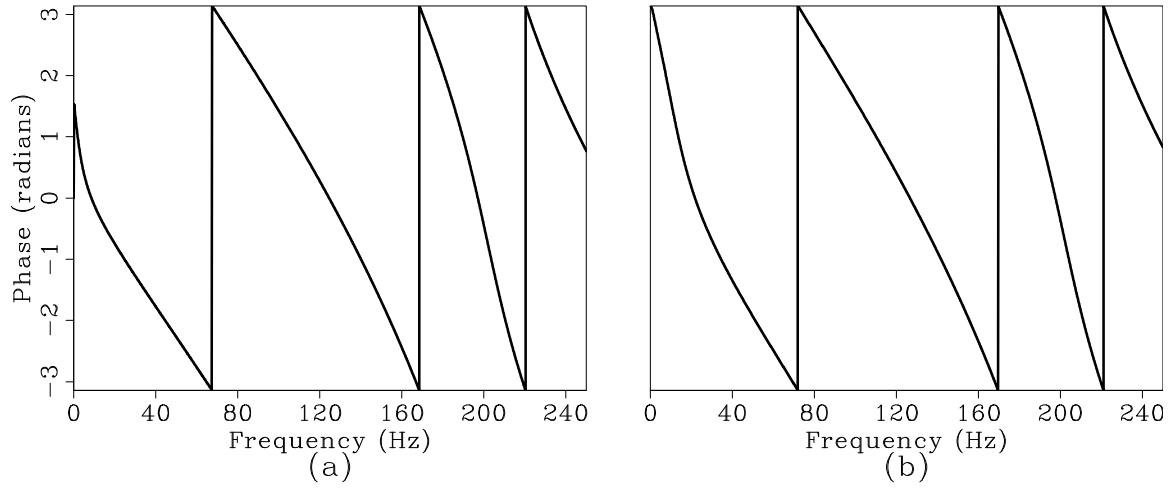

Figure 4.19: Phase spectrum of instrument response. (a) Hydrophone. (b) Vertical-component geophones. [**CR**] chap4/. p-response

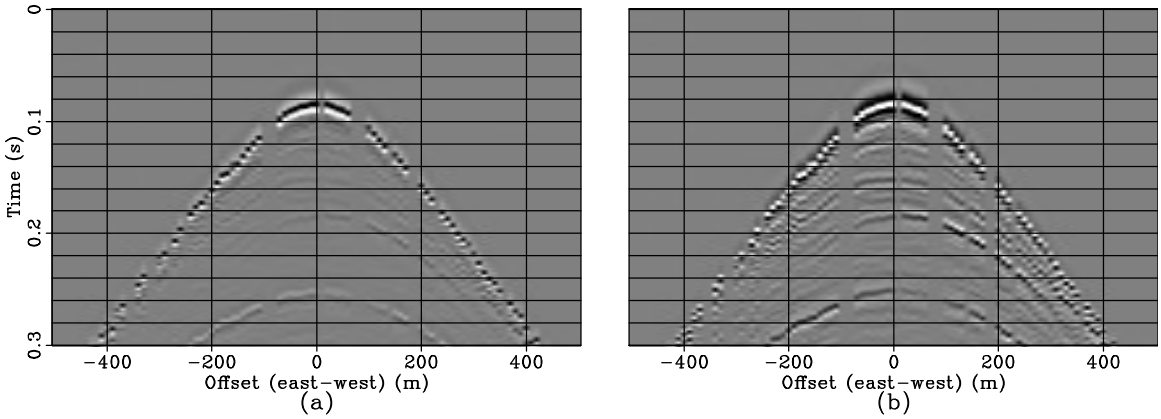

Figure 4.20: Receiver gathers corresponding to those in Figure 4.17 after removing the instrument response. (a) Hydrophone. (b) Vertical-component geophones. [**CR**] chap4/. forties-desig-gather

Once the calibration filter is estimated for each node, I test it by plugging it into Equations 4.5 and 4.6 to perform PZ summation on the active data. Although the calibration coefficient is estimated at only zero offset, I use it for all traces regardless of offset for display purposes. The result of the separation is shown in Figure 4.21. Again, these gathers have been bandpassed for frequencies between $40 - 200$ Hz. As hoped, the receiver gather for the up-going wavefield contains primarily the reflections, and the water-column multiple is also significantly weaker (Figure 4.21a). However, the direct arrival is still clear, although it appears weaker. As for the receiver gather for the down-going wavefield, the reflection events have nearly disappeared while the direct wave and water-column multiple are quite clear (Figure 4.21b), which is expected. Though not perfect, the wavefield separation results seem reasonable here. This method of estimating calibration coefficients is repeated for a select number of nodes.

Cross-correlation of up- and down-going noise

With reasonable calibration coefficients between the hydrophone and vertical-geophone recordings from active-seismic data, I apply the up-down separation procedure to the same 30-minute time windows used for seismic interferometry in the previous section. As with the active-source data, I first remove the instrument responses from the passive recordings. I then bandpass the recordings for frequencies between

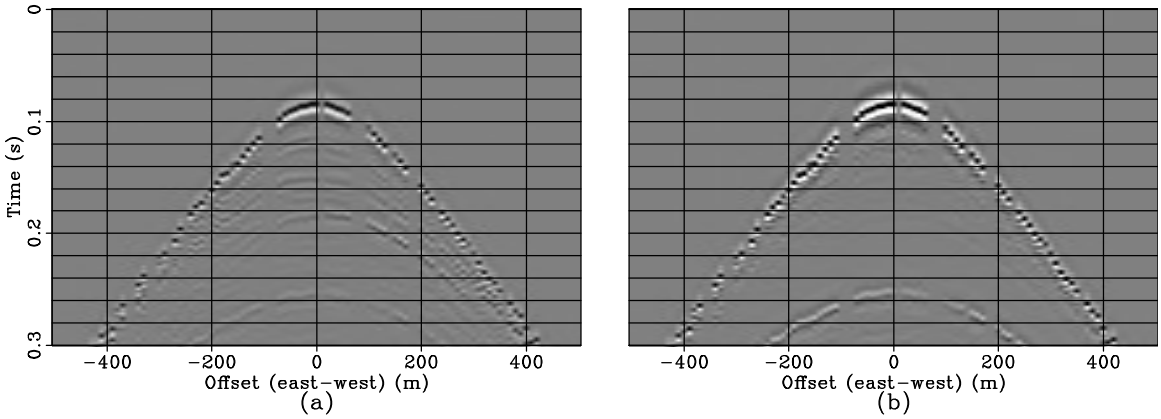

Figure 4.21: Receiver gathers corresponding to those in Figure 4.20 after PZ summation. (a) Up-going wavefield. (b) Down-going wavefield. [**CR**] chap4/. forties-pz

$40-200$ Hz before performing PZ summation on the passive seismic recordings using the corresponding calibration coefficient for each node estimated from the active data (Equations 4.5 and 4.6). Finally, I cross-correlate the resulting up- and down-going wavefields from each time window in the frequency domain using:

$$F(\omega) = D(\omega)U^*(\omega), \tag{4.7}$$

where F is the fathometer output, D is the down-going wavefield, and U is the up-going wavefield. I do not perform cross-coherence here (like for passive seismic interferometry) because I do not want the amplitude effects from removing the instrument response and applying PZ summation to be discarded by spectral whitening.

1D profiles

Figure 4.22 shows the results of cross-correlating up- and down-going passive energy recorded by four random nodes at Forties after linear stacking the result from each 30-min time window. These results are estimated 1D profiles of the subsurface. I scale the amplitudes along the time axis by $t^{0.8}$ to enhance later arrivals and plot the envelopes of the signals for easier interpretation. Aside from the peaks at 0 s, there appears to be peaks around 0.16 s at each of the nodes. As discussed previously, the water depth in this area is approximately 120 m. Assuming a water velocity of 1500 m/s, the water-column multiple would take about 0.16 s to travel up and down.

Additionally, there appears to consistently be an event between 0.30 and 0.32 s, which could be related to the second water-column multiple (two trips up and down).

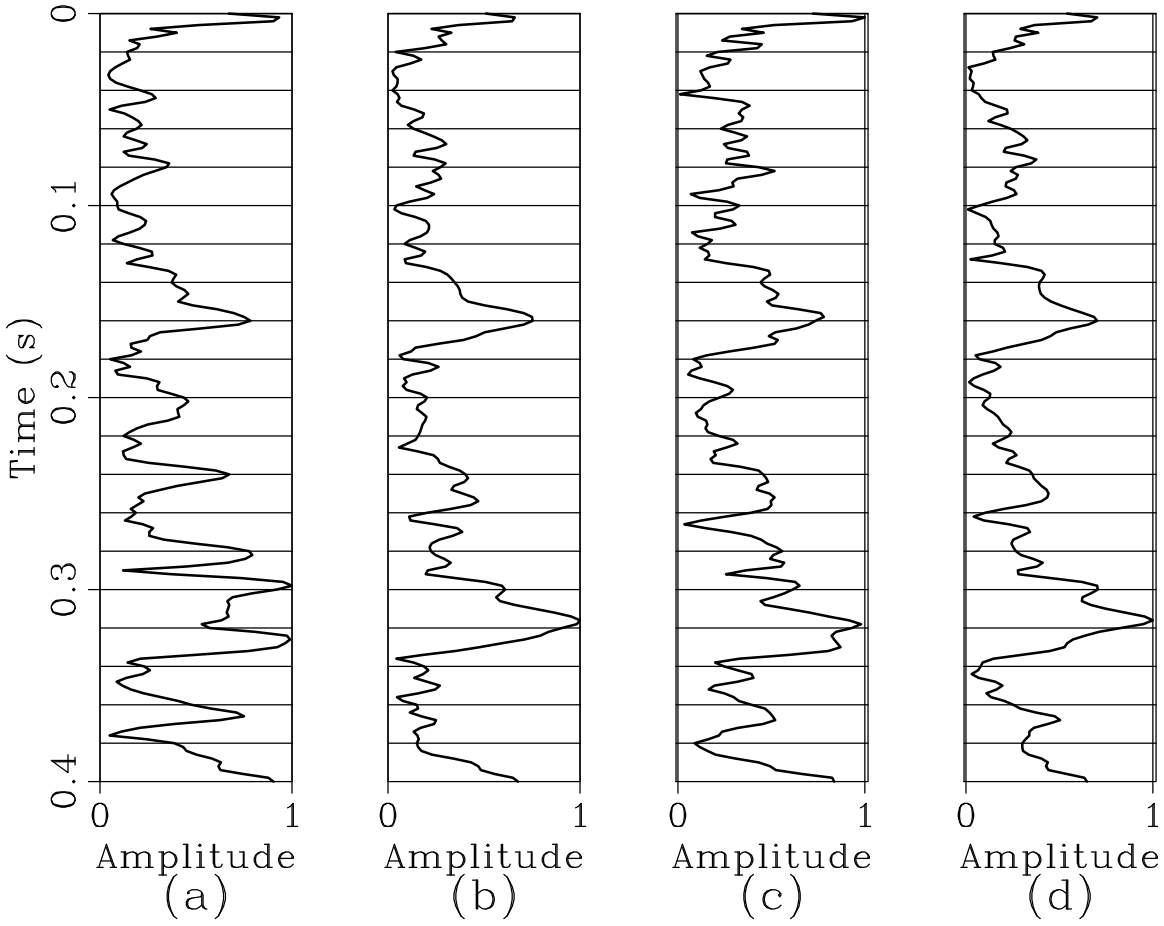

Figure 4.22: Envelopes of passive fathometry results at four different nodes in the $40 - 200$ Hz frequency band after linear stacking of results from all 30-min time windows. Amplitudes are scaled by time. [**CR**] chap4/. fathometer-linear-all

Based on the performance of phase-weighted stacking in the previous section, Figure 4.23 shows the results for the same four nodes using phase-weighted stacking rather than linear stacking. There are a number of observations to make. First, it is clear that the fathometry results are much less noisy now. Second, the peaks around 0.16 s and between 0.30 and 0.32 s are more apparent now that the noise has decreased. Again, these events are likely to be related to water-column multiples given the water depth at Forties and average water velocity. Third, and most interesting, is the emergence of peaks besides those related to the water column. In particular, there appear to be peaks at approximately 0.08 s and 0.25 s in each of the profiles.

As with the virtual source gathers in the previous section, I also display the

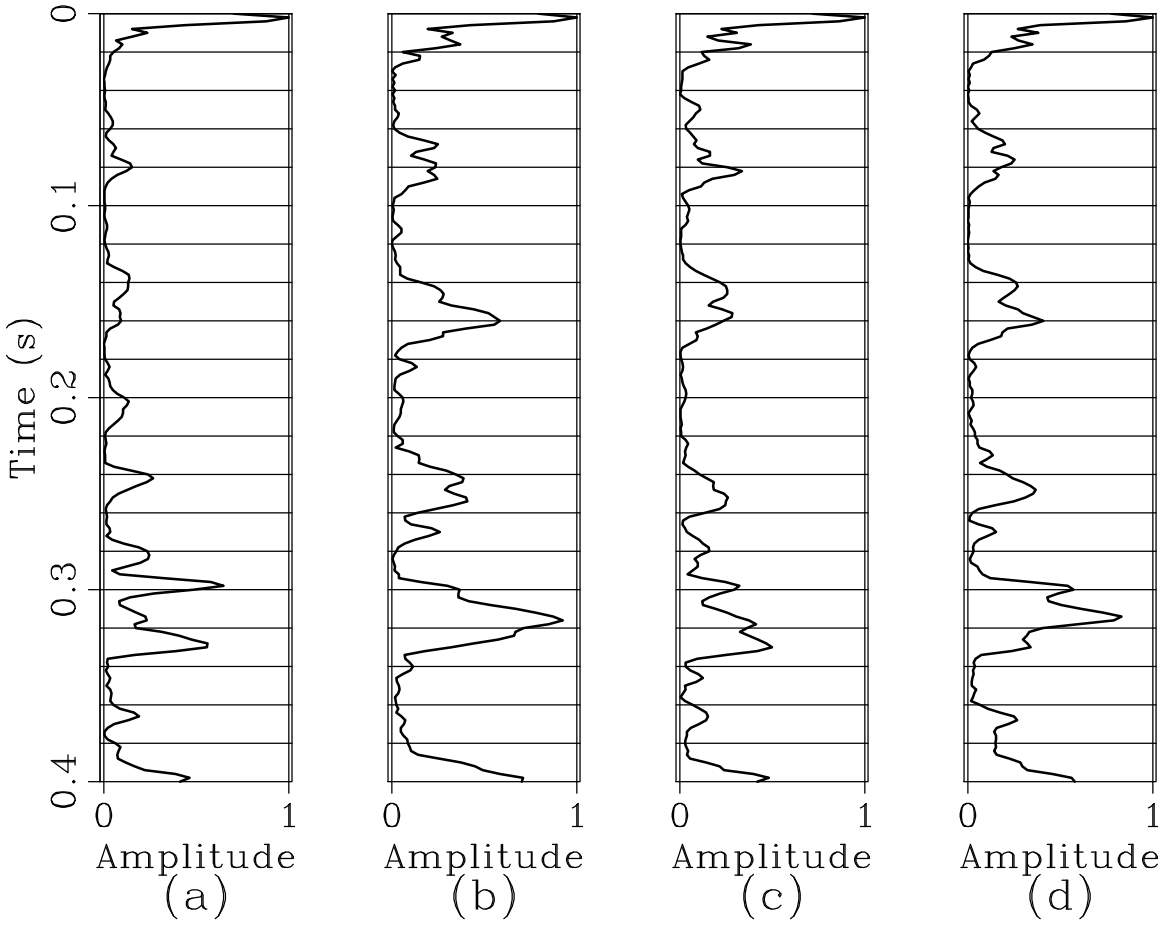

Figure 4.23: Envelopes of passive fathometry results at four different nodes in the $40 - 200$ Hz frequency band after phase-weighted stacking of results from all 30-min time windows. Amplitudes are scaled by time. [**CR**] chap4/. fathometer-pws-all

fathometry results for two of the nodes (Figures 4.23a and 4.23b) that have been phase-weighted stacked over four different time periods: all times, period T1, period T2, and period T3. Each panel has an amplitude gain scaled by time to enhance later events. Looking at the first node (Figure 4.24), it appears that different time periods contribute to different peaks in the final fathometry result. Unfortunately, there is no arrival that is clearly consistent over time. This is also the case for the second node (Figure 4.25). Furthermore, there is hardly any consistent arrivals between different nodes for a given time period. The exception is the sharp peaks at 0.16 and 0.32 s during stormy weather (period T1).

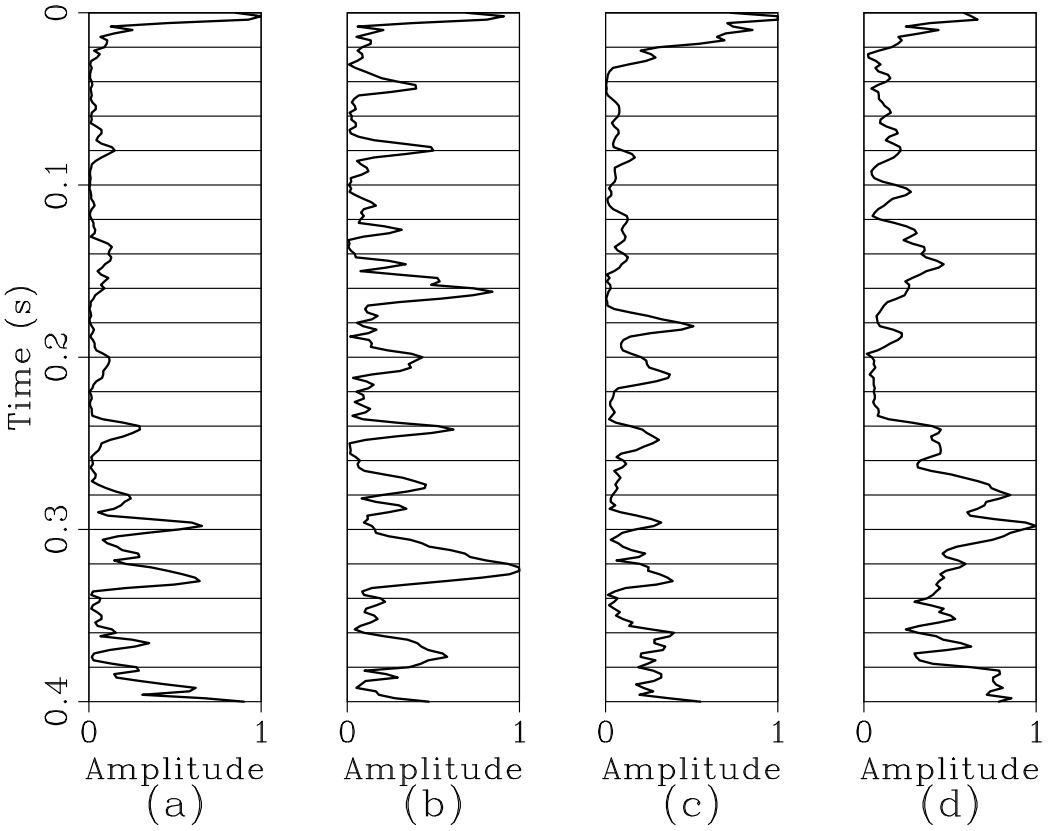

Figure 4.24: Envelopes of passive fathometry results corresponding the to the node in Figure 4.23a, phase-weighted stacked over (a) all times, (b) period T1, (c) period T2, and (d) period T3. Amplitudes are scaled by time. [**CR**] chap4/. fathometer-00-pws-all-quiet

To help determine what the peaks in the fathometry results correspond to, I return to the active-source data. Figure 4.26 displays four near-zero offset hydrophone traces bandpassed for frequencies between $40 - 200$ Hz for the nodes corresponding to the 1D profiles in Figures 4.22 and 4.23. Though performing normal moveout on

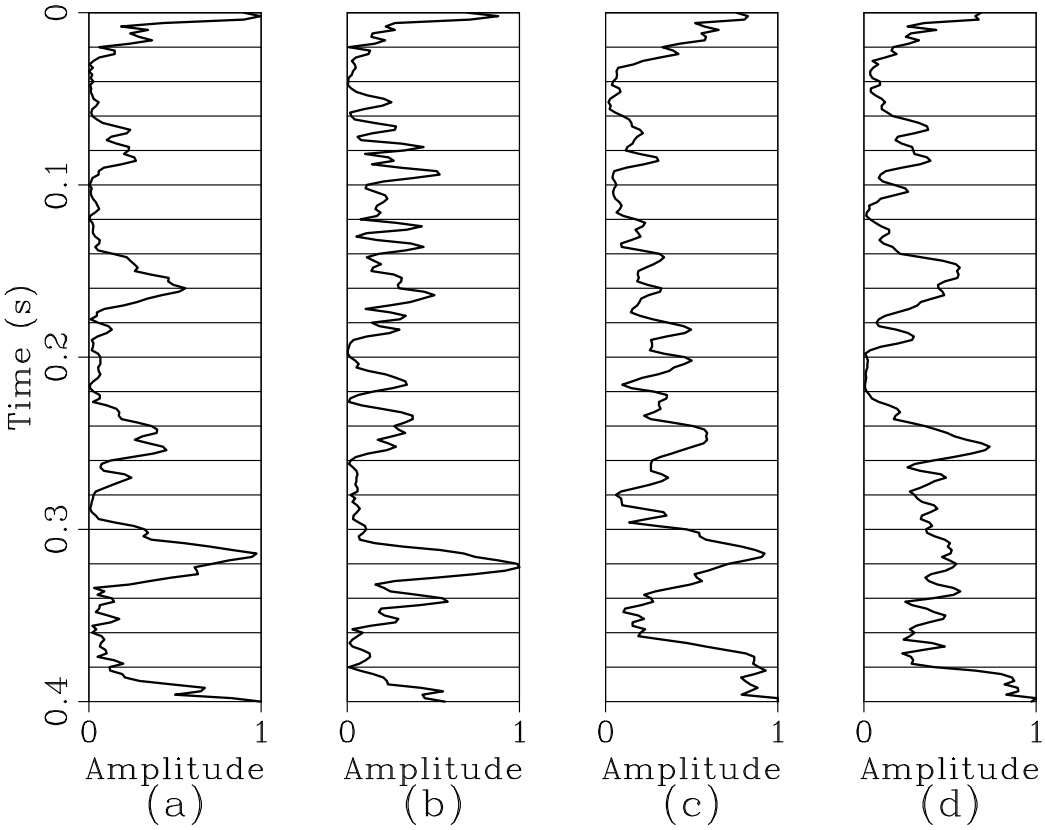

Figure 4.25: Envelopes of passive fathometry results corresponding the to the node in Figure 4.23b, phase-weighted stacked over (a) all times, (b) period T1, (c) period T2, and (d) period T3. Amplitudes are scaled by time. [**CR**] chap4/. fathometer-01-pws-all-quiet

a common-midpoint gather centered at the node locations would yield traces with higher signal-to-noise ratio, the acquisition geometry (particularly the limited range of the node array) of the active survey does not allow for long-offset traces when sorting the data into common midpoints. Like the fathometry results, I bandpass the traces for frequencies between $40 - 200$ Hz and plot their envelopes.

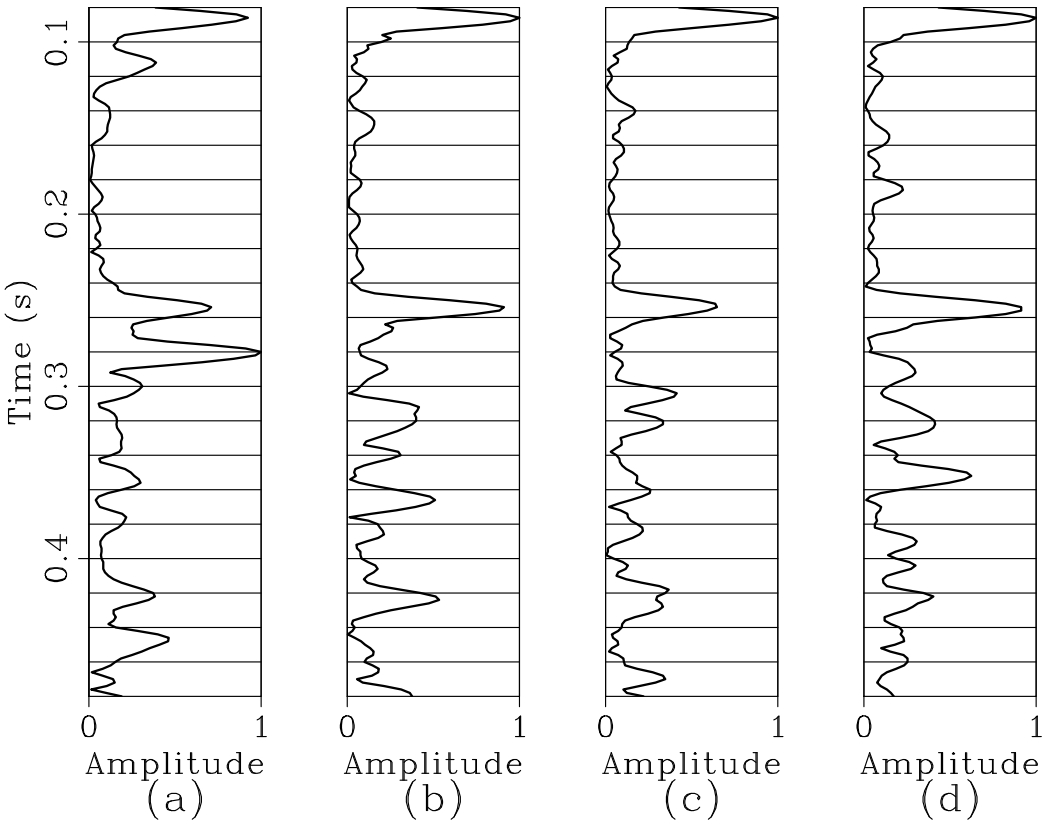

Figure 4.26: Near-zero offset hydrophone traces corresponding to the fathometry results in Figures 4.22 and 4.23. An amplitude gain scaled by time and a time shift have been applied for comparison to fathometry results. [**CR**] chap4/. zero-all

From these zero-offset gathers, there are two clear arrivals in each of the gathers. Note that their arrival times are similar across all four displayed nodes. The first is at approximately 0.9 s, which corresponds to the direct arrival. The second is at approximately 0.25 s, which is 0.16 s after the direct arrival. Given the water bottom is approximately 120 m depth, the two-way traveltime of a wave through the water column is 0.16 s. Thus, this second strong arrival is the water-column multiple. Additionally, there appear to be some reflection events between these two dominant arrivals that range between $0.14 - 0.16$ s (or $0.05 - 0.07$ s after the direct arrival).

DISCUSSION

Based on the arrival times of events in the active-source traces, passive fathometry appears to be potentially extracting the water column multiples. In the active-source data, the first multiple arrives 0.16 s after the the direct arrival across all displayed nodes, and in the fathometry results, there are strong peaks at 0.16 s across all nodes (even those not shown here). Additionally, based on the known two-way traveltime through the water column, the event at 0.32 s in the fathometry results are potentially related to the second water-column multiple.

While the fathometry results also reveal arrivals at 0.08 and 0.25 s, they do not appear to correspond to the shallow reflections in the active data. The reflections in the active data arrive between $0.05 - 0.07$ s after the direct arrival, which are later than the previously mentioned arrivals in in the fathometry results. Additionally, these arrival times in the fathometry results are consistent across all nodes, whereas the reflection arrival times vary slightly from node to node.

Although the fathometry results display peaks at the expected water-column multiple arrival times, the regularity of the arrivals in the fathometry results (every 0.08 s) is important to note. Such a regular pattern indicates that there is a periodic pattern in the recorded passive seismic data. These are unlikely to be related to instrument spikes, as there is no comb pattern at 12.5 Hz intervals in the spectrograms (Figure 4.5). Additionally, these are unlikely to be generated by a continuous but weak active source, as the regular arrivals in the fathometry results are not overwhelmingly clear across different all time periods (Figures 4.24 and 4.25). While these regular arrivals (including the water-column multiples) are potentially artifacts from acquisition or processing, it is interesting to note that the time between each arrival is approximately the one-way traveltime through the water column.

It is also interesting to note that period T1 (the stormy period) displays high frequency signal not observed in the other time periods. This time period also displays the strongest arrivals at 0.16 and 0.32 s, which are the expected traveltimes of water-column multiples. Together, these results suggest that it may be possible that stormy weather does produce strong high-frequency, vertically propagating energy to extract. Therefore, fathometry results during stormy periods may be the most reliable.

The question remains whether the fathometry results offer an improvement over

a simple autocorrelation. To compare, I display the autocorrelations of both the hydrophones (Figure 4.27) and vertical geophones (Figure 4.28) for the same four nodes shown in the fathometry results. Like the fathometry processing, I removed the instrument responses and frequency bandpassed the traces prior to autocorrelation. The autocorrelation of the hydrophone is nearly identical to the fathometry results, and the autocorrelation of the vertical geophone produces similar but noisier results. Thus, regardless of which method is used, it appears that the same events at 0.08 s intervals are observed.

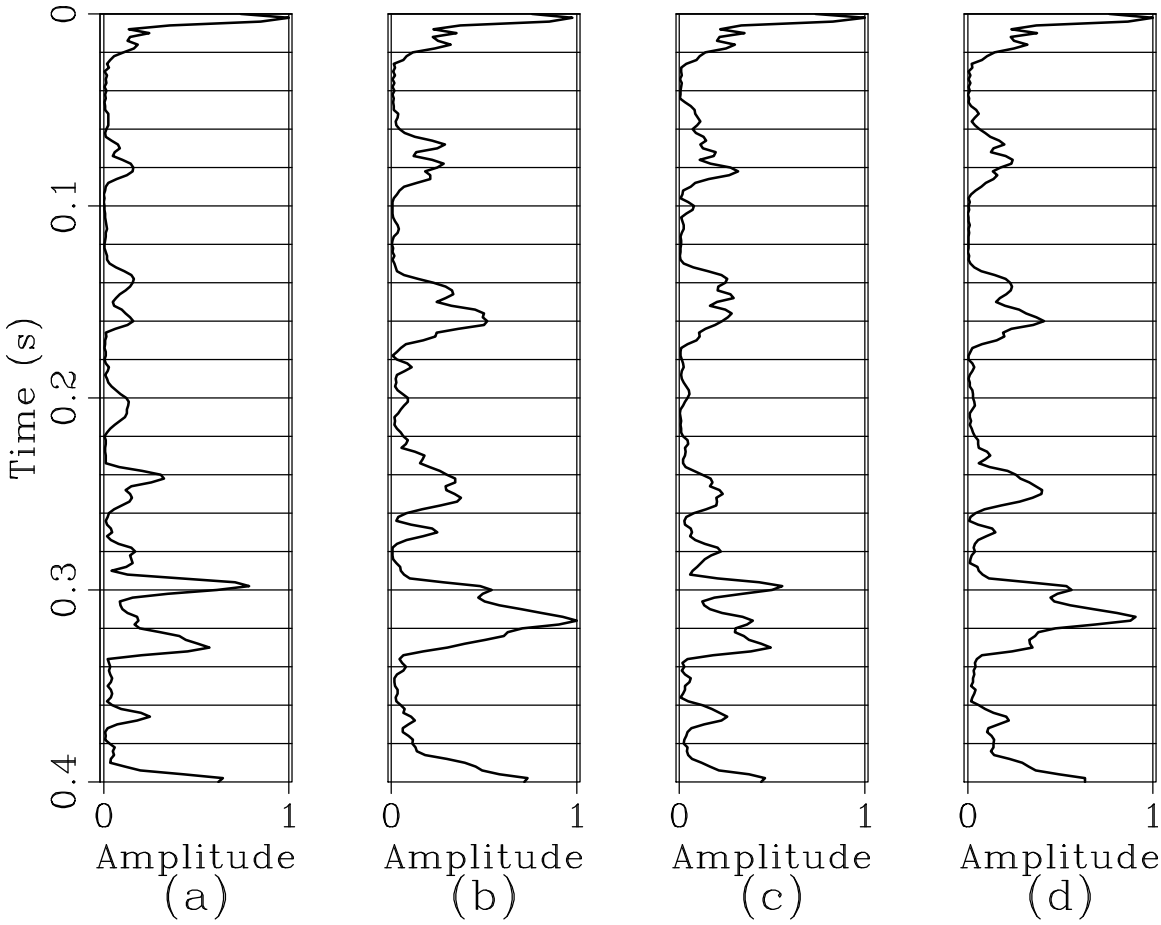

Figure 4.27: Autocorrelation of hydrophone recordings from corresponding nodes in Figures 4.22 and 4.23. Amplitudes are scaled with time. [**CR**] chap4/. autoH-pws-all

Clearly, passive fathometry and the corresponding up-down separation of passive energy did not prove to be worth the effort, as similar results could be obtained through a cheaper autocorrelation procedure. The assumption that the majority of the energy arrives at near-vertical incidence is likely too large of an assumption, given that many PP virtual source gathers displayed not only strong platform-generated

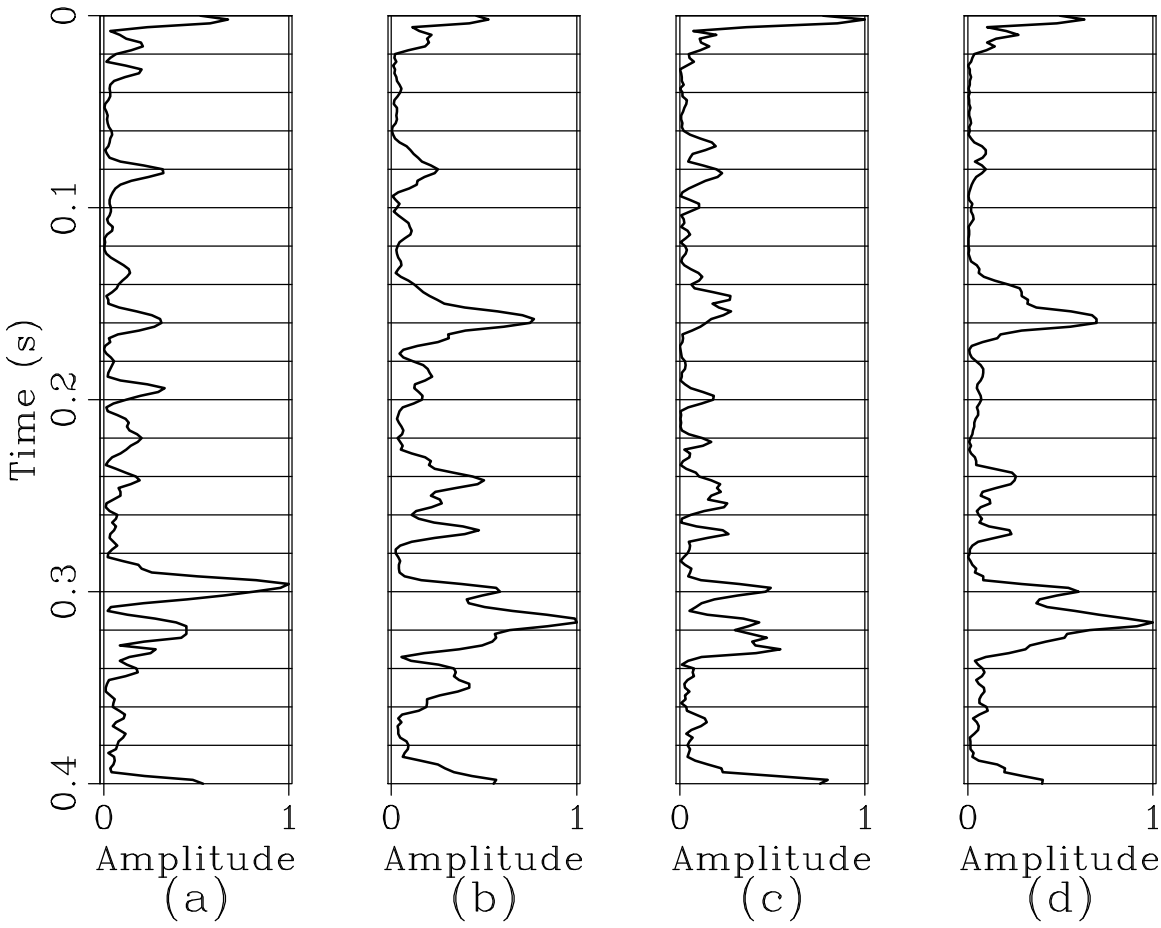

Figure 4.28: Autocorrelation of vertical-geophone recordings from corresponding nodes in Figures 4.22 and 4.23. Amplitudes are scaled with time. [**CR**] chap4/. autoV-pws-all

noise but also strong events propagating at water velocity at near-horizontal angles. These horizontally propagating events interfere with the desired signal that up-down separation tries to enhance, and thus likely corrupted the fathometry results. It is clear that applying PZ summation to passive seismic data is not enough to extract reflections from noise.

The success of passive fathometry using a vertically-aligned array is based on up-down wavefield separation via beamforming. The stacking power of the array allows for multiple signals to be combined into up- and down-going signals with high signal-to-noise ratios. These clean signals are then cross-correlated to obtain a reflection profile below the vertical array. With an OBN array, nodes are typically spaced too far apart for their traces to be combined. However, if nodes are close enough to each other, it may be possible to average their hydrophone and vertical-geophone recordings to enhance normally propagating energy while dampening horizontally-propagating energy. PZ summation could then be applied to separate the beamformer outputs into up- and down-going wavefields to be cross-correlated. Additionally, it could be beneficial to record data at over 500 Hz, as energy from breaking waves at the sea surface typically dominate the ambient seismic noise field between $500 - 5000$ Hz (Hildebrand, 2009). Such high investigation frequencies would allow interfering signal from platform energy and distant seismic shooting to be avoided in the analysis.

CONCLUSIONS

I investigated the apparent P-waves in the ambient seismic noise recordings from Apache Forties using seismic interferometry and passive fathometry processing. By using a phase-weighted stack in the seismic interferometry workflow, I showed that there are three apparent P-wave events in the hydrophone-hydrophone (PP) and vertical-vertical (ZZ) geophone correlations. I used virtual source gathers with approximate lines of receivers to determine the velocity and directionality of these events. One event travels at 1500 m/s and appeared to travel across the array along different azimuths over time. Because it is most apparent in the PP correlations, I hypothesized that this event was a horizontally-propagating event likely originating from distant sources such as another active seismic survey or shipping noise. Another event traveled at an apparent velocity of approximately 3000 m/s with 0 s intercept time and appeared in the virtual source gathers from both components. The last

event also traveled at an apparent velocity of approximately 3000 m/s but with 0.15 s intercept time, and appeared in only the ZZ correlations. I hypothesized that the origin of these events was the platform, and that they were likely P-wave reverberations in the water column.

Given this interpretation of the faster events, I performed passive fathometry processing on the ambient noise in an attempt to harness vertically propagating energy for extracting subsurface reflections. While there were arrivals at the expected two-way traveltimes through the water column, there were also consistent arrivals at the one-way traveltimes through the water column across all nodes. Comparison of the fathometry results to active-source data suggested that these arrivals between the two-way traveltimes were unlikely to be related to subsurface stratigraphy. Instead, the regularity and timing of arrivals suggests that they are artifacts, potentially in the acquisition or the processing. Additionally, it appears that passive fathometry did not add much value over simple autocorrelation, most likely because the assumption of vertically-propagating energy is violated at Forties. Regardless of the success of passive fathometry processing, it appeared that the water depth could potentially be extracted in a shallow marine environment from the ambient seismic noise field, particularly during stormy weather.

ACKNOWLEDGMENTS

I would like to thank Apache North Sea Limited for access to the data set and permission to publish.

Chapter 5

Body-wave extraction in a deep-water environment

Though the microseism band of Earth's ambient seismic noise field is primarily composed of surface waves, it can also contain body waves. In this chapter, I perform multi-component seismic interferometry on passive seismic data from the Moere Vest long-offset ocean-bottom node survey to extract three distinct wave modes: Scholte waves, guided acoustic waves, and critical refractions. While Scholte waves are common, the latter two wave modes are not. The dispersive behavior of the acoustic guided waves compares well with theoretical dispersion curves, while the arrival times of the critical refractions compare well with those in the active seismic survey. Numerical modeling of wave propagation through a simplified elastic model of Moere Vest suggests that these critical refractions could result from Scholte waves interacting with the horst-and-graben structure of the top of basalt. Overall, the results from this chapter lay the foundation for passive subsurface imaging using wave modes beyond surface waves.

INTRODUCTION

The application of seismic interferometry to recordings of Earth's ambient seismic noise field has been shown to successfully estimate the Green's function between pairs of receivers. While extraction of the surface-wave portion of the estimated Green's function has been successful across many spatial scales in both land and marine

environments (e.g., Shapiro et al., 2005; Bensen et al., 2008; de Ridder and Dellinger, 2011), there have been far fewer studies that have successfully extracted non-surface-wave modes. In onshore environments, Roux et al. (2005) and Gerstoft et al. (2008c) retrieved diving P-waves at the regional scale. Additionally, Poli et al. (2012) retrieved P-wave reflections off the mantle transition zone, while Ruigrok et al. (2011) and Zhan et al. (2010) retrieved P- and S-wave reflections off the Moho, respectively. In these studies, the body-wave energy was extracted from the microseism band. At the exploration scale, Nakata et al. (2015) were able to extract diving P-waves from a dense array at Long Beach, California, while Nakata et al. (2011) and Draganov et al. (2013) were able to extract reflection events in separate locations. In shallow marine environments, studies have been able to extract direct P-waves traveling in the water column (e.g., Mordret et al., 2013), as well as sea-surface reflected and sea-bottom reflected events (e.g., Brooks and Gerstoft, 2009).

In this chapter, I focus on extracting both surface waves and non-surface waves from the ambient seismic noise field recorded by the Moere Vest deep-water ocean-bottom node (OBN) array. I begin with an overview of the unique Moere Vest OBN array. I then provide an overview of passive seismic interferometry and apply it to passive seismic data below 2 Hz. The resulting virtual source gathers reveal three distinct wave modes:

- Scholte waves, which are commonly observed in ambient noise studies using OBN data;
- guided acoustic waves, which have previously only been observed at these water depths and frequencies in Hatchell and Mehta (2010); and
- critical refractions off a subsurface structure, which have previously never been observed in passive seismic data.

Because of the rarity of two of these wave modes in passive seismic studies, I outline evidence supporting each of these classifications. I then simulate wave propagation through a simple elastic model to test a hypothesis for the natural generation of critical refractions.

MOERE VEST CONTINUOUS RECORDINGS

The Moere Vest data set, provided by Seabed Geosolutions, consists of 179 four-component ocean-bottom nodes (OBNs) deployed along a line on the seabed of offshore Norway and above a known block of basalt (Figure 5.1). The array is notable for its spatial extent (85 km maximum offset between nodes) and deep-water environment (approximately $1.6 - 1.9$ km depth). The nodes consist of three different sub-geometries: 141 nodes spaced 250 m apart and spanning 35 km that form the regular spread; 12 nodes spaced 5 km apart at each end of the regular spread to increase the total length of the array to 85 km; and 26 nodes spaced 2 m apart in two parallel lines along the regular spread. Each node records continuously at 2-ms sampling for approximately 10 days, with all nodes simultaneously recording for 7 of those days.

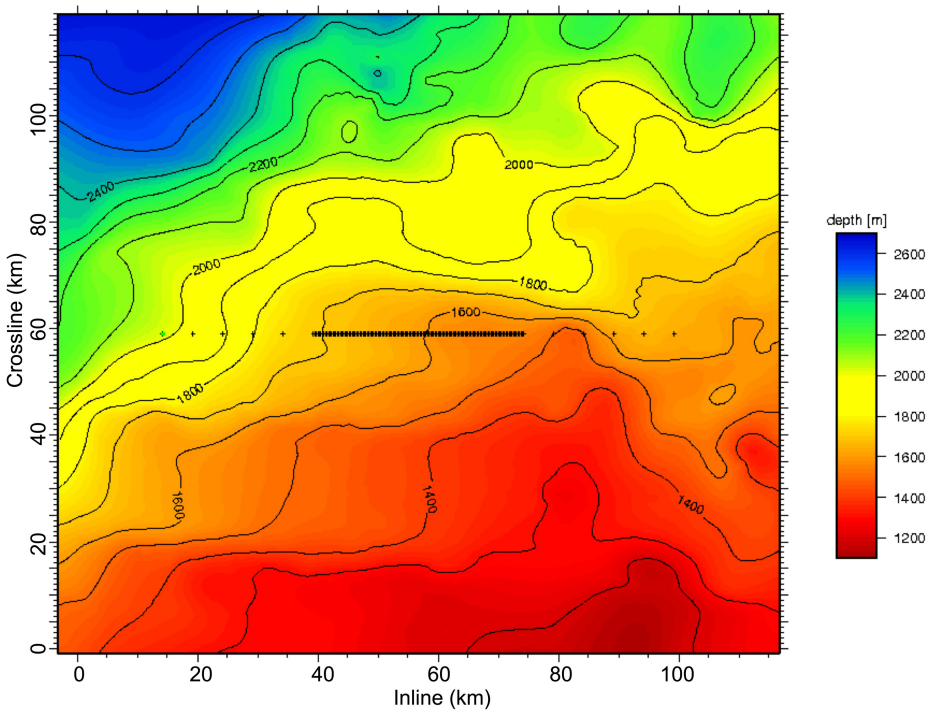

Figure 5.1: Map of the Moere Vest OBN array with bathymetry. Nodes at both ends of the dense regular spread are used for spectrograms and virtual source locations. [**NR**] chap5/. moerevest-map

To prepare the data for a passive seismic study, I first rotate the horizontal-component recordings of each geophone such that one component is inline with the

OBN array and the other component is orthogonal to the array using the method from Alves (2017). Because the shot and receiver lines overlap, the method effectively finds the rotation angle at which the first break energy is maximized in the radial component. I then taper each recording to the nearest hour and then divide the results into two-hour windows with 50% overlap (Seats et al., 2012).

Within the 7 days of simultaneous recordings were periods of active seismic shooting, where seismic shots occurred at 100 m intervals along a line over the node array. This is apparent in the log-spectrogram of both the hydrophone and vertical-geophone recordings for the node on the western edge of the regular spread, where the spectral comb signature of active sources is dominant above 2 Hz (Figure 5.2). Note that the comb pattern above 2 Hz is due to regular seismic shot intervals. While the effect of active seismic shooting does not appear to interfere with the frequencies of interest in this study (below 2 Hz), I remove them from further analysis to ensure that the results shown here are derived from strictly passive seismic data. Removal of times of active seismic surveys results in approximately 3 days of simultaneous passive recordings, or 78 two-hour time windows.

From the remaining time windows, it appears that energy below 2 Hz becomes stronger between periods of active seismic shooting. This spectral trend might be indicative of stormy conditions, which are known to induce stronger microseisms (Gerstoft et al., 2008c). A storm during this time would also explain why active seismic shooting was halted. Thus, the conditions during this survey provide an opportunity to extract body waves from the ambient seismic noise field.

PASSIVE SEISMIC INTERFEROMETRY

Passive seismic interferometry produces an estimate of the Green's function between two receivers by cross-correlating their continuous and simultaneous recordings of the ambient seismic noise field (Wapenaar et al., 2010). To perform passive seismic interferometry I calculate the average of the whitened coherency between each pair of nodes across all time windows. This procedure is also referred to as calculating the cross-coherence, and it typically produces a broader-band signal than standard cross-correlation while maintaining phase information. In the frequency domain, the

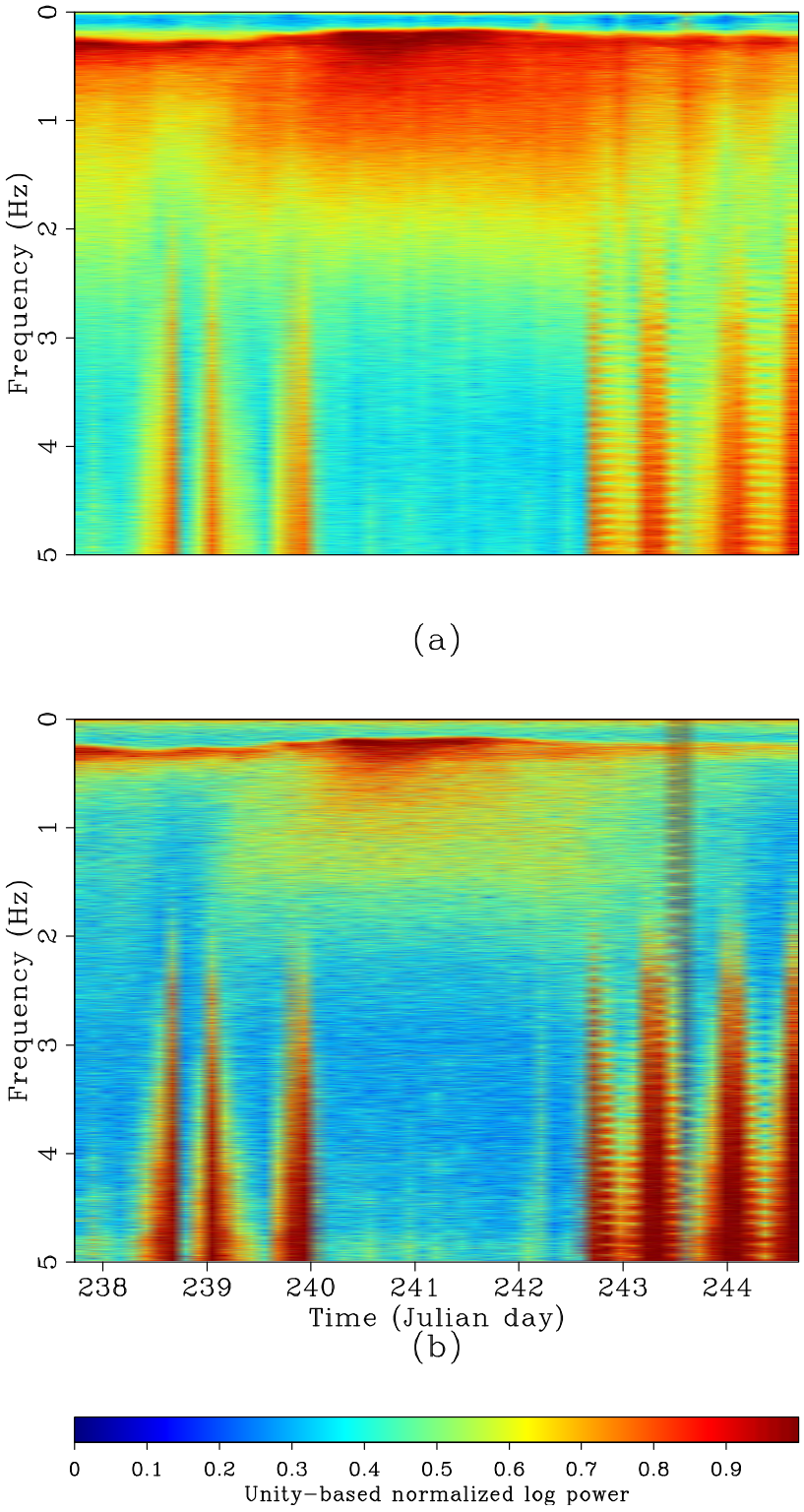

Figure 5.2: Spectrograms of data recorded by the western node of the primarily array. (a) Hydrophone. (b) Vertical geophone. [**CR**] chap5/. moerevest-sp-lo

procedure is generally expressed as:

$$[G(x_B, x_A, \omega) + G^*(x_B, x_A, \omega)] = \left\langle \left(\frac{U(x_B, \omega)}{\{|U(x_B, \omega)|\}} \right) \left(\frac{U^*(x_A, \omega)}{\{|U(x_A, \omega)|\}} \right) \right\rangle, \qquad (5.1)$$

where G is the Green's function between two receiver locations (x_A, x_B), $U(x, \omega)$ is the Fourier transform of the wavefield at a given receiver location x, $*$ is the complex conjugate, $\langle \cdot \rangle$ is an averaging operation, $|\cdot|$ is the magnitude of the spectrum, and $\{\cdot\}$ is a 0.003 Hz running window average used for normalizing the signal. In total, nearly 2.5 million cross-coherences are calculated (78 time windows $\times$ 179^2 node pairs).

By cross-correlating the recording from one node with recordings from all other nodes, I can create a virtual source gather at any node in the array. As a result, I can create an entire virtual seismic survey with virtual sources at each node location. For this study, I focus on correlations from the hydrophones as well as from the vertical and radial components of the geophones. I include the radial component here in hopes of detecting any shear-wave energy. Because the Moere Vest array is such a wide-aperture and deep array, I only investigate frequencies below 2 Hz, which is dominated by strong microseism energy. Any extracted signal at high frequencies is likely to be anthropogenic in origin, and any hidden, naturally occurring signal at high frequencies is likely to be heavily attenuated at these large spatial scales.

WAVES MODES IN VIRTUAL SOURCE GATHERS

Virtual source gathers derived from passive seismic data recorded at Moere Vest reveal three different wave modes: Scholte waves, guided acoustic waves, and critical refractions. I outline evidence for each of these classifications in the following subsections.

Scholte waves

Scholte waves are surface waves that travel along fluid-solid interfaces. Their particle motion is elliptical along the direction of propagation, much like Rayleigh waves. Figures 5.3 and 5.4 show hydrophone-hydrophone (PP) and vertical-vertical geophone (ZZ) virtual source gathers, respectively, for frequencies between $0.2 - 0.4$ Hz for two virtual source locations: one at the western edge of the regular spread and one at the

eastern edge of the regular spread (red dots in Figure 5.1). The slow event propagating in each gather at a group velocity of approximately 450 m/s appears to be a Scholte wave for a number of reasons.

First, this event is much stronger in the ZZ virtual source gathers (Figure 5.4) than in the PP virtual source gathers (Figure 5.3). Since geophones are coupled to the ground while hydrophones are coupled to the water, one would expect any Scholte wave propagating along the seabed to be stronger in ZZ correlations than in PP correlations. The stronger, faster-propagating event in the PP correlations is likely an acoustic guided wave (analyzed in the following subsection). Second, surface waves typically dominate Earth's ambient seismic noise field at these very low frequencies (microseism band). As a result Scholte waves are commonly the dominant arrival in passive seismic data collected at the ocean bottom (e.g., Mordret et al., 2013; de Ridder and Biondi, 2015). Third, Scholte waves are commonly observed to propagate at velocities on the order of a few 100s m/s (e.g., de Ridder and Dellinger, 2011; de Ridder et al., 2015), which is on the order of the group velocities estimated here.

Another common characteristic of Scholte waves is that they are dispersive. Because velocity of wave propagation through the subsurface increases with depth, and because surface waves typically sample shallower depths as frequency increases (shorter wavelengths), Scholte waves commonly display decreasing velocities as frequency increases. Here, I create a dispersion image by performing slant stacks over ranges of intercept times and moveout velocities on a virtual source gather, and then performing a Fourier transform along the time axis to produce an image in the frequency-velocity domain. The dispersion image associated with the ZZ virtual source gather in Figure 5.4a, which displayed strong Scholte-wave energy, is shown in Figure 5.5. As expected, the phase velocity appears to decrease as frequency increases. Given this dispersion image, it appears that the wavelengths vary approximately between 1250 m at 0.4 Hz and 3000 m at 0.2 Hz, which are long enough to potentially reach the top of basalt approximately 1 km below the sea bottom when assuming that surface waves are sensitive to depths approximately one-third of their wavelengths (Forsyth et al., 1998).

The previously outlined evidence suggests that these low-velocity, low-frequency events are Scholte waves. From the ZZ virtual source gathers (Figure 5.4), it is clear

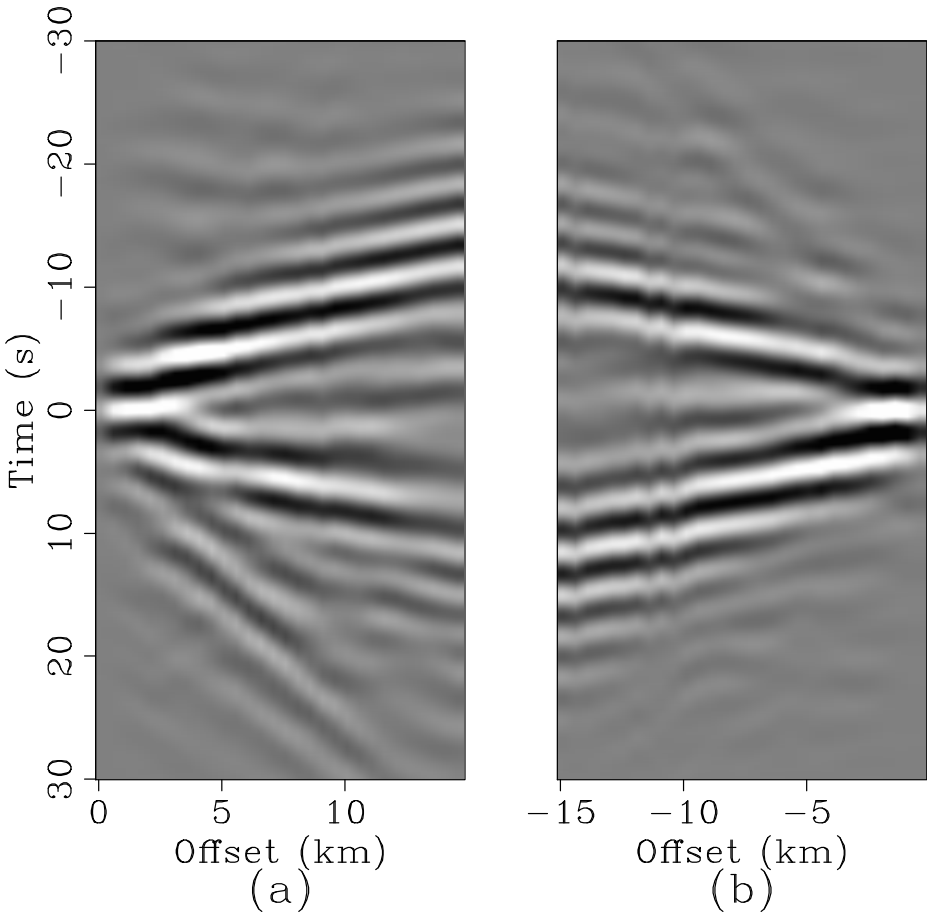

Figure 5.3: PP virtual source gathers for frequencies between $0.2 - 0.4$ Hz for two different virtual source locations. (a) Western node of the main array. (b) Eastern node of the main array. Positive offsets are toward the east while negative offsets are toward the west. The faint events propagating at approximately 450 m/s are Scholte waves, while the strong events propagating at 1500 m/s are likely acoustic guided waves. [**CR**] chap5/. scholte-hh-end

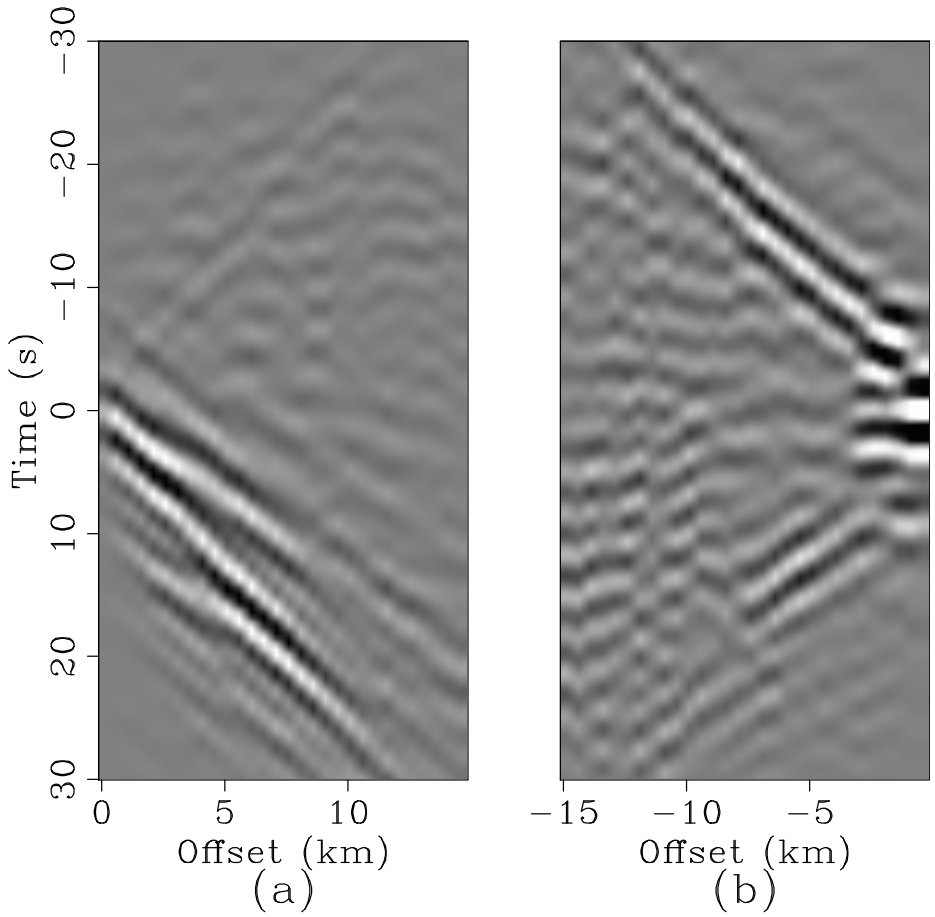

Figure 5.4: ZZ virtual source gathers for frequencies between $0.2 - 0.4$ Hz for two different virtual source locations. (a) Western node of the main array. (b) Eastern node of the main array. Positive offsets are toward the east while negative offsets are toward the west. The strong events propagating at approximately 450 m/s are Scholte waves. [**CR**] chap5/. scholte-zz-end

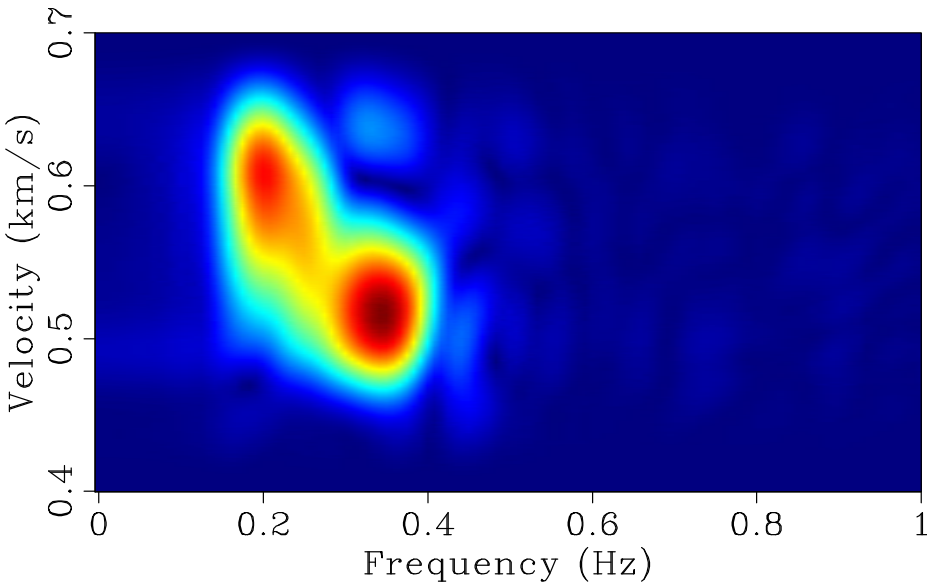

Figure 5.5: Scholte wave dispersion image for the virtual source gather centered at the western node for the ZZ virtual source gather (Figure 5.4a). Warmer colors correspond to greater coherence of the dispersion estimate. [**CR**] chap5/. dispersion-scholte

that the Scholte-wave energy is strongest at positive time lags when the virtual source is in the west of the array and at negative time lags when the virtual source is in the east of the array. This indicates that the Scholte-wave energy is propagating primarily from west to east, which suggests that this particular energy is arriving from open North Sea waters rather than from the Norwegian coastline. These Scholte waves and their corresponding dispersion images can potentially be used to estimate 1D shear-wave velocity depth profiles.

Guided acoustic waves

Guided acoustic waves consist of constructively interfering, post-critical P-wave reflections reverberating between the sea surface and seabed (Burg et al., 1951). They are commonly observed over a broad range of frequencies in active seismic marine surveys where the water depth is shallow and the sea bottom is hard (e.g., Shtivelman, 2004; Klein et al., 2005; Boiero et al., 2013).

Figures 5.6 and 5.7 show PP and ZZ virtual source gathers, respectively, for frequencies between $0.4 - 1.5$ Hz for the same two virtual source locations as in

virtual source gathers in the previous subsection. Note that the maximum offset in these gathers are now 30 km (twice as long as those in the gathers in the previous subsection). The strong, consistent arrivals in each of the virtual source gathers are likely guided acoustic waves for a number of reasons.

First, the group velocity of these arrivals is approximately 1500 m/s, which is the velocity of acoustic waves in water. Given that Scholte wave velocities at these frequencies are often observed to be on the order of 100s m/s (e.g., de Ridder and Dellinger, 2011; de Ridder et al., 2015), this energy is unlikely to be related to Scholte waves. Second, the signal-to-noise ratio for this event appears to be higher in the PP correlations (Figure 5.6) than in the ZZ correlations (Figure 5.7), and this same event dominates the PP correlations at frequencies below 0.4 Hz (Figure 5.3). Since hydrophones are coupled to the water and geophones are coupled to the ground, one would expect any waves propagating in the water, such as acoustic guided waves, to be stronger in the PP virtual source gathers than in the ZZ virtual source gathers.

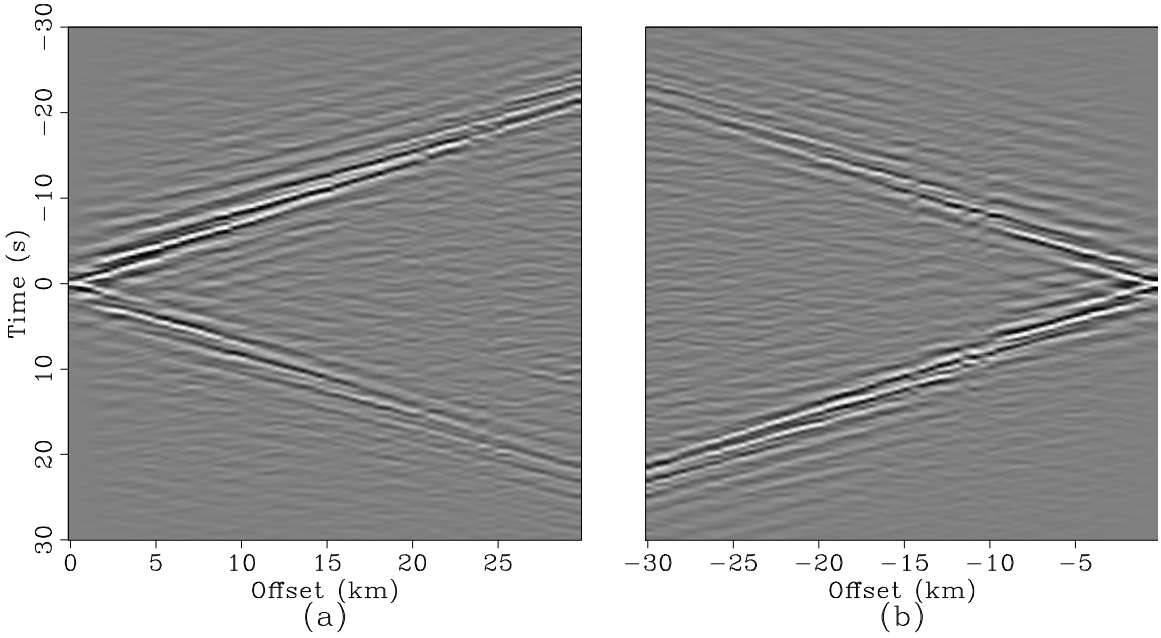

Figure 5.6: PP virtual source gathers for frequencies between $0.4 - 1.5$ Hz for two different virtual source locations. (a) Western node of the main array. (b) Eastern node of the main array. Positive offsets are toward the east while negative offsets are toward the west. Events propagating at 1500 m/s are acoustic guided waves. [**CR**] chap5/. guided-hh-end

In terms of kinematics, acoustic guided waves are observed to be dispersive and

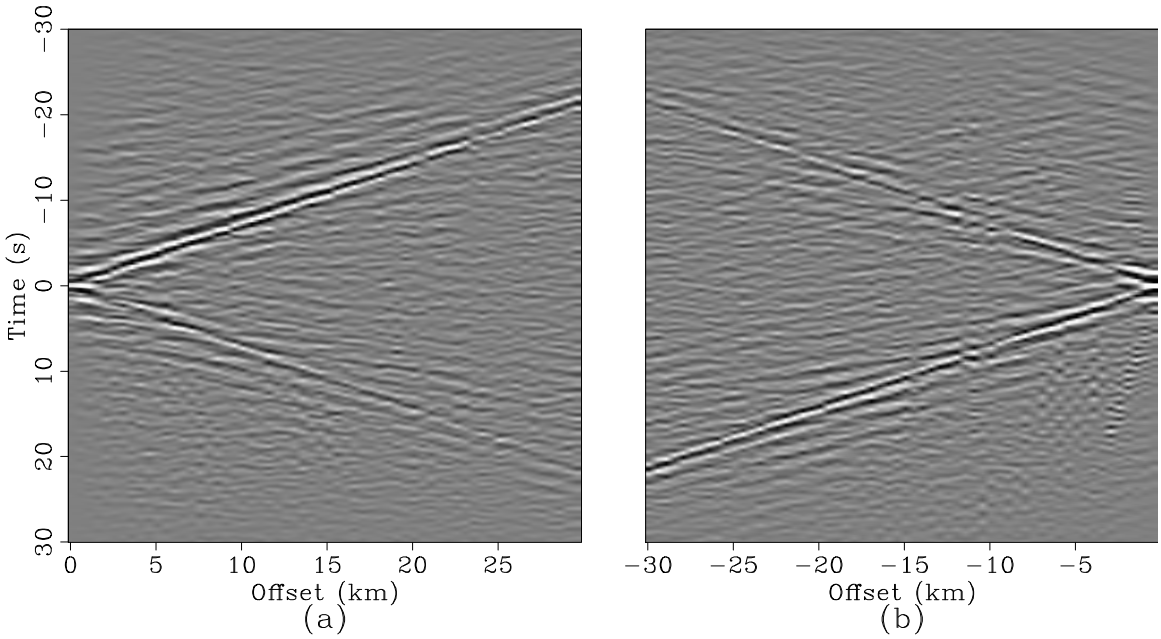

Figure 5.7: ZZ virtual source gathers for frequencies between $0.4 - 1.5$ Hz for two different virtual source locations. (a) Western node of the main array. (b) Eastern node of the main array. Positive offsets are toward the east while negative offsets are toward the west. Events propagating at 1500 m/s are acoustic guided waves. [**CR**] chap5/. guided-zz-end

their phase velocities exceed water velocity (Shtivelman, 2004). This dispersive pattern can be interpreted as due to the superposition of acoustic waves reverberating in the water column at various post-critical angles (Gualtieri, 2014). To verify this dispersive nature, I again create a dispersion image based on the PP virtual source gather (Figure 5.6a) using the same approach as outlined in the previous subsection. The only difference is that I perform the operation on a broader-band virtual source gather (up to 3 Hz instead of 1.5 Hz) to determine whether this signal extends over a broad range of frequencies like acoustic guided waves in active seismic surveys. The background image in Figure 5.8 shows that the apparent acoustic guided wave shares these dispersive traits, as phase velocity for a given mode exceeds water velocity as frequency decreases and approaches water velocity as frequency increases. Additionally, this event displays multiple modes, which has been observed in acoustic guided waves in a number of active seismic source studies (e.g., Klein et al., 2005; Boiero et al., 2013; Wang et al., 2016).

To further support the hypothesis that these events are acoustic guided waves, I compare the observed dispersion image to theoretical dispersion curves calculated using the following approximation from Hatchell and Mehta (2010) for guided waves in a liquid layer over a solid:

$$\tan\left[\frac{2\pi h f}{c}\sqrt{\frac{c^2}{v_1^2}-1}\right] = -\frac{\rho_2}{\rho_1}\frac{\sqrt{\frac{c^2}{v_1^2}-1}}{\sqrt{1-\frac{c^2}{v_2^2}}}, \tag{5.2}$$

where h is water depth, ρ_1 and ρ_2 are the densities of water and seafloor, respectively, f is frequency, v_1 is water velocity, v_2 is P-wave velocity of the seafloor, and c is guided-wave phase velocity. Solutions for phase velocity c and frequency f given $h = 1800$ m, $\rho_1 = 1000$ kg/m^3, $\rho_2 = 1800$ kg/m^3, $v_1 = 1500$ m/s, and $v_2 = 2300$ m/s (reasonable parameters given Alves (2017)) are shown in white in Figure 5.8. The theoretical and observed dispersion curves match quite well, further suggesting that these events are guided acoustic waves.

While commonly observed in shallow marine seismic surveys, guided acoustic waves have rarely been observed in passive seismic data at this combination of frequencies, spatial scale, and water depth. One similar case was from Hatchell and Mehta (2010), who used passive seismic interferometry to recover guided acoustic

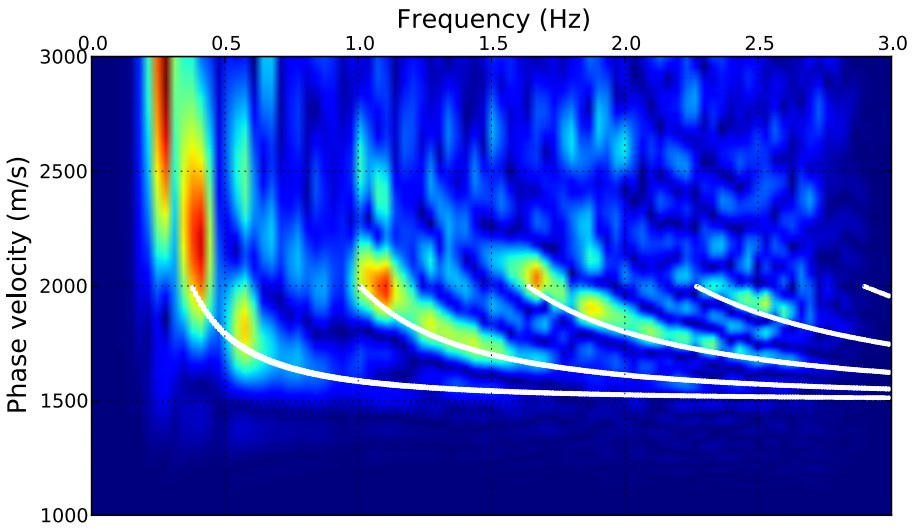

Figure 5.8: Guided wave dispersion image for the virtual source gather centered at the western node for the PP virtual source gather (Figure 5.6a). A gain proportional to frequency is applied to enhance the modes at higher frequencies. Warmer colors correspond to greater coherence of the dispersion estimate. The overlying white lines indicate theoretical dispersion curves using Equation 5.2 and the parameters outlined in the text. [**CR**] chap5/. dispersion-h-guided-overlay

waves from continuous seismic data recorded by OBNs 1000 m deep and with a maximum offset of 9600 m. In that study, the time asymmetry of the resulting acoustic guided waves were used to detect clock drifts. As seen with the theoretical dispersion curve calculation, though these acoustic guided waves propagate in the water, they interact with the seabed and are thus sensitive to elastic properties of the subsurface material (Klein et al., 2005). Therefore, it is possible to invert these acoustic guided wave dispersion curves for more detailed P-wave velocity depth profiles of the subsurface than the simple half-space model here (Klein et al., 2005; Boiero et al., 2013).

Critical refractions

Critical refractions, or head waves, occur where there are interfaces with sharp impedance contrasts. At Moere Vest, Alves (2017) identified refractions off the top of basalt using the active-source seismic data. Here, I examine the passive seismic data for similar critical refractions. Figure 5.9 shows time-symmetrized ZZ virtual source gathers for

frequencies between $0.5 - 2.0$ Hz for the same two virtual source locations as in the previous subsections. Though faint, there appear to be very fast linear events in both gathers (the stronger events are the acoustic guided waves). The same events in the PP virtual source gathers (not shown here) are even fainter. Because vertical geophones are coupled to the ground and not to the water column, this event is likely propagating in the subsurface. This interpretation, along with the high apparent velocity of the event and knowledge of the subsurface basalt, hints that these events are potentially critical refractions. Because of the polarity reversal and approximate 2-s difference in timing between the refractions in each gather, the earlier event could be a critical refraction off the top of basalt and the later event could be a similar event that additionally traveled through the water column as a multiple.

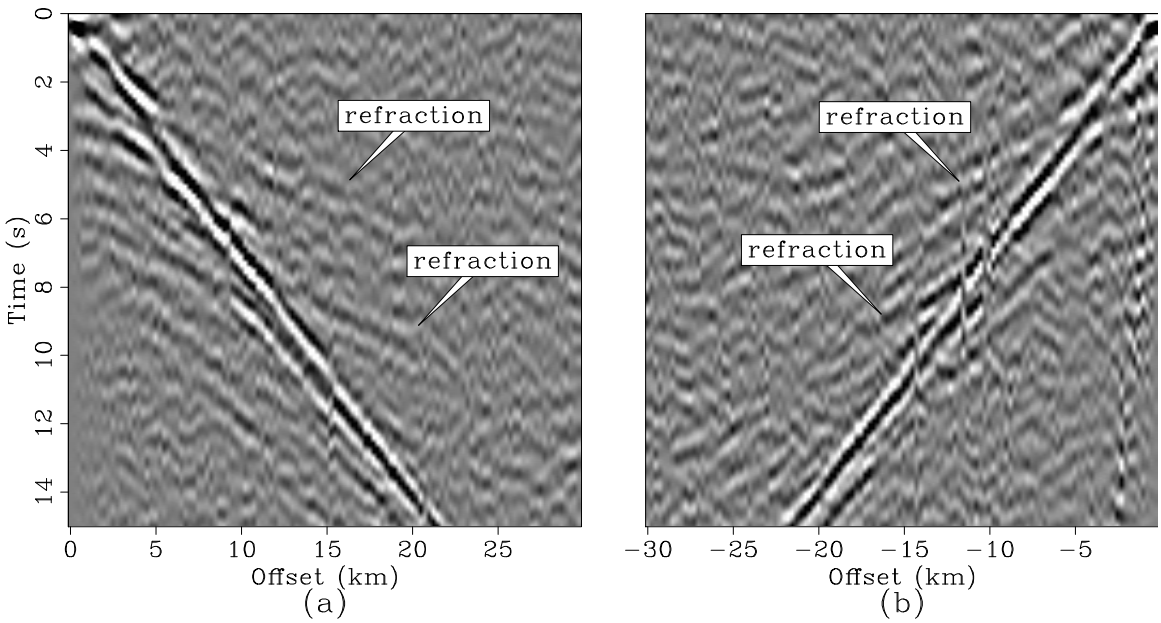

Figure 5.9: ZZ virtual source gathers for frequencies between $0.5 - 2.0$ Hz for two different virtual source locations. a) Western node of the main array. (b) Eastern node of the main array. Positive offsets are toward the east while negative offsets are toward the west. Though faint, potential critical refractions are observed. [**CR**] chap5/. refraction-zz-end

The simplest way to determine whether these events extracted from passive seismic data are critical refractions is to compare them to active-source data. Before doing so, differences in source location must be accounted for. Virtual sources are located at nodes on the sea bottom, while active sources are located near the sea surface. To get these two types of gathers to correspond to the same location, I reference the

virtual source gather from passive seismic data and the receiver gather from active seismic data to a common node. To get the gathers to begin at similar times, I shift the receiver gather from active data by 1.1 s. Given that water depth at Moere Vest is approximately $1600 - 1900$ m, this shift removes the approximate initial traveltime through the water column and effectively places the active seismic sources near the sea bottom. Though the angle of incidence of the initial path through the water column depends on source-receiver offset, I assume that it does not vary significantly from normal incidence due to ray bending from the high impedance contrast between the seabed and water.

Active-source vertical-geophone receiver gathers centered at the western and eastern nodes of the regular spread (same as in the previous subsections) are shown in Figure 5.10. I bandpass for frequencies between $2 - 6$ Hz, apply a linear gain proportional to offset, and heavily clip the gathers to enhance the critical refractions. Comparison of these events to the fast linear events in the corresponding ZZ virtual source gathers in Figure 5.9 reveals similar arrival times and moveout velocities. The similarity not only pertains to the early linear arrivals, but also to the later linear arrivals. As in the potential critical refractions from passive seismic data, these linear events also display opposite polarities and are separated by approximately 2 s, which suggests these later events could be multiple-related critical refractions.

One approach to enhance the stacking power of the potential critical refraction events in the passive seismic data is to stack over all virtual source gathers to create a super-source gather (Lin et al., 2013; Nakata et al., 2015). The trade-off is that all detailed spatial information is lost, as the procedure effectively assumes a 1D medium. The ZZ super-source gather (Figure 5.11a) reveals stronger critical refractions than in the individual virtual source gathers (Figure 5.9). These events are apparent at both negative and positive times, as well as both positive and negative offsets, which indicates that the potential critical refractions are propagating in both directions along the array. The symmetry of these events in time and space suggest that these events are not generated by localized sources, and that their fast velocities are not just apparent velocities from plane waves hitting the array at a specific angle.

The vertical-radial (ZR) super-source gather (Figure 5.11b) also displays hints of refraction-like events that were not apparent in corresponding individual virtual source gathers (not shown here). Compared to the ZZ super-source gather, the fast

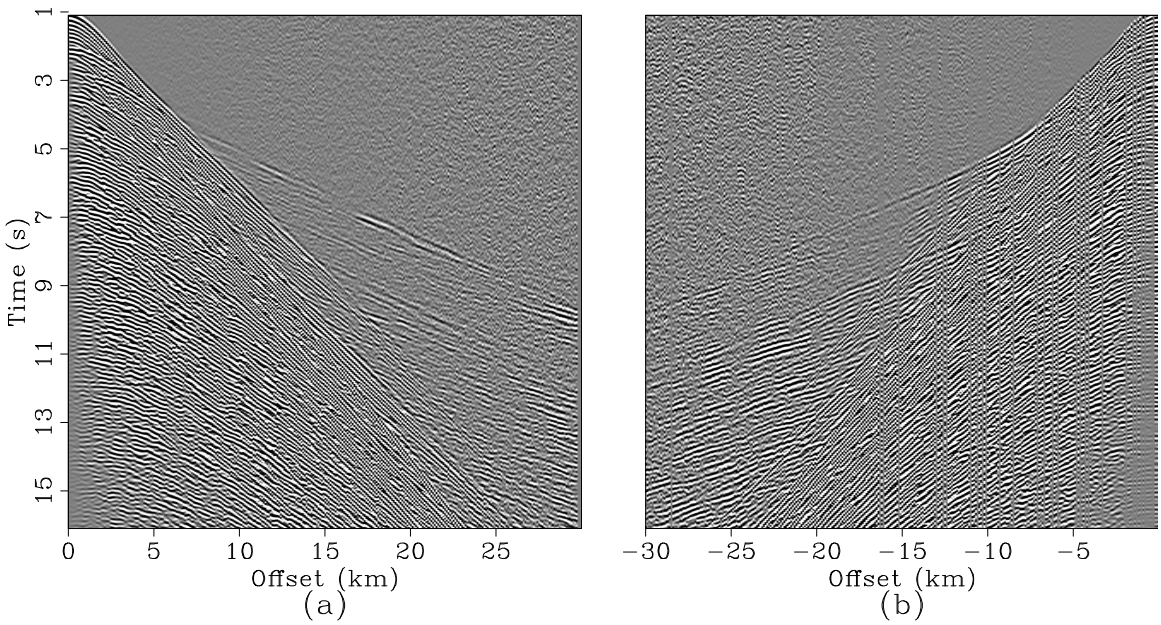

Figure 5.10: Vertical-geophone receiver gathers for frequencies between $2 - 6$ Hz for two different virtual source locations. a) Western node of the main array. (b) Eastern node of the main array. Positive offsets are toward the east while negative offsets are toward the west. A linear gain proportional to offset and a strong clip are applied to enhance the critical refractions. [**CR**] chap5/. active-zz-half

linear events arrive later in time. Furthermore, these events are only apparent at positive time lags. This observation could provide insight into how these potential critical refractions are generated in Earth's ambient seismic noise field, as they suggest that refractions only appear when reaching the vertical geophone before the radial geophone (and not vice versa). One hypothesis is that these refractions are the result of storm-induced down-going energy in the water column interacting with the top of basalt.

To examine whether the difference in arrival times of the potential critical refractions in the virtual super-source gathers in Figure 5.11 is reasonable, I compare the positive time lags of the virtual super-source gathers to their respective vertical- and radial-component receiver gathers from active seismic data. Though the virtual super-source gathers do not correspond to a specific spatial location while the receiver gathers do (here, the common node is the western node in the regular spread), it is an adequate comparison for investigating the relative arrival times of the critical

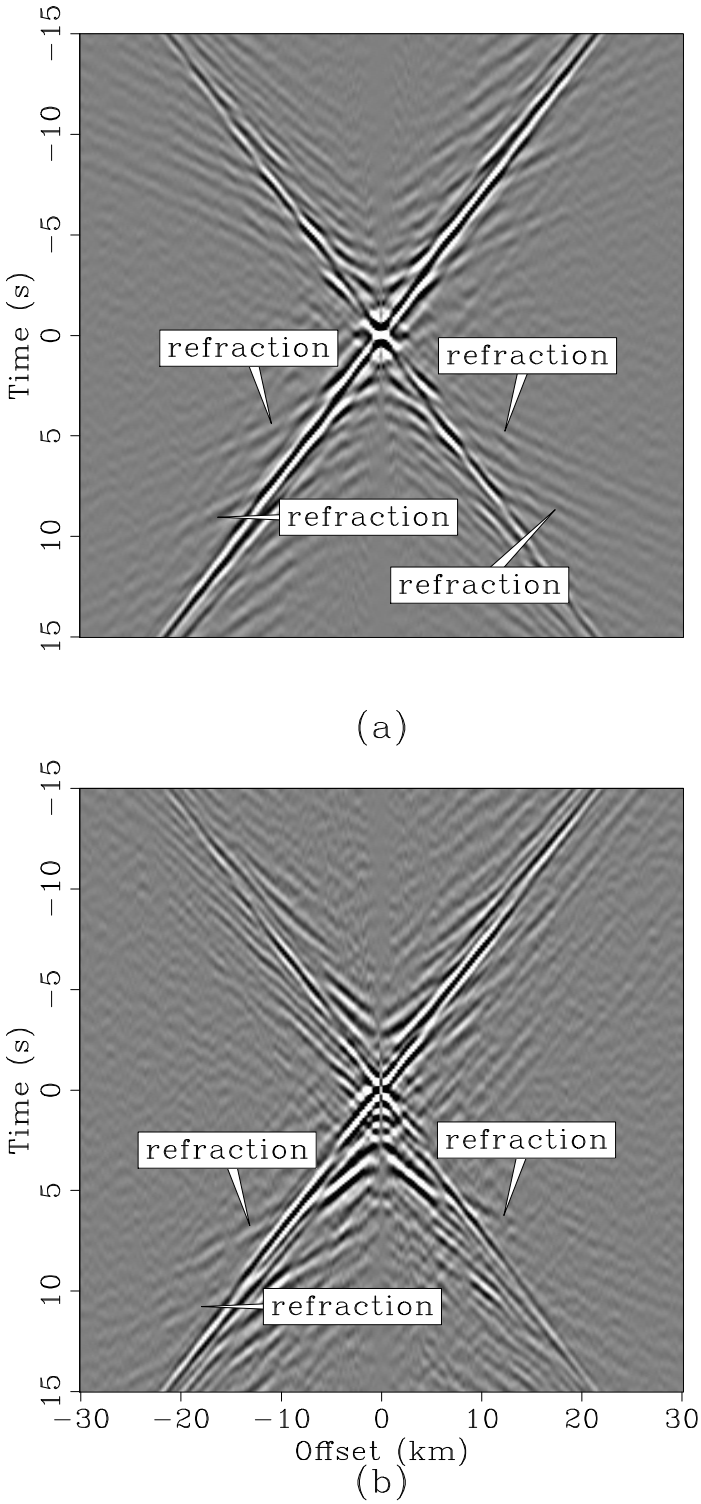

Figure 5.11: Virtual super-source gathers for frequencies between $0.5 - 2.0$ Hz. (a) Vertical-vertical geophone correlations. (b) Vertical-radial geophone correlations. Note the difference in the first refraction arrival times between the two gathers, particularly at positive time lags. [**CR**] chap5/. super-unsym

refraction between different geophone components. The arrival times of the critical refraction event in the ZZ super-source gather and vertical-component receiver gather are similar (Figure 5.12). Using these arrival times as a reference, it is clear that the corresponding fast linear events in both the ZR super-source gather and the radial-component receiver gather arrive relatively later by similar amounts of time (Figure 5.13).

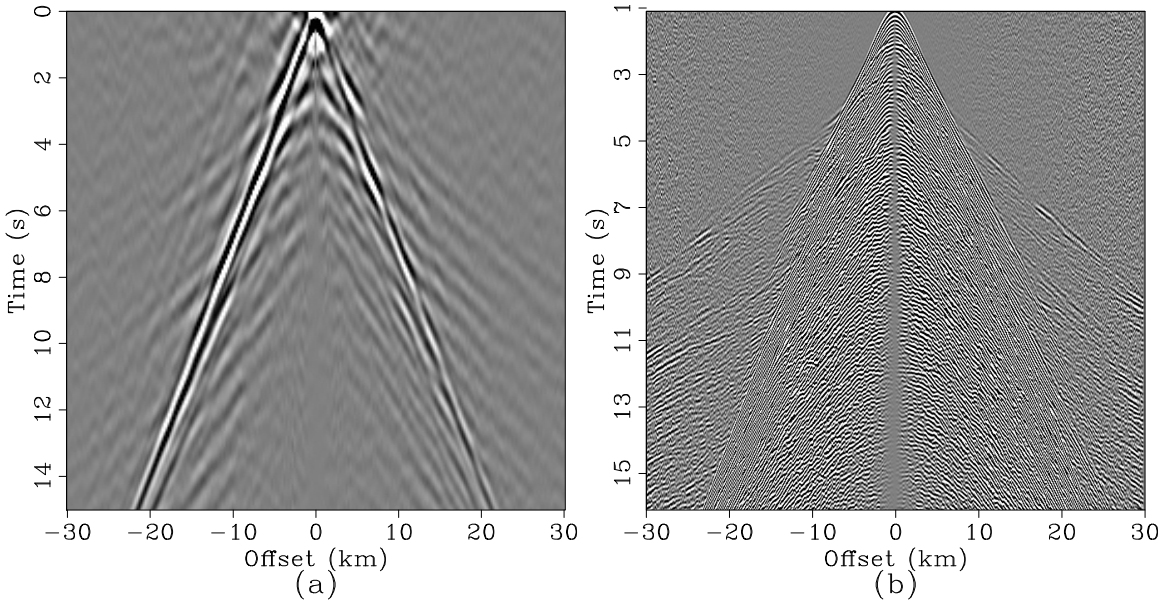

Figure 5.12: Comparison of (a) positive time lags of ZZ virtual super-source gather and (b) time-shifted vertical-geophone receiver gather for the western node in the main array. Note that the critical refraction times are comparable. [**CR**] chap5/. comp-zz-full

Moronfoyer et al. (2016) hypothesized that the difference in arrival times of the critical refraction in the two geophone components was due to differences in subsurface P-wave and S-wave velocities. The vertical component recorded the faster P-wave refraction while the radial component recorded the slower converted S-wave refraction. Regardless of the true cause for the differences in critical refraction arrival times, the fact that fast linear events in the ZZ and ZR super-source gathers display similar refraction arrival time differences as those in the active seismic data is another piece of evidence supporting the classification of the fast linear events in the virtual source gathers as critical refractions.

To compare the velocities of the apparent refractions in the passive and active

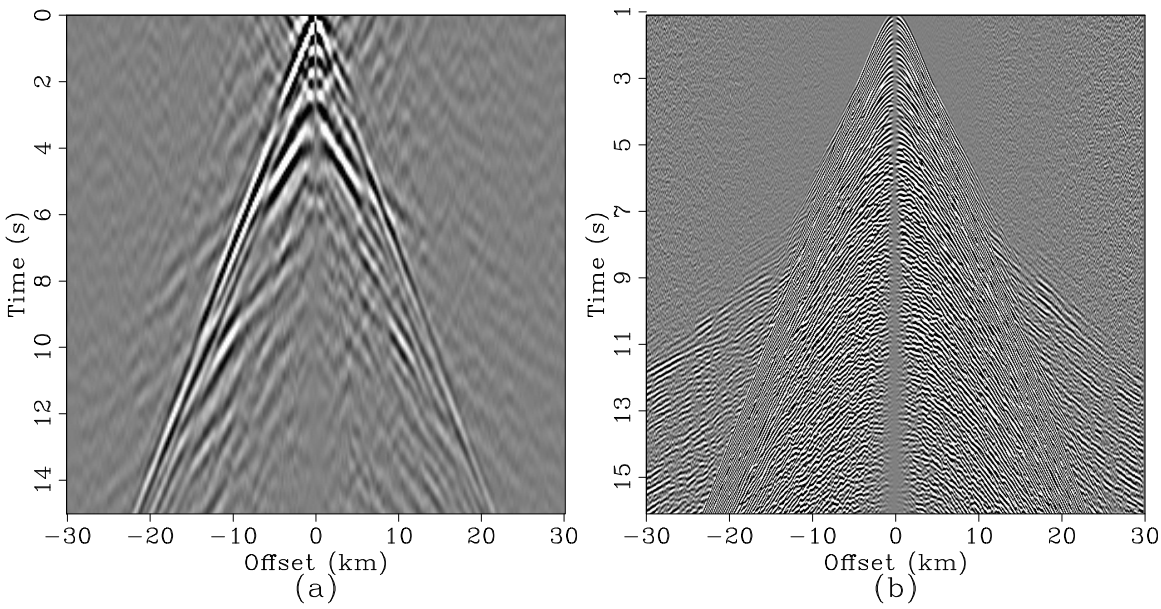

Figure 5.13: Comparison of (a) positive time lags of ZR virtual super-source gather and (b) time-shifted radial-geophone receiver gather for the western node in the main array. Note that the critical refraction times are comparable to each other and later than the corresponding refractions in the vertical geophone receiver gathers. [**CR**] chap5/. comp-zx-full

seismic data, I perform linear moveout (LMO) on the gathers. Results using a moveout velocity of 4400 m/s on the ZZ and ZR virtual super-source gathers are shown in Figures 5.14a and 5.15a, while the corresponding vertical- and radial-geophone receiver gathers after LMO with the same velocity are shown in Figures 5.14b and 5.15b, respectively. The apparent critical refractions in both the virtual super-source gathers and receiver gathers (at least at positive offsets) appear to be flattened at this high moveout velocity, thus providing another piece of evidence that I am recovering critical refractions in the passive seismic data. Note that the refractions in the receiver gathers are not quite flat at negative offsets (where sources are west of the receiver node); they require moveout with a higher velocity to be flattened. This is likely because the basalt tilts slightly downward toward the west, and apparent refraction velocities are typically slower shooting down-dip (toward the west) than up-dip (toward the east).

This trend of different critical refraction velocities depending on node location cannot be observed in the super-source gathers. This is because the negative offsets in the virtual super-source gathers are sensitive to a different part of the basalt than

the negative offsets of the receiver gather centered at the western node of the regular array. Because of the relatively large number of nodes in the regular spread of the array, both offsets of the virtual super-source gathers are biased towards the critical refraction response off the basalt directly beneath that particular subset of the array. While the positive offsets of the receiver gather centered at the western node of the regular array sense the same refraction off the basalt beneath the regular spread, the negative offsets sense the refraction off the basalt that is west of the regular spread. As a result, the negative offsets of the receiver gather are not flattened at 4400 m/s while the positive offsets and virtual super-source gathers are.

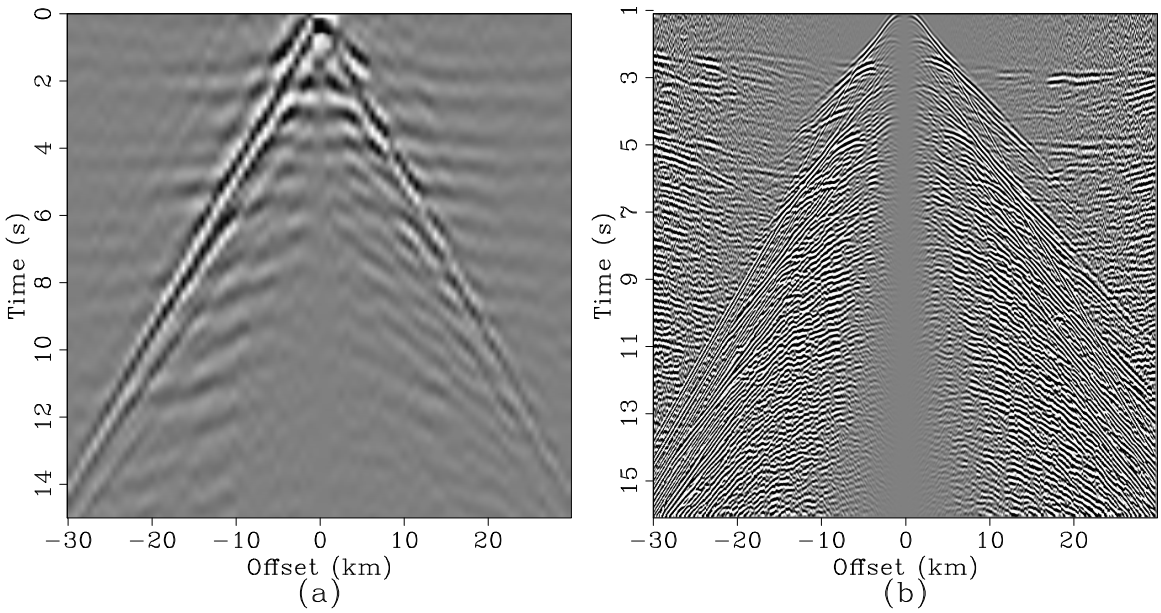

Figure 5.14: Comparison of (a) positive time lags of ZZ virtual super-source gather and (b) vertical-geophone receiver gather for the western node in the main array after LMO at 4400 m/s. [**CR**] chap5/. comp-zz-full-lmo

Overall, there is evidence that I am extracting critical refractions from passive seismic data, particularly when comparing these events to active data. These types of events from passive seismic data have never been observed before. They are observed at Moere Vest for a couple of potential reasons. One is that the array provides sufficiently long offsets for potential refractions to become well-separated from other events, such as guided acoustic waves. Another reason is that there is a basalt body in the subsurface, which is likely to produce the high-impedance interface needed for critical refractions to be generated. Two hypotheses for how these critical refractions are generated are:

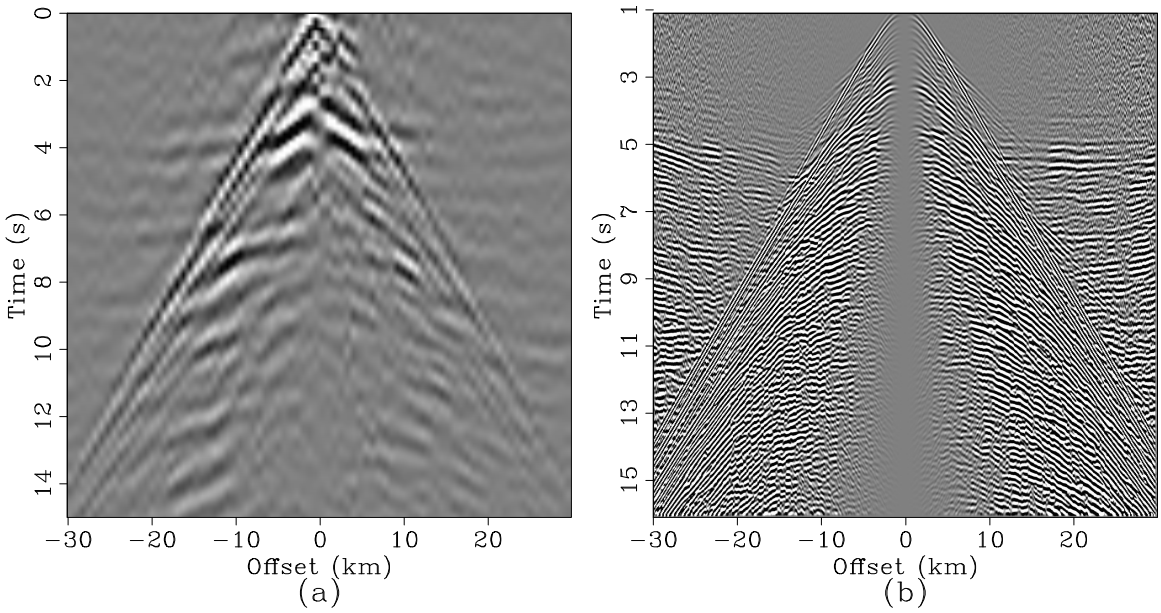

Figure 5.15: Comparison of (a) positive time lags of ZR virtual super-source gather and (b) radial-geophone receiver gather for the western node in the main array after LMO at 4400 m/s. [**CR**] chap5/. comp-zx-full-lmo

- storm-generated P-wave energy producing refractions, and
- surface waves interacting with the top of basalt and converting into refractions.

I investigate the latter hypothesis for the generation of critical refractions in passive seismic energy in the following section.

NUMERICAL MODELING OF CRITICAL REFRACTIONS

Because this example from Moere Vest is the first instance of the successful extraction of critical refractions from the ambient seismic noise field, the natural generation of these wave modes is not well established. However, knowing that Earth's ambient seismic field is dominated by surface waves, one hypothesis is that Scholte waves are interacting with the top of basalt and subsequently converting or scattering into critical refractions and diffractions. Given it appears that the Scholte-wave wavelengths vary approximately between 1250 m at 0.4 Hz and 3000 m at 0.2 Hz, it is possible that they penetrate deep enough to sense the basalt's horst-and-graben structure

approximately 1 km beneath the sea bottom.

To test this hypothesis, I simulate wavefield conversions using a staggered-grid elastic finite-difference wave propagation code (Fabien-Ouellet et al., 2017) on a simplified 2D elastic model of Moere Vest consisting of three layers: a water layer, an overburden layer, and a basalt layer with a 100-m thick step feature to mimic the sharp corners of a horst-and-graben structure (Figure 5.16). Specific values for the elastic parameters were estimated from Alves (2017) and can be found in Table 5.1. The model spans 5000 cells in the horizontal direction and 800 cells in the vertical direction, and has a grid spacing of 10 m. Because I am interested in observing the interaction of low-frequency Scholte waves with the simple step feature of the top of basalt, I place an explosive source with a 0.4 Hz Ricker wavelet 25 km away from the step feature and 50 m below the sea bottom. The source goes off at 4 s. The distance between the source and the step function is large so that the Scholte wave is separated from other wave modes (refractions and direct waves) by the time it reaches the step feature. I also place absorbing boundary conditions along all sides of the model, as I want to reduce interference from waves reflecting off the sea surface. I run the propagation for 50000 time steps of length 0.008 s.

Layer	Thickness [m]	V_p [m/s]	V_s [m/s]	Density [kg/m^3]
Water	1500	1500	0	1000
Overburden	1000	2300	1400	1800
Basalt	infinite	5000	3000	2500

Table 5.1: Model parameters for the simple three-layer model with a 100-m thick step feature at the top of basalt shown in Figure 5.16.

Figure 5.17a shows the resulting vertical-velocity source gather recorded by receivers along the water bottom. To help interpret the events, I include the resulting source gather when using a 7 Hz Ricker wavelet (Figure 5.17b) because the events are better separated. I also include snapshots of the wavefield at 20 s for both experiments in Figure 5.18. Note that the energy at near offsets at low frequencies is an artifact of the modeling procedure.

The fastest group of arrivals appear to be critical refractions, given that the event is propagating at approximately 5000 m/s (most apparent in Figure 5.17b), which is the P-wave velocity of the basalt layer. The next fastest event appears to be direct P-waves, as they are propagating at close to 2300 m/s, which is the P-wave

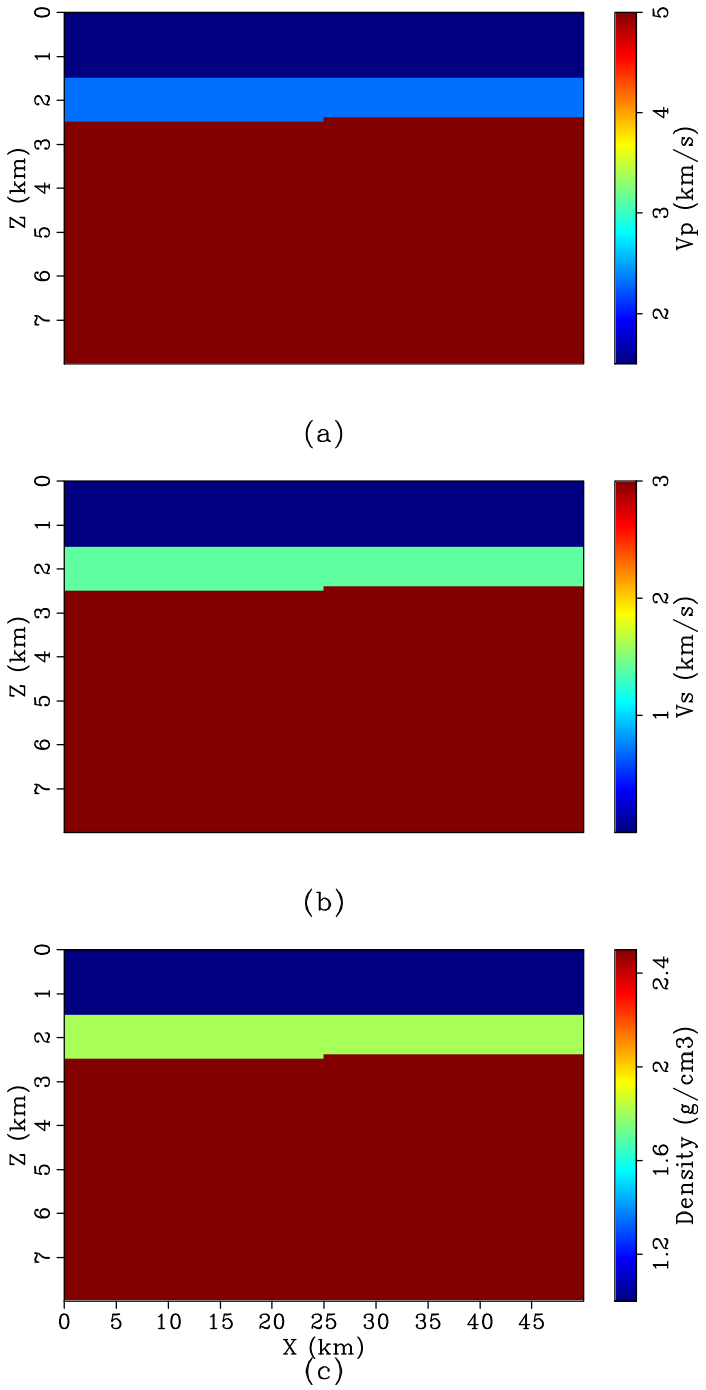

Figure 5.16: Model used for generating synthetic source gathers. The simple three-layer model consists of a water layer, an overburden, and a basalt body with a step feature. (a) P-wave velocity. (b) S-wave velocity. (c) Density. Nodes are located at the water-solid interface and the source is located 50 m below the sea bottom on the left side of the model. Note that vertical and horizontal axes are not to scale in order to enhance the step feature in the basalt. [**ER**] chap5/. moerevest-model

velocity of the overburden layer. The slowest event appears to be propagating at approximately 1100 m/s. Though this moveout velocity is close to the S-wave velocity in the overburden of 1400 m/s, the snapshots of the wavefield at 20 s (Figure 5.18) suggests that this linear event is related to the wavefield trapped at the solid-liquid interface at approximately 18 km. Therefore, it appears that this slow event is the Scholte wave of interest.

Assuming the slower packet of arrivals is related to Scholte waves, there is apparent forward- and back-scattered energy at the location of the step feature (25 km) at low frequencies. To better examine the scattered events, I subtract the source gather associated with the basalt with the step feature from a source gather associated with the basalt without the step feature (not shown here) to produce Figure 5.19. While the incident critical refraction and direct P-wave display both forward and back-scattered energy, I focus on the scattered energy from the incident Scholte wave. As expected, the incident Scholte wave produces a back-scattered Scholte wave with the same propagation velocity. More importantly, there is a strong and fast linear event with moveout velocity of approximately 5000 m/s that is clearly back-scattered off the step feature. This is the P-wave velocity of the modeled basalt. Therefore, numerical modeling of wavefield propagation supports the hypothesis that a critical refraction can be generated from a Scholte wave interacting with the horst-and-graben structure of the top of basalt. These refractions are generated even if the step feature is as thin as 100 m.

DISCUSSION

The microseism band at Moere Vest contains a wealth of spatially coherent seismic signals. Because the microseism band is typically dominated by surface waves, the presence of coherent Scholte waves is expected. The extracted acoustic guided waves is less common from passive seismic data but can provide complementary subsurface information to Scholte waves. By inverting the dispersion curve of the Scholte wave for an S-wave velocity depth profile and inverting the dispersion curve of the acoustic guided wave for a P-wave velocity depth profile, it may be possible to estimate Vp/Vs ratios at Moere Vest without active seismic sources, which can be useful for classifying different subsurface lithologies and for generating starting velocity models for elastic full-waveform inversion.

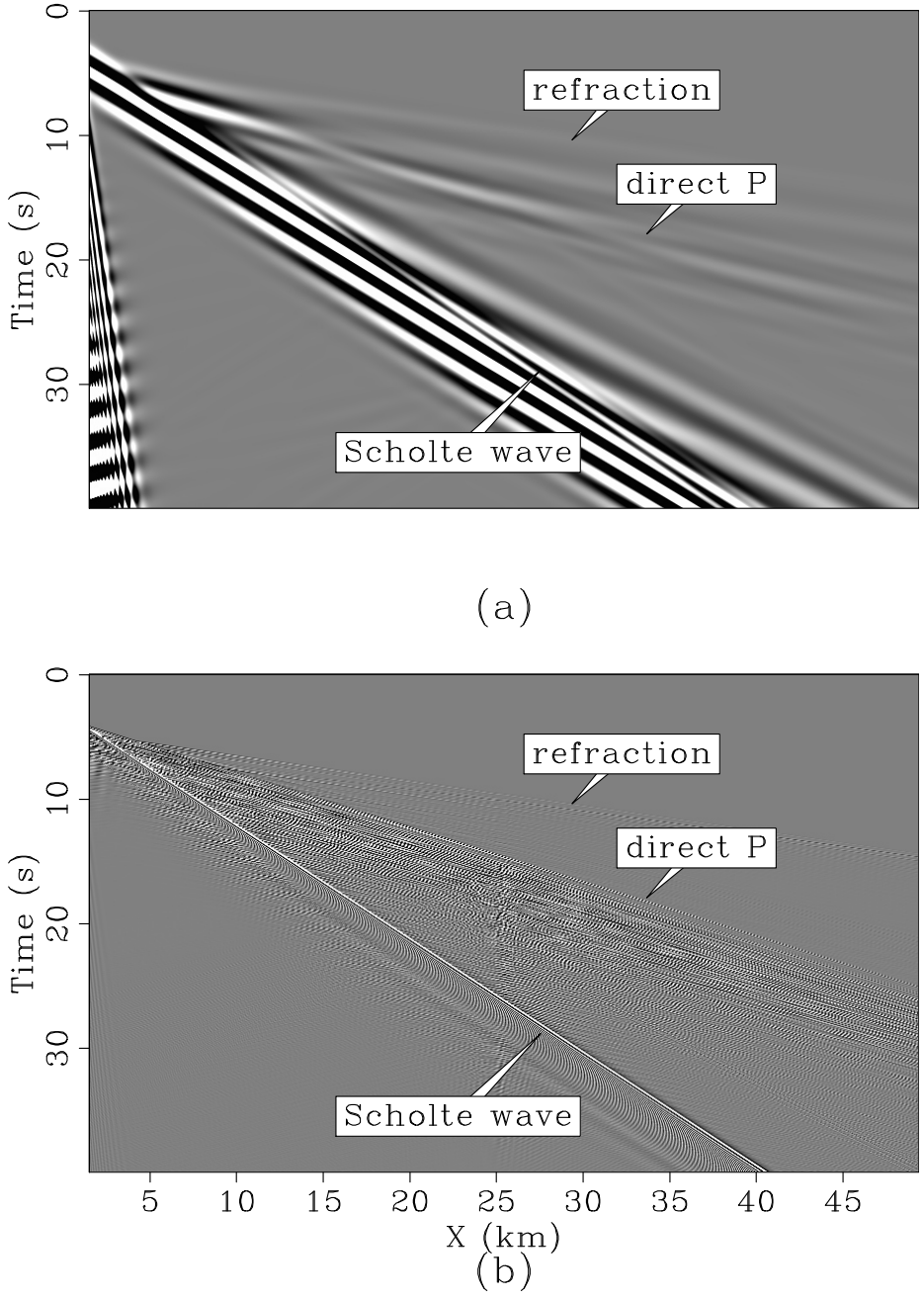

Figure 5.17: Modeled source gathers for two different frequencies. (a) 0.4 Hz. (b) 7 Hz. [**CR**] chap5/. dat-step-vz

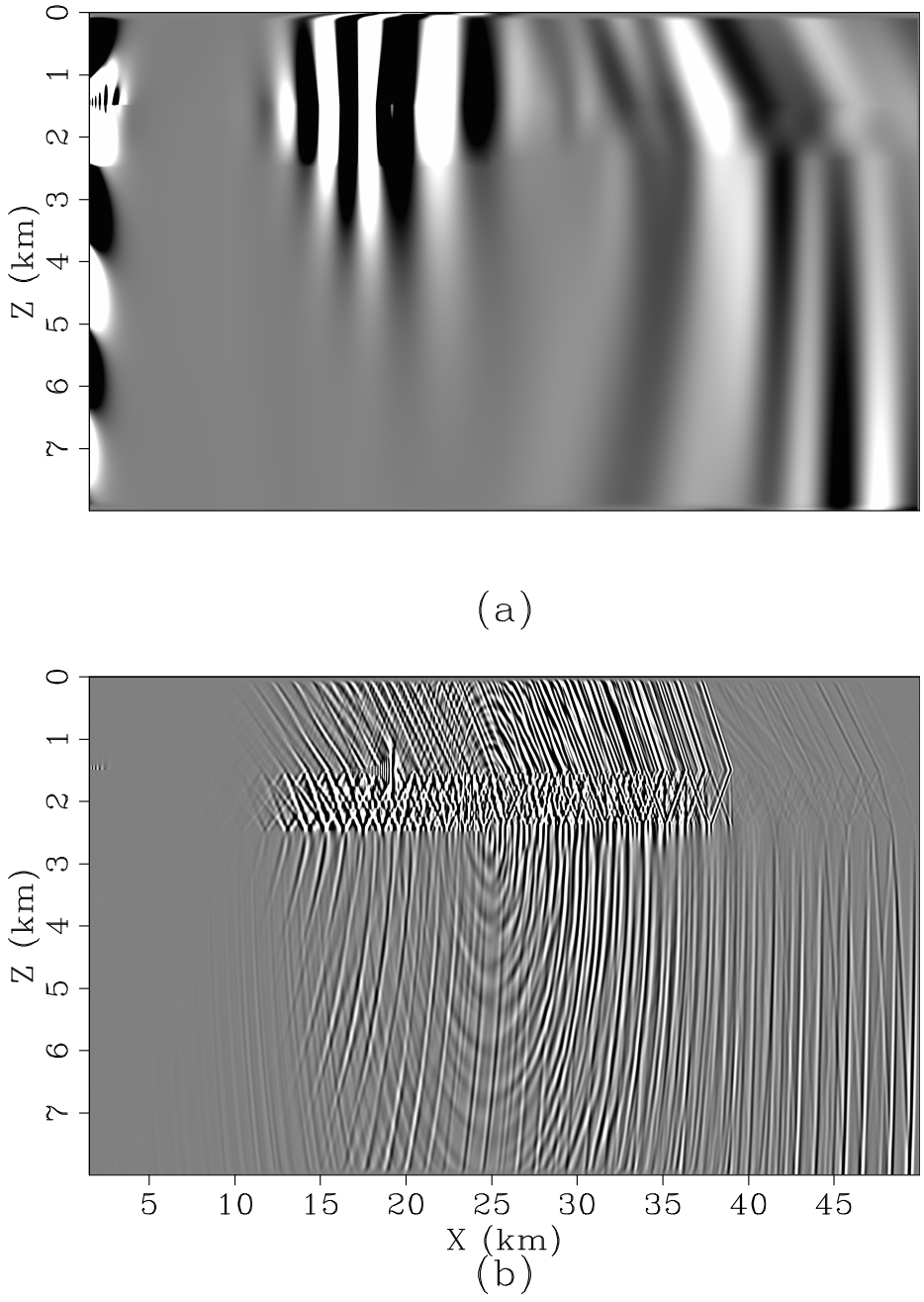

Figure 5.18: Snapshot of the wavefield at 20 s for two different frequencies. (a) 0.4 Hz. (b) 7 Hz. [**CR**] chap5/. mov-step-vz

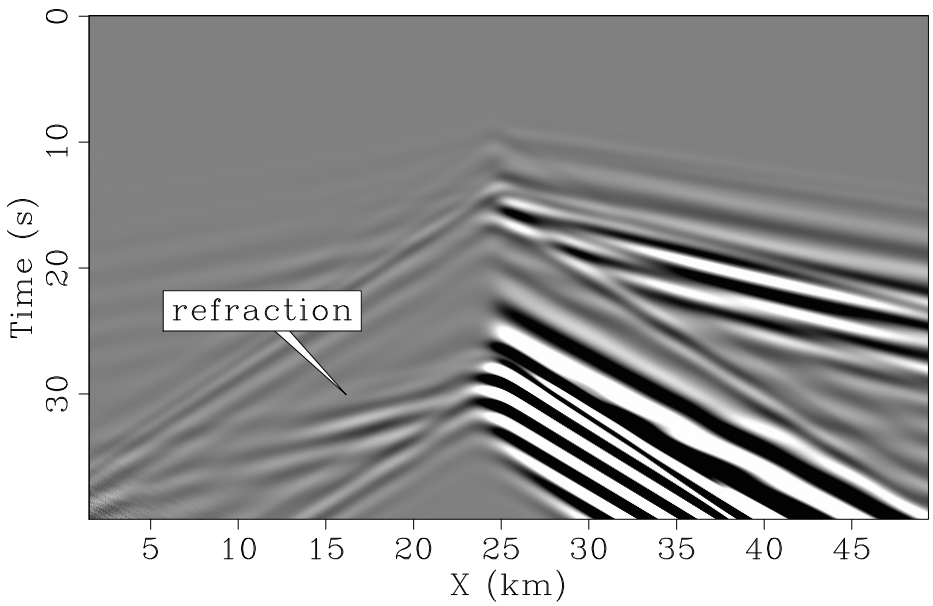

Figure 5.19: Difference between 0.4 Hz vertical-velocity source gathers with and without the step feature at the top of basalt. Note that the back-scattered energy from the incident Scholte wave interacting with the step feature appears to be comprised of both surface waves and critical refractions. [**CR**] chap5/. diff-p4-step-vzA

The extraction of apparent critical refractions from passive seismic data has never been observed before. While stacking over all individual virtual source gathers enhanced these events, the resulting virtual super-source gathers do not provide the spatial detail required for seismic imaging. Therefore, further processing steps would be needed to extract these weak events in the individual virtual source gathers. The challenge appears to be dampening the energy from the acoustic guided waves, which are masking the critical refraction energy. One approach is to use an FK filter to attempt to remove the acoustic guided waves in the individual virtual source gathers. Another approach is to create a correlation-based selection filter that selects two-hour correlations with relatively strong refraction energy prior to stacking (Nakata et al., 2015). In this approach, the critical refractions in the virtual super-source gathers are the reference events. Once the critical refractions are isolated in each individual virtual source gather, it may be possible to perform refraction imaging techniques to estimate velocity models and stratigraphic layer thicknesses.

While the wave modes at Moere Vest are intriguing, there is still uncertainty regarding how the guided acoustic waves and critical refractions are generated. Because the frequencies I am looking at here are lower than the frequencies of a typical active

seismic survey, these events are unlikely to be human-generated. The acoustic guided waves require there to be interfering post-critical reflections within the water column. Based on the spectrograms, it appears that there is an increase in microseism energy between periods of active seismic shooting, which could be indicative of stormy weather conditions. As a number of studies have shown (e.g., Gerstoft et al., 2008c; Zhang et al., 2010; Landès et al., 2010), P-waves can be generated by storms inducing large ocean waves that interact in deep-water environments. Given that Moere Vest is located in a deep-water environment, it is possible that the acoustic guided waves could originate from the interaction of storm-induced ocean waves in nearby regions. Similarly, critical refractions could also be induced by P-waves generated by storm-induced microseisms in deep-water environments. Alternatively, the critical refractions could be generated by long-period Scholte waves interacting with the horst-and-graben structure of the top of basalt, as modeled in the previous section.

Regardless of the true mechanism for the natural generation of critical refractions, there are reasons to believe that critical refractions from passive seismic data are not restricted to Moere Vest. First, for a critical refraction to be observed, a high-velocity layer must exist in the subsurface. Here, it is a relatively flat basalt layer, but it could be another material such as salt. Second, there must be strong microseism energy, whether in the form of P-waves or surface waves. Microseism energy is recorded at all locations and is particularly strong in deep-water environments during stormy weather. These requirements are commonly found throughout the world. Thus, what makes Moere Vest unique is not the location, but rather the array, which provides long enough offsets for refractions to separate from the guided acoustic wave. With similar arrays, critical refractions in passive seismic data can be more commonly observed.

CONCLUSIONS

Using passive seismic interferometry, I found that the continuous seismic recordings from the Moere Vest OBN array contained apparent Scholte waves, guided acoustic waves, and critical refractions. While Scholte waves are commonly extracted from Earth's ambient seismic noise field, the latter two wave modes are not. Acoustic guided waves are commonly observed in shallow-water active seismic surveys, but had rarely been observed in passive seismic data at low frequencies and deep depths. At Moere Vest, I found that the dispersion image for the passive acoustic guided wave

had similar dispersive characteristics as those from typical active seismic surveys. Much like Scholte waves, these dispersion curves can be inverted for depth profiles of seismic velocities. Even more rare are critical refractions, which had never been observed in passive seismic data before. I found that the arrival times of potential critical refractions from passive seismic data compared well to those from active data. I hypothesized that one potential mechanism for the natural generation of critical refractions is that they are converted from low-frequency Scholte waves interacting with the horst-and-graben structure of the top of basalt. I validated the feasibility of this hypothesis through numerical modeling of wavefield propagation through a simplified elastic model containing a basalt layer with a simple step feature. Overall, it is likely that the length of the array, the presence of a high-impedance interface at the top of basalt, and strong microseism energy allowed the acoustic guided waves and critical refractions to be visible.

ACKNOWLEDGEMENTS

I would like to thank Seabed Geosolutions for use of this data set and permission to share results. This work used the XStream computational resource, supported by the National Science Foundation Major Research Instrumentation program (ACI-1429830).

Appendix A

Body-wave energy at Long Beach

While estimated Green's functions (EGFs) from the ambient seismic noise field are typically dominated by surface waves, there are instances of body-wave energy in EGFs, including P-wave reflections off the Moho (Ruigrok et al., 2011; Zhan et al., 2010) and exploration-scale reflections in isolated locations (Nakata et al., 2011; Draganov et al., 2013). At Long Beach, there were no clear indications of body-wave energy in either the beamforming analysis (Figure 2.10) or individual high-frequency virtual source gathers (Figures 3.4 and 3.5). However, by stacking over all virtual source gathers in the array, it is possible to enhance the body-wave signal at Long Beach (Lin et al., 2013).

To extract body waves, the virtual source gathers are sorted into 50 m offset bins, frequency bandpassed between $4 - 9$ Hz, and averaged over causal and acausal time lags. The resulting gather, which I call a virtual super-source gather, is shown in Figure A.1 and is the foundation for the work in Nakata et al. (2015). There are clear body waves propagating between 2 km/s and 2.75 km/s. They appear to begin propagating at zero time and have velocities that increase with offset, which suggests that these events are diving waves. Given that the array consists of only vertical-component geophones, these events are likely P-diving waves.

Because I am stacking over all virtual sources, the resulting virtual super-source gather has poor spatial information. To select EGFs with strong body-wave energy between individual source-receiver pairs, a second cross-correlation between the virtual super-source gather and individual virtual source gathers is required. Once EGFs

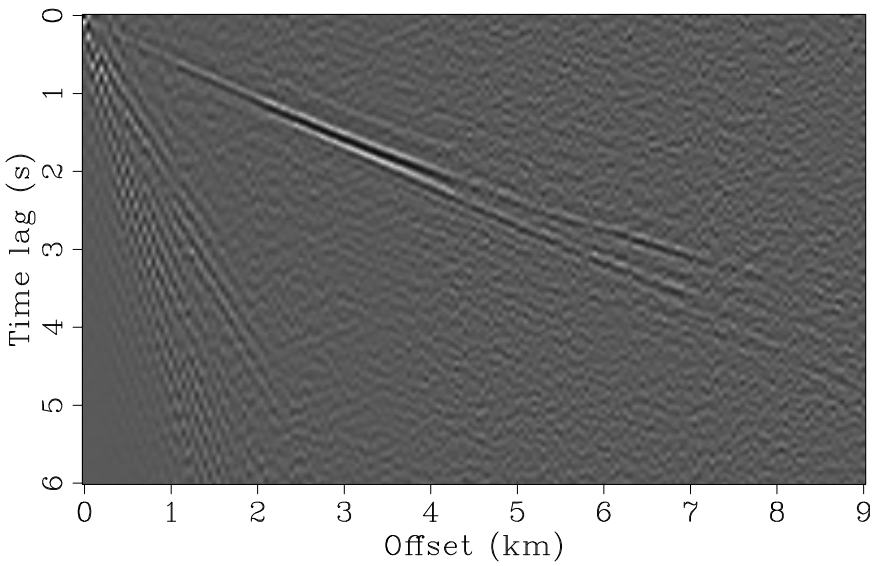

Figure A.1: Virtual super-source gather created from stacking over all virtual-source gathers in the Long Beach array. The frequency range is 4–9 Hz. Diving P-waves are clearly observed to be propagating between 2 km/s and 2.75 km/s. [**CR**] appendA/. lb-supergather-all

with a maximum correlation value over a certain threshold are selected, a body-wave tomography can be performed (Nakata et al., 2015).

While beamforming on the ambient seismic noise field suggested the presence of Rayleigh waves originating from Interstate 405 and local roads (Figure 2.10), it failed to reveal any body waves propagating. Therefore, to determine which direction the body waves are coming from, I sort the virtual super-source gather by virtual source-receiver pair azimuth and stack them into 10-degree bins. Azimuth is defined as the angle of the receiver with respect to the virtual source, with 0 degrees corresponding to a receiver due north of the source and +90 degrees corresponding to a receiver due east of the source. I also keep causal and acausal time lags, rather than average them, to help the interpretation of the resulting partial virtual super-source gathers.

Figure A.2 shows three resulting partial super-source gathers for different azimuths and frequencies between $4 - 9$ Hz. From top to bottom, the panels correspond to azimuths between $175 - 185$ degrees (receivers south of the virtual source), $145 - 155$ degrees (receivers south-southeast of the virtual source), and between $85 - 95$ degrees (receivers east of the virtual source). These trends are apparent in each day of virtual source gathers (not shown here), suggesting that these trends are consistent over time.

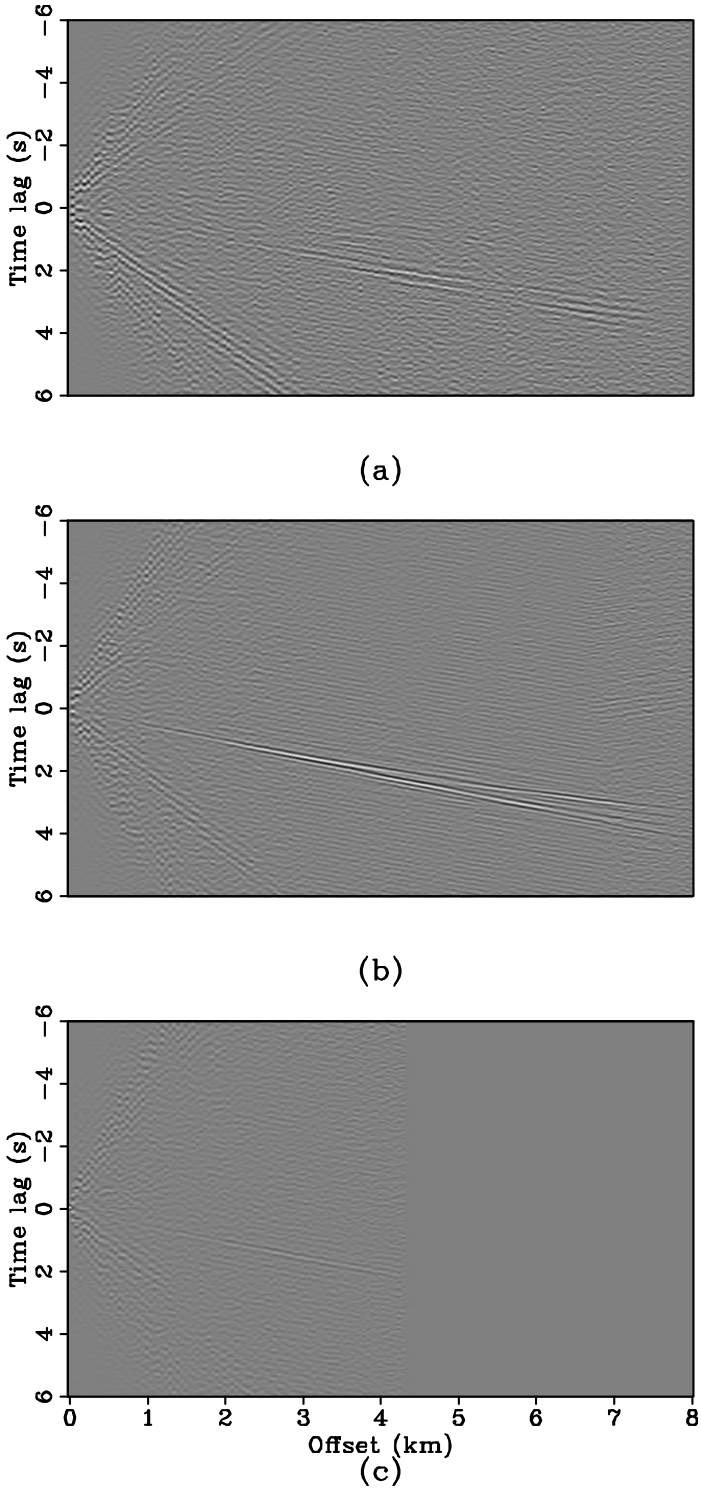

Figure A.2: Virtual super-source gathers for frequencies between $4 - 9$ Hz along different source-receiver azimuths. (a) $175 - 185$ degrees (receivers south of the virtual source). (b) $145 - 155$ degrees (receivers south-southeast of the virtual source). (c) $85 - 95$ degrees (receivers east of the virtual source). All gathers are clipped independently to enhance any arrivals. [**CR**] appendA/. lb-supergather-azi

The first observation is that none of these gathers are symmetric over zero time lag. Because events at acausal time lags correspond to energy moving toward the virtual source while events at causal time lags correspond to energy moving away from the virtual source, it is clear that noise sources are unevenly distributed in space. Here, the body-wave energy is generally found at causal times, which suggests that body waves are generated from inland rather than from the ocean (given the azimuthal orientation of the virtual sources and receivers in Figure A.2).

The second observation is that the body waves are relatively strongest (compared to any other arrivals) for orientations along the northwest-southeast direction (Figure A.2b), followed by the north-south (Figure A.2a) and east-west (Figure A.2c) directions. Therefore, body-wave energy appears to be most strongly propagating from northwest to southeast. One possible explanation for this energy is that it is aircraft-generated noise from Long Beach Airport in the northwest part of the array. Overall, body-wave energy can be observed in the ambient seismic noise field at Long Beach, and it appears to preferentially propagate from northwest to southeast across the array.

Appendix B

Low-frequency virtual source gathers at Long Beach

While high-frequency virtual source gathers at Long Beach demonstrate relatively low signal-to-noise ratios (SNRs) and require knowledge of the location of major roads and highways within the array for interpretation (Figures 3.4 and 3.5), low-frequency ($0.5 - 2.0$ Hz) virtual source gathers display much higher SNR and are much simpler to interpret. The virtual source gathers shown here were the foundation for the surface-wave tomography performed in Dahlke et al. (2014).

Using the same methodology outlined in Chapter 3, I create virtual source gathers in map view centered in the southwest region of the array and over Interstate 405 (Figures B.1 and B.2, respectively). Note that these are the same virtual source locations as in Figures 3.2 and 3.3, respectively. For both source locations, there is a clear wavefront visible across all times that is likely a Rayleigh wave given the frequency of investigation. The wavefront displays significant asymmetry over time, which suggests that it has a preferential propagation direction. Given that the energy is strongest in the southern region of the array at acausal time lags (when energy is moving toward the receiver) and strongest in the northern region of the array at causal time lags (when energy is moving away from the receiver), the apparent Rayleigh wave is propagating across the array from south to north. Note that this is opposite the propagation direction of the apparent body wave (Appendix A). This result agrees with the beamforming analysis in Figure 2.9, where there was significant seismic energy propagating from south to north throughout the entire array that was likely

generated from the Pacific Ocean.

When looking at a virtual source gather along a line of receivers oriented north-south and centered on E 7th St (southernmost station; Figure 3.1), the wavefront is clearly propagating from south to north (based on previous reasoning). To confirm that this wavefront is related to the Rayleigh wave, I create a dispersion image from this virtual source gather by performing a tau-p transform followed by a 1D Fourier transform along the tau axis (Figure B.4).

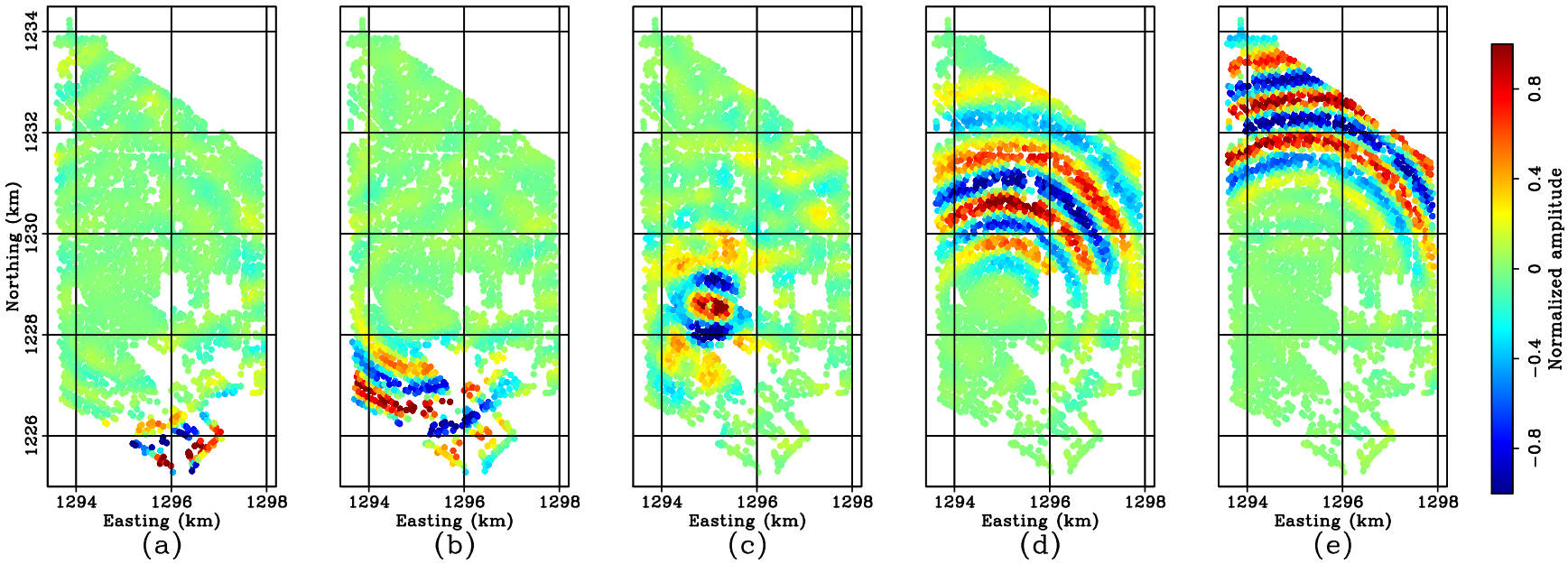

Figure B.1: Snapshots of virtual source gathers centered in the southwest region of the array (1295.0 km easting, 1228.6 km northing) at (a) -8 s, (b) -4 s, (c) 0 s, (d) 4 s, and (e) 8 s. Snapshots are bandpassed for frequencies between $0.5 - 2.0$ Hz. All panels are clipped identically. The Rayleigh wave is clearly propagating from south to north. [**CR**] appendB/. lb-01-si-micro

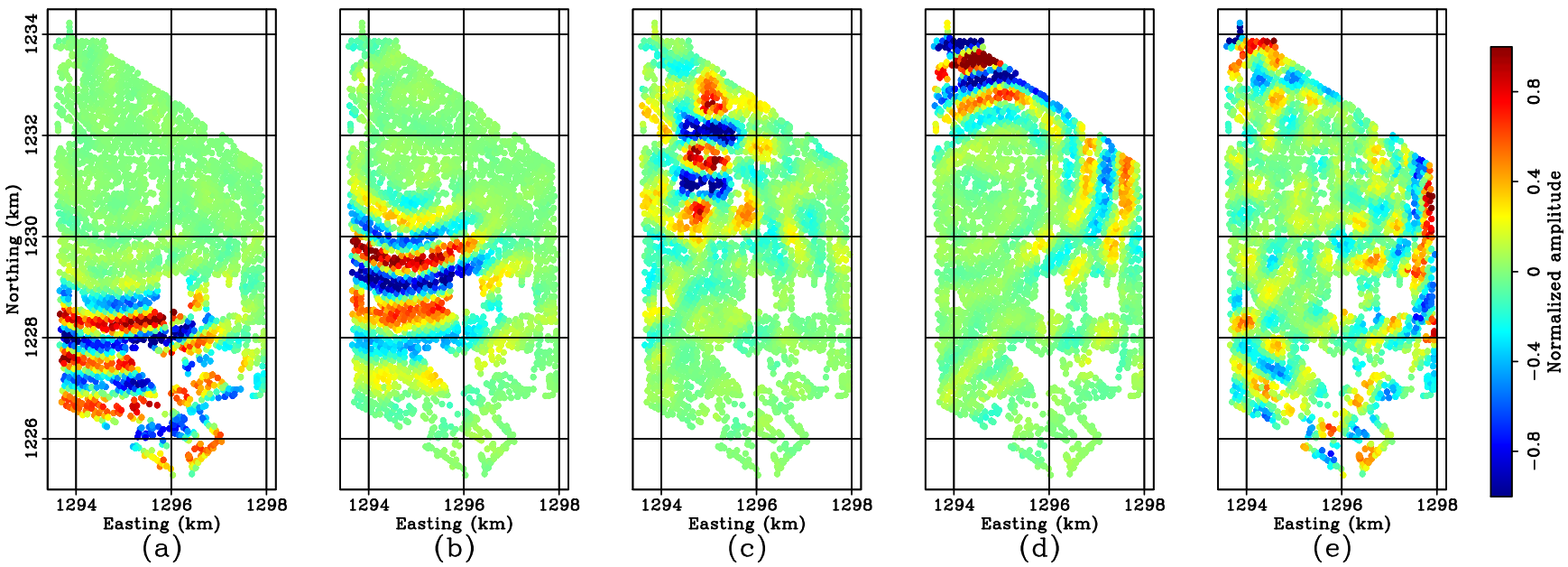

Figure B.2: Snapshots of virtual source gathers centered over Interstate 405 (1294.9 km easting, 1231.6 km northing) at (a) -8 s, (b) -4 s, (c) 0 s, (d) 4 s, and (e) 8 s. Snapshots are bandpassed for frequencies between $0.5 - 2.0$ Hz. All panels are clipped identically. The Rayleigh wave is clearly propagating from south to north. [**CR**] appendB/. lb-03-si-micro

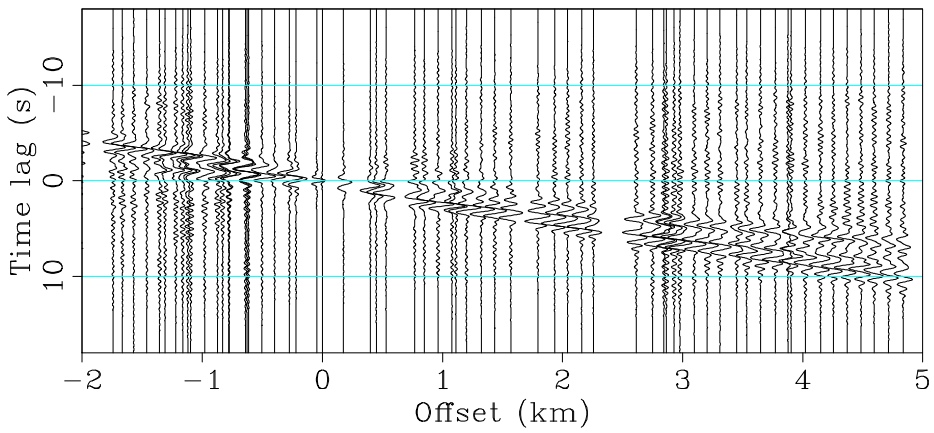

Figure B.3: Virtual source gather along a line of receivers oriented north-south. The virtual source is located on E 7th St, which is the southernmost source location in Figure 3.1. Positive offsets are toward the north, while negative offsets are toward the south. This gather is analogous to the one in Figure 3.4a. [**CR**] appendB/. nslines-micro

It appears that the wavefront is dispersive, as velocity varies with frequency. Specifically, velocity appears to decrease (slowness appears to increase) as frequency increases, which is characteristic of surface waves. As frequency increases, wavelengths become shorter and thus sense shallower depths. Combined with the observation that seismic velocity in the subsurface typically increases with depth, surface waves often exhibit the behavior observed in the dispersion image here. Additionally, propagation velocities appear to be approximately between $600 - 1000$ m/s, which are too slow to be body-wave energy. Overall, ocean-generated Rayleigh waves in the ambient seismic noise field at Long Beach can be easily recovered and interpreted at low frequencies.

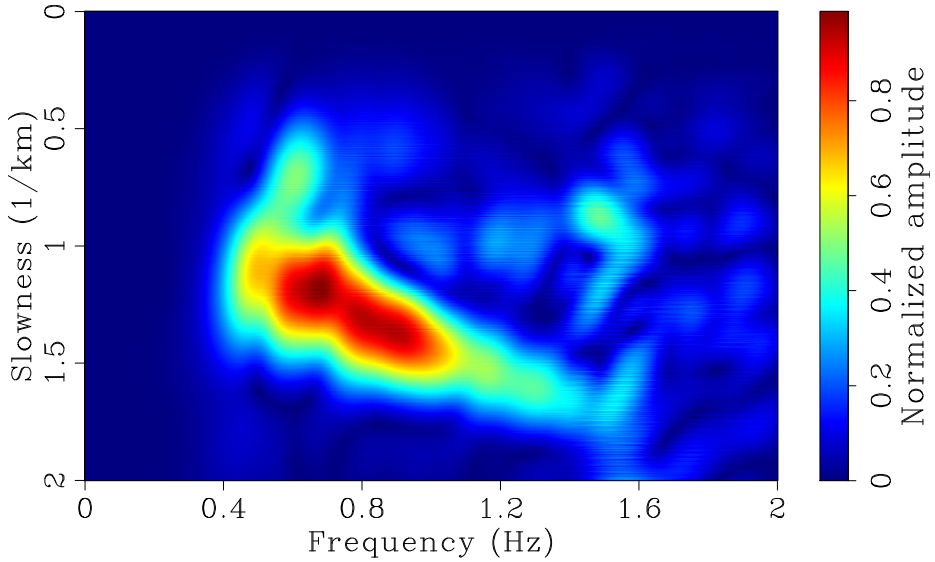

Figure B.4: Dispersion image in the frequency-slowness domain generated from the virtual source gather in Figure B.3. [**CR**] appendB/. lb-disp-micro

Bibliography

Alves, G., 2017, Elastic Full Waveform Inversion of the Moere Vest data: SEP-Report, **168**, 63–76.

Aster, R. C., B. Borchers, and C. H. Thurber, 2013, Parameter estimation and inverse problems: Academic Press.

Behm, M., G. M. Leahy, and R. Snieder, 2014, Retrieval of local surface wave velocities from traffic noise–an example from the La Barge basin (Wyoming): Geophysical Prospecting, **62**, 223–243.

Bensen, G., M. Ritzwoller, M. Barmin, A. Levshin, F. Lin, M. Moschetti, N. Shapiro, and Y. Yang, 2007, Processing seismic ambient noise data to obtain reliable broad-band surface wave dispersion measurements: Geophysical Journal International, **169**, 1239–1260.

Bensen, G., M. Ritzwoller, and N. Shapiro, 2008, Broadband ambient noise surface wave tomography across the United States: Journal of Geophysical Research: Solid Earth, **113**.

Biondi, E. and S. A. Levin, 2014, Up-down separation of ocean bottom node data using calibration filter based on critically refracted waves and adaptive subtraction: SEP-Report, **155**.

Blaik, M. and W. L. Donn, 1953, Microseism ground motion at palisades and weston: Technical report, Lamont Geological Observatory PalisadesNY.

Boiero, D., E. Wiarda, and P. Vermeer, 2013, Surface-and guided-wave inversion for near-surface modeling in land and shallow marine seismic data: The Leading Edge.

Bowden, D., V. Tsai, and F. Lin, 2015, Site amplification, attenuation, and scattering from noise correlation amplitudes across a dense array in Long Beach, CA: Geophysical Research Letters, **42**, 1360–1367.

Brooks, L. A. and P. Gerstoft, 2009, Green's function approximation from cross-correlations of 20–100 Hz noise during a tropical storm: The Journal of the Acoustical Society of America, **125**, 723–734.

Burg, K., M. Ewing, F. Press, and E. Stulken, 1951, A seismic wave guide phenomenon: Geophysics, **16**, 594–612.

California Department of Conservation, 2012, Geologic compilation of Quaternary surficial deposits in Southern California: Technical report, California Department of Conservation.

Campillo, M. and A. Paul, 2003, Long-range correlations in the diffuse seismic coda: Science, **299**, 547–549.

Chang, J. P., S. A. de Ridder, and B. L. Biondi, 2016, High-frequency Rayleigh-wave tomography using traffic noise from Long Beach, California: Geophysics, **81**, B43–B53.

Claerbout, J. F., 1968, Synthesis of a layered medium from its acoustic transmission response: Geophysics, **33**, 264–269.

Dahlke, T., G. Beroza, J. Chang, and S. de Ridder, 2014, Stochastic variability of velocity estimates using eikonal tomography on the Long Beach data set: 84th Annual International Meeting, SEG, Expanded Abstracts, 2352–2356.

de Ridder, S., B. Biondi, and R. Clapp, 2014, Time-lapse seismic noise correlation tomography at Valhall: Geophysical Research Letters, **41**, 6116–6122.

de Ridder, S., B. Biondi, and D. Nichols, 2015, Elliptical-anisotropic eikonal phase velocity tomography: Geophysical Research Letters, **42**, 758–764.

de Ridder, S. and J. Dellinger, 2011, Ambient seismic noise eikonal tomography for near-surface imaging at Valhall: The Leading Edge, **30**, 506–512.

de Ridder, S. A. and B. L. Biondi, 2015, Ambient seismic noise tomography at ekofisk: Geophysics.

Dellinger, J., A. Ross, D. Meaux, A. Brenders, G. Gesoff, J. Etgen, J. Naranjo, G. Openshaw, M. Harper, et al., 2016, Wolfspar, an" FWI-friendly" ultralow-frequency marine seismic source: Presented at the 2016 SEG International Exposition and Annual Meeting.

Draganov, D., X. Campman, J. Thorbecke, A. Verdel, and K. Wapenaar, 2013, Seismic exploration-scale velocities and structure from ambient seismic noise (¿ 1 Hz): Journal of Geophysical Research: Solid Earth, **118**, 4345–4360.

Draganov, D., K. Wapenaar, W. Mulder, J. Singer, and A. Verdel, 2007, Retrieval

of reflections from seismic background-noise measurements: Geophysical Research Letters, **34**, L04305.

Ekström, G., 2001, Time domain analysis of earth's long-period background seismic radiation: Journal of Geophysical Research: Solid Earth, **106**, 26483–26493.

Fabien-Ouellet, G., E. Gloaguen, and B. Giroux, 2017, Time-domain seismic modeling in viscoelastic media for full waveform inversion on heterogeneous computing platforms with OpenCL: Computers & Geosciences, **100**, 142–155.

Forsyth, D. W., S. C. Webb, L. M. Dorman, and Y. Shen, 1998, Phase velocities of Rayleigh waves in the MELT experiment on the East Pacific Rise: Science, **280**, 1235–1238.

Friedrich, A., F. Krueger, and K. Klinge, 1998, Ocean-generated microseismic noise located with the Gräfenberg array: Journal of Seismology, **2**, 47–64.

Garnier, J. and G. Papanicolaou, 2009, Passive sensor imaging using cross correlations of noisy signals in a scattering medium: SIAM Journal on Imaging Sciences, **2**, 396–437.

Gerstoft, P., W. S. Hodgkiss, M. Siderius, C.-F. Huang, and C. H. Harrison, 2008a, Passive fathometer processing: The Journal of the Acoustical Society of America, **123**, 1297.

Gerstoft, P., P. M. Shearer, N. Harmon, and J. Zhang, 2008b, Global P, PP, and PKP wave microseisms observed from distant storms: Geophysical Research Letters, **35**.

———, 2008c, Global P, PP, and PKP wave microseisms observed from distant storms: Geophysical Research Letters, **35**.

Gualtieri, L., 2014, Modeling the secondary microseismic noise generation and propagation.

Halliday, D., A. Curtis, and E. Kragh, 2008, Seismic surface waves in a suburban environment: Active and passive interferometric methods: The Leading Edge, **27**, 210–218.

Hasselmann, K., 1963, A statistical analysis of the generation of microseisms: Reviews of Geophysics, **1**, 177–210.

Hatchell, P. and K. Mehta, 2010, Ocean bottom seismic (obs) timing drift correction using passive seismic data, *in* SEG Technical Program Expanded Abstracts 2010, 2054–2058, Society of Exploration Geophysicists.

Hildebrand, J. A., 2009, Anthropogenic and natural sources of ambient noise in the ocean: Marine Ecology Progress Series, **395**, 5–20.

Karagianni, E., C. Papazachos, D. Panagiotopoulos, P. Suhadolc, A. Vuan, and G. Panza, 2005, Shear velocity structure in the Aegean area obtained by inversion of Rayleigh waves: Geophysical Journal International, **160**, 127–143.

Klein, G., T. Bohlen, F. Theilen, S. Kugler, and T. Forbriger, 2005, Acquisition and inversion of dispersive seismic waves in shallow marine environments: Marine Geophysical Researches, **26**, 287–315.

Kostov, C. and B. Biondi, 1987, Improving resolution of slant stacks using beam stacks: 57th Annual International Meeting, SEG, Expanded Abstracts, 792–794.

Landès, M., F. Hubans, N. M. Shapiro, A. Paul, and M. Campillo, 2010, Origin of deep ocean microseisms by using teleseismic body waves: Journal of Geophysical Research: Solid Earth, **115**.

Levin, S. A. and J. P. Chang, 2015, Stable reorientation for the forties dataset: SEP-Report, **160**, 189–194.

Levshin, A., V. Pisarenk, and G. Pogrebin, 1972, Frequency-time analysis of oscillations: Annales de Geophysique, **28**, 211–218.

Lin, F.-C., D. Li, R. W. Clayton, and D. Hollis, 2013, High-resolution 3D shallow crustal structure in Long Beach, California: Application of ambient noise tomography on a dense seismic array: Geophysics, **78**, Q45–Q56.

Lin, F.-C., M. P. Moschetti, and M. H. Ritzwoller, 2008, Surface wave tomography of the western United States from ambient seismic noise: Rayleigh and Love wave phase velocity maps: Geophysical Journal International, **173**, 281–298.

Lin, F.-C., M. H. Ritzwoller, and R. Snieder, 2009, Eikonal tomography: surface wave tomography by phase front tracking across a regional broad-band seismic array: Geophysical Journal International, **177**, 1091–1110.

Lin, F.-C., M. H. Ritzwoller, J. Townend, S. Bannister, and M. K. Savage, 2007, Ambient noise Rayleigh wave tomography of New Zealand: Geophysical Journal International, **170**, 649–666.

Lobkis, O. I. and R. L. Weaver, 2001, On the emergence of the Green's function in the correlations of a diffuse field: The Journal of the Acoustical Society of America, **110**, 3011–3017.

Longuet-Higgins, M. S., 1950, A theory of the origin of microseisms: Philosophical Transactions of the Royal Society of London A: Mathematical, Physical and Engineering Sciences, **243**, 1–35.

Martin, E. R., F. Huot, Y. Ma, R. Cieplicki, S. Cole, M. Karrenbach, and B. L.

Biondi, 2018, A Seismic Shift in Scalable Acquisition Demands New Processing: Fiber-Optic Seismic Signal Retrieval in Urban Areas with Unsupervised Learning for Coherent Noise Removal: IEEE Signal Processing Magazine, **35**, 31–40.

McNamara, D. and R. Boaz, 2005, Seismic noise analysis system, power spectral density probability density function: stand-alone software package: Technical report, USGS Open-File Report 2005-1438.

Mikesell, D., K. van Wijk, A. Calvert, and M. Haney, 2009, The virtual refraction: Useful spurious energy in seismic interferometry: Geophysics, **74**, A13–A17.

Mooney, W. D. and A. Ginzburg, 1986, Seismic measurements of the internal properties of fault zones: Pure and Applied Geophysics, **124**, 141–157.

Mordret, A., M. Landès, N. Shapiro, S. Singh, P. Roux, and O. Barkved, 2013, Near-surface study at the valhall oil field from ambient noise surface wave tomography: Geophysical Journal International, ggt061.

Mordret, A., N. M. Shapiro, and S. Singh, 2014, Seismic noise-based time-lapse monitoring of the Valhall overburden: Geophysical Research Letters, **41**, 4945–4952.

Moronfoyer, A. T., S. Ronen, S. L. Klemperer, and G. Alves, 2016, Upper-crustal structure of the Møre margin, offshore-norway: 20016 AGU Fall Meeting, San Francisco, –.

Moschetti, M., M. Ritzwoller, and N. Shapiro, 2007, Surface wave tomography of the western United States from ambient seismic noise: Rayleigh wave group velocity maps: Geochemistry, Geophysics, Geosystems, **8**.

Nakata, N., J. P. Chang, J. F. Lawrence, and P. Boué, 2015, Body wave extraction and tomography at Long Beach, California, with ambient-noise interferometry: Journal of Geophysical Research: Solid Earth, **120**, 1159–1173.

Nakata, N., R. Snieder, T. Tsuji, K. Larner, and T. Matsuoka, 2011, Shear wave imaging from traffic noise using seismic interferometry by cross-coherence: Geophysics, **76**, SA97–SA106.

Picozzi, M., S. Parolai, D. Bindi, and A. Strollo, 2009, Characterization of shallow geology by high-frequency seismic noise tomography: Geophysical Journal International, **176**, 164–174.

Pilz, M., S. Parolai, M. Picozzi, and D. Bindi, 2012, Three-dimensional shear wave velocity imaging by ambient seismic noise tomography: Geophysical Journal International, **189**, 501–512.

Poli, P., M. Campillo, H. Pedersen, et al., 2012, Body-wave imaging of Earths mantle

discontinuities from ambient seismic noise: Science, **338**, 1063–1065.

Rickett, J. and J. Claerbout, 1999, Acoustic daylight imaging via spectral factorization: Helioseismology and reservoir monitoring: The leading edge, **18**, 957–960.

Rost, S. and C. Thomas, 2002, Array seismology: methods and applications: Reviews of Geophysics, **40**, 2–1.

Roux, P., K. G. Sabra, P. Gerstoft, W. Kuperman, and M. C. Fehler, 2005, P-waves from cross-correlation of seismic noise: Geophysical Research Letters, **32**.

Ruigrok, E., X. Campman, and K. Wapenaar, 2011, Extraction of P-wave reflections from microseisms: Comptes Rendus Geoscience, **343**, 512–525.

Sabra, K. G., P. Gerstoft, P. Roux, W. Kuperman, and M. C. Fehler, 2005a, Extracting time-domain Green's function estimates from ambient seismic noise: Geophysical Research Letters, **32**.

———, 2005b, Surface wave tomography from microseisms in Southern California: Geophysical Research Letters, **32**.

Schalkwijk, K., C. Wapenaar, and D. Verschuur, 1999, Application of two-step decomposition to multicomponent ocean-bottom data: Theory and case study: Journal of Seismic Exploration, **8**, 261–278.

Schimmel, M. and H. Paulssen, 1997, Noise reduction and detection of weak, coherent signals through phase-weighted stacks: Geophysical Journal International, **130**, 497–505.

Schimmel, M., E. Stutzmann, and J. Gallart, 2011, Using instantaneous phase coherence for signal extraction from ambient noise data at a local to a global scale: Geophysical Journal International, **184**, 494–506.

Seats, K. J., J. F. Lawrence, and G. A. Prieto, 2012, Improved ambient noise correlation functions using Welch's method: Geophysical Journal International, **188**, 513–523.

Shapiro, N. M., M. Campillo, L. Stehly, and M. H. Ritzwoller, 2005, High-resolution surface-wave tomography from ambient seismic noise: Science, **307**, 1615–1618.

Shtivelman, V., 2004, Estimating seismic velocities below the sea-bed using surface waves: Near Surface Geophysics, **2**, 241–247.

Siderius, M., H. Song, P. Gerstoft, W. S. Hodgkiss, P. Hursky, and C. Harrison, 2010, Adaptive passive fathometer processing: The Journal of the Acoustical Society of America, **127**, 2193.

Snieder, R., 2004, Extracting the Green's function from the correlation of coda waves:

A derivation based on stationary phase: Physical Review E, **69**, 046610.

Snieder, R., Y. Fan, E. Slob, and K. Wapenaar, 2010, Equipartitioning is not sufficient for Green's function extraction: Earthquake Science, **23**, 403–415.

Socco, L. V., S. Foti, and D. Boiero, 2010, Surface-wave analysis for building near-surface velocity models–Established approaches and new perspectives: Geophysics, **75**, 75A83–75A102.

Stehly, L., M. Campillo, and N. Shapiro, 2006, A study of the seismic noise from its long-range correlation properties: Journal of Geophysical Research: Solid Earth, **111**.

Toksöz, M. N. and R. T. Lacoss, 1968, Microseisms: Mode structure and sources: Science, **159**, 872–873.

Wang, J., R. R. Stewart, N. I. Dyaur, and M. L. Bell, 2016, Marine guided waves: Subbottom property estimation and filtering using physical modeling data: Geophysics.

Wapenaar, K., 2004, Retrieving the elastodynamic Green's function of an arbitrary inhomogeneous medium by cross correlation: Physical Review Letters, **93**, 254301.

Wapenaar, K., D. Draganov, R. Snieder, X. Campman, and A. Verdel, 2010, Tutorial on seismic interferometry: Part 1–basic principles and applications: Geophysics, **75**, 75A195–75A209.

Wapenaar, K. and J. Fokkema, 2006, Greens function representations for seismic interferometry: Geophysics, **71**, SI33–SI46.

Weemstra, C., W. Westra, R. Snieder, and L. Boschi, 2014, On estimating attenuation from the amplitude of the spectrally whitened ambient seismic field: Geophysical Journal International, ggu088.

Welch, P., 1967, The use of fast Fourier transform for the estimation of power spectra: a method based on time averaging over short, modified periodograms: IEEE Transactions on audio and electroacoustics, **15**, 70–73.

Wenz, G. M., 1972, Review of underwater acoustics research: Noise: The Journal of the Acoustical Society of America, **51**, 1010–1024.

Widmer-Schnidrig, R. and G. Laske, 2007, Theory and observations-normal modes and surface wave measurements: Treatise on Geophysics, **1**, 67–125.

Wills, C. J. and W. Silva, 1998, Shear-wave velocity characteristics of geologic units in California: Earthquake Spectra, **14**, 533–556.

Witek, M., S. van der Lee, and T.-S. Kang, 2014, Rayleigh wave group velocity distributions for East Asia using ambient seismic noise: Geophysical Research Letters, **41**, 8045–8052.

Wu, F. T., A. L. Levshin, and V. M. Kozhevnikov, 1997, Rayleigh wave group velocity tomography of Siberia, China and the vicinity: Pure and Applied Geophysics, **149**, 447–473.

Yang, Y., M. H. Ritzwoller, F.-C. Lin, M. Moschetti, and N. M. Shapiro, 2008, Structure of the crust and uppermost mantle beneath the western United States revealed by ambient noise and earthquake tomography: Journal of Geophysical Research: Solid Earth, **113**.

Zhan, Z., S. Ni, D. V. Helmberger, and R. W. Clayton, 2010, Retrieval of Moho-reflected shear wave arrivals from ambient seismic noise: Geophysical Journal International, **182**, 408–420.

Zhang, J., P. Gerstoft, and P. D. Bromirski, 2010, Pelagic and coastal sources of P-wave microseisms: Generation under tropical cyclones: Geophysical Research Letters, **37**.